

Copyright Undertaking

This thesis is protected by copyright, with all rights reserved.

By reading and using the thesis, the reader understands and agrees to the following terms:

- 1. The reader will abide by the rules and legal ordinances governing copyright regarding the use of the thesis.
- 2. The reader will use the thesis for the purpose of research or private study only and not for distribution or further reproduction or any other purpose.
- 3. The reader agrees to indemnify and hold the University harmless from and against any loss, damage, cost, liability or expenses arising from copyright infringement or unauthorized usage.

IMPORTANT

If you have reasons to believe that any materials in this thesis are deemed not suitable to be distributed in this form, or a copyright owner having difficulty with the material being included in our database, please contact lbsys@polyu.edu.hk providing details. The Library will look into your claim and consider taking remedial action upon receipt of the written requests.

SUBSTRATE AND INTERFACE ENGINEERING FOR CENTIMETERSIZED WAFER-SCALE GROWTH OF CRYSTALLINE BLACK PHOSPHORUS ULTRATHIN FILMS

ZHAO YUQIAN

PhD

The Hong Kong Polytechnic University

2025

The Hong Kong Polytechnic University Department of Applied Physics

Substrate and Interface Engineering for
Centimeter-sized Wafer-scale Growth of
Crystalline Black Phosphorus Ultrathin
Films

ZHAO Yuqian

An initial thesis submitted in partial fulfilment of the requirements for the degree of Doctor of Philosophy

January 2025

CERTIFICATE OF ORIGINALITY

| hereby declare that this thesis is my own work and that, to the best of my knowledge |
|------------------------------------------------------------------------------------------|
| and belief, it reproduces no material previously published or written, nor material that |
| has been accepted for the award of any other degree or diploma, except where due |
| acknowledgement has been made in the text. |
| |
| |
| |
| |
| |
| |
| |
| (Signed) |
| ZHAO Yuqian (Name of student) |



Abstract

Since Novoselov et al. first successfully exfoliated graphene from bulk graphite using scotch tape in 2004, two-dimensional (2D) materials have emerged as a significant area of research, recognized for their vast potential applications across various fields, including flexible devices, sensors, and optics. Among these materials, 2D black phosphorus (BP) and its monolayer form, phosphorene, have attracted considerable attention as promising alternatives to graphene. 2D BP not only possesses a bandgap that lies between that of graphene (0 eV) and transition metal dichalcogenides (TMDs) (1.0 eV–2.0 eV), but also exhibits a tunable direct bandgap, exceptional carrier mobility, and a significant on/off ratio. These characteristics position BP as one of the most compelling research topics within the realm of 2D materials. For the successful commercialization of BP, it is essential to establish robust techniques for producing large-area 2D BP-based devices on various available substrates under easily controlled conditions for further investigation.

In the first part of the thesis, we employed a piezoelectric actuator to conduct the interfacial biaxial strain engineering, allowing us to investigate the anisotropic Raman response of the ultrathin BP transferred onto an oxide dielectric substrate. Our findings revealed that three characteristic peaks exhibit a redshift when tensile strain is applied, while they display a blueshift under compressive strain. Notably, under a tensile strain of 0.2%, the B_{2g} mode experiences a shift of -12.2 cm⁻¹/%. Conversely, when a compressive strain of -0.2% is applied, the Raman shift rate of the B_{2g} mode can increase to as much as 15.3 cm⁻¹/%. Additionally, we calculated the Grüneisen parameters to explore the relationship between tensile or compressive strain and the

phonon behavior of crystalline BP. The underlying physical mechanism responsible for the observed Raman response under strain is discussed, highlighting its connection to variations in bond angles and bond lengths within BP. Furthermore, modulation of biaxial strain may alter the anisotropic dispersion of BP, underscoring its substantial potential for innovative polarized light detection applications.

Although exfoliation enables efficient separation of high-quality multilayer 2D BP from single-crystalline bulk sources, facilitating detailed investigations into their fundamental properties. However, this method is not ideal for large-scale production due to challenges in achieving precise control over both the thickness and lateral dimensions. Consequently, in the second part of the thesis, we developed a clean transfer strategy to produce centimeter-scale, high-quality few-layer BP films grown via precisely controlled pulsed laser deposition (PLD) on silicon substrates. Ethylene-vinyl acetate (EVA) polymer and ethylene glycol (EG) were selected as the adhesive layer and medium, respectively, to preserve the superior crystalline quality and properties of BP throughout the transfer process. Importantly, we successfully fabricated large-scale bottom-gate few-layer BP field-effect transistor (FET) arrays on SiO₂/Si substrates, demonstrating exceptional homogeneity. Our FET device arrays demonstrated exceptional electrical characteristics, featuring a high carrier mobility of 295 cm² V⁻¹ s⁻¹ and a significant current switching ratio of 3.6×10³, comparable to that of as-grown BP films on mica substrates. This work illustrates that the wet transfer method can effectively create scalable, high-crystallinity BPbased device arrays while maintaining excellent electrical performance, thus enabling more complex design possibilities for a wide range of applications.



List of Publications

- Yuqian, Zhao, Zehan Wu, Zhaoying Dang, and Jianhua Hao*. "Progress in the synthesis of 2D black phosphorus beyond exfoliation." *Applied Physics Reviews* 9 (2022): 041318.
- Yuqian Zhao, Feng Guo, Sin-Yi Pang, Weng Fu Io, Lok Wing Wong, Jiong Zhao, and Jianhua Hao*. "Piezoelectric substrate-induced strain engineering on tuning polarized Raman spectra of crystalline black phosphorus" *Applied Physics Letters* 122 (2023): 132903.
- 3. **Yuqian Zhao**, Jianfeng Mao, Zehan Wu, Weng Fu Io, Sing-Yi Pang, Yifei Zhao and Jianhua Hao*. "A clean transfer approach to prepare centimetre-scale black phosphorus crystalline multilayers on silicon substrates for field-effect transistors." *Nature Communications* **15** (2024): 6795.
- 4. Ran Ding, Yongxin Lyu, Yuqian Zhao, Zehan Wu, Feng Guo, Weng Fu Io, Sin-Yi Pang, Jianfeng Mao, Man-Chung Wong, Lok Wing Wong, Cenqi Yan, Jiangsheng Yu, Jiong Zhao, Gang Li and Jianhua Hao* "Revealing photovoltaic behavior in 2D hybrid perovskite ferroelectric single-crystalline microwire arrays for self-powered photodetectors." *Materials Today Physics* 28 (2022): 100867.
- Weng Fu Io, Man-Chung Wong, Sin-Yi Pang, Yuqian Zhao, Ran Ding, Feng Guo, and Jianhua Hao*. "Strong piezoelectric response in layered CuInP2S6 nanosheets for piezoelectric nanogenerators." Nano Energy 99 (2022): 107371.
- Weng Fu Io, Sin-Yi Pang, Lok Wing Wong, Yuqian Zhao, Ran Ding, Jianfeng
 Mao, Yifei Zhao, Feng Guo, Shuoguo Yuan, Jiong Zhao, Jiabao Yi, Jianhua



- Hao*. "Direct observation of intrinsic room-temperature ferroelectricity in 2D layered CuCrP₂S₆." *Nat Commun* **14** (2023): 7304.
- Sin-Yi Pang, Weng Fu Io, Feng Guo, Yuqian Zhao, Jianhua Hao*, "Two-dimensional MXene-based devices for information technology", *Mater Sci Eng R: Rep.* 163 (2025): 100894.
- Resen Yang*, Chuan-Pu Liu*, Till Frömling*, Jianhua Hao*, Jaya Venkat Spandana Rao, Yuqian Zhao, "Piezotronic and Piezo-phototronic sensors", MRS Bull. 50 (2025): 123.

Acknowledgement

First and foremost, I would like to express my heartfelt appreciation and respect for my supervisor, Prof. Jianhua Hao, for his invaluable guidance, patient mentorship, and unwavering support throughout my postgraduate studies. His extensive scientific expertise and enthusiasm for science and research have profoundly impacted my determination to complete my PhD degree.

I would also like to extend my sincere gratitude to the professors who provided invaluable support during my experimental studies and coursework. Additionally, I am grateful for the assistance of the technicians who facilitated the use of equipment in the UMF and our department.

I would like to convey my sincere gratitude to my research colleagues for their invaluable help and support during my investigations.

I gratefully thank the financial support from the Hong Kong Research Grant Council (RGC) of Hong Kong (RGC GRF No. PolyU 15301121).

I would like to thank my parents for their endless love. You are the best parents in the world!

I would like to thank my friends for their endless tolerance and support; your presence in my life makes everything worthwhile.

Finally, I want to thank myself. You did it—great job!



Table of Contents

| Abstract | I |
|--------------------------------------------------------------|------|
| List of Publications | III |
| Acknowledgement | V |
| Table of Contents | VI |
| Table of Figures | IX |
| List of Tables | XIII |
| Chapter 1 Introduction | 1 |
| 1.1 Background of two-dimensional materials | 1 |
| 1.2 Brief introduction of black phosphorus | 2 |
| 1.3 Material structure and fundamental characteristics of BP | 4 |
| 1.4 Synthesis of 2D BP | 7 |
| 1.5 Transfer techniques for 2D materials | 10 |
| 1.6 Objective of the research | 14 |
| 1.7 Organization of thesis | 16 |
| Chapter 2 Methodology | 18 |
| 2.1 Preparation methods of 2D BP | 18 |
| 2.1.1 Mechanical exfoliation | 19 |
| 2.1.2 Pulsed laser deposition approach | 21 |
| 2.2 Characterization process for 2D BP | 23 |
| 2.2.1 Optical microscope | 23 |

| | 2.2.2 X-ray diffraction | 24 |
|-----|--------------------------------------------------------------------------|----|
| | 2.2.3 Atomic force spectroscopy | 25 |
| | 2.2.4 Transmission electron microscopy | 27 |
| | 2.2.5 Raman spectroscopy | 29 |
| 2. | 3 Device fabrication process | 30 |
| | 2.3.1 Photolithography | 30 |
| | 2.3.2 Electron beam evaporation | 32 |
| | 2.3.3 Dry transfer | 34 |
| | 2.3.4 Wet transfer | 34 |
| 2. | 4 Device characterizations | 35 |
| Cha | pter 3 Exploring the anisotropic properties of BP with PMN-PT substrates | 37 |
| 3. | 1 Introduction | 37 |
| 3. | 2 Interfacial strain engineering of BP by PMN-PT substrates | 39 |
| 3. | 3 Material characterization of BP nanoflakes | 41 |
| 3. | 4 Anisotropic characteristic of BP via polarized Raman spectroscopy | 43 |
| 3. | 5 Raman spectroscopy of BP under biaxial strain | 47 |
| 3. | 6 Conclusion | 54 |
| Cha | pter 4 Prepare centimetre-scale BP-based devices on silicon substrates | 56 |
| 4. | 1 Introduction | 56 |
| 4. | 2 Growth conditions for BP via PLD | 58 |
| 4. | 3 Fabrication process for FETs | 58 |



| | 4.4 Characterization of BP and FET arrays | . 59 |
|---|------------------------------------------------|------|
| | 4.5 Clean transfer process of BP | . 60 |
| | 4.6 Adhesion analysis of different interfaces | . 61 |
| | 4.7 Material characterization of BP thin films | . 68 |
| | 4.8 Electrical properties of BP-based FETs | . 73 |
| | 4.9 Conclusion | . 85 |
| C | hapter 5 Conclusion and future prospectives | . 87 |
| | 5.1 Conclusion | . 87 |
| | 5.2 Future Perspectives | . 88 |
| R | eferences | . 92 |



Table of Figures

| Figure 1.1 Schematic representation of (a) the tetrahedral WP P4 molecule, | |
|-------------------------------------------------------------------------------------|------|
| (b)molecular structure of monolayer phosphorene, and (c) the properties and | |
| corresponding applications of low-dimensional BP. 83-90 | 7 |
| Figure 2.1 Schematic illustration of mechanical exfoliation process. 131 | . 20 |
| Figure 2.2 Schematic diagram of the main components within a PLD system 132 | . 22 |
| Figure 2.3 Photo of the PLD chamber utilized for BP thin film deposition | . 23 |
| Figure 2.4 Schematic illustration of the working principle of XRD ¹³³ | . 25 |
| Figure 2.5 Schematic illustration of the working principle of AFM ¹³⁴ | . 27 |
| Figure 2.6 Schematic illustration of TEM ¹³⁵ | . 28 |
| Figure 2.7 Schematic illustration of Raman spectroscopy ¹³⁶ | . 30 |
| Figure 2.8 Overview of photolithography ¹³⁷ | . 32 |
| Figure 2.9 Photo of the Denton Explorer E-beam deposition system | . 33 |
| Figure 2.10 Photograph of the device electric measurement system | . 36 |
| Figure 3.1 Schematic illustration of device fabrication for BP on a piezoelectric | |
| PMN-PT substrate | . 39 |
| Figure 3.2 Schematic illustration of the device structure for BP on a piezoelectric | |
| PMN-PT substrate | . 40 |
| Figure 3.3 AFM height profiles of the mechanical-exfoliated BP nanoflakes. Inset: | |
| corresponding AFM image | . 41 |
| Figure 3.4 HRTEM image of the mechanical-exfoliated BP nanoflakes | . 42 |
| Figure 3.5 SEAD pattern of the mechanical-exfoliated BP nanoflakes | . 42 |
| Figure 3.6 Raman spectrum of the mechanical-exfoliated BP nanoflakes. | . 43 |

| Figure 3. / Schematic illustration of Raman spectra acquisition using an |
|-------------------------------------------------------------------------------------------------|
| electromechanical device that applies external biaxial strain |
| Figure 3.8 Polarized Raman spectra of BP nanosheets obtained at different |
| polarization angles |
| Figure 3.9 Polar plots illustrating the intensity variations of the A_g^2 Raman peak 46 |
| Figure 3.10 Polar plots illustrating the intensity variations of the B_{2g} Raman peak 47 |
| Figure 3.11 Raman spectra of the BP sample on a PMN-PT substrate subjected to |
| various biaxial strains49 |
| Figure 3.12 The 3D representation of BP structures includes specific definitions for |
| various structural parameters |
| Figure 3.13 Polarized Raman spectra of the BP nanoflake under conditions of no |
| strain, 0.2% tensile strain, and -0.2% compressive strain. Inset: A magnified view of |
| the region surrounding the Ag ¹ peak |
| Figure 3.14 Polar plot illustrates the polarized Raman peak intensities for the B_{2g} |
| mode under various biaxial strain conditions |
| Figure 3.15 Polar plot illustrates the polarized Raman peak intensities for the ${\rm A_g}^2$ |
| mode under various biaxial strain conditions |
| Figure 4.1 Schematic diagram of wet transfer process of PLD-deposited BP thin film |
| with EVA polymer assisted in EG solution |
| Figure 4.2 Left: Optical photo and Right: Microscopic images of wet-transferred BP |
| on SiO ₂ /Si substrate (scale bar:10 μm) |
| Figure 4.3 Microscopic image of wet-transferred BP sample on the SiO ₂ /Si substrate |
| using PS polymer in EG solvent |
| Figure 4.4 Contact angle measurements of EG and glycerol (Gly) on different |
| surfaces. 63 |

| Figure 4.5 Work of adhesion at various interfaces. 64 |
|--------------------------------------------------------------------------------------------------|
| Figure 4.6 Molecular formula of (a) EVA and (b) PS |
| Figure 4.7 Schematic representation of the delamination process in EG and IPA |
| solutions during peeling. 66 |
| Figure 4.8 AFM topography and height analysis of the EVA polymer is presented in |
| (a) before and (b) after immersion in EG solvent. A comparable analysis of the EVA |
| polymer is shown in (c) before and (d) after immersion in IPA solvent |
| Figure 4.9 Optical image of BP sample on mica substrates (a) after direct growth, (b) |
| after wet transfer with EVA polymer in EG solvent |
| Figure 4.10 The AFM height profile of direct-grown BP thin films on a mica |
| substrate. 68 |
| Figure 4.11 The AFM height profile of wet-transferred BP thin films onto a SiO ₂ /Si |
| substrate. 69 |
| Figure 4.12 XRD patterns for the bare mica substrate, as-grown BP, and wet- |
| transferred BP |
| Figure 4.13 Raman spectra of BP thin films before the wet transfer process (on mica |
| substrate) and after the transfer to SiO ₂ /Si substrate |
| Figure 4.14 An optical microscope image of wet-transferred BP FET arrays with |
| varying channel lengths on a SiO ₂ /Si substrate |
| Figure 4.15 Drain current (I_{ds}) versus drain voltage (V_{ds}) curves for BP FETs with |
| channel lengths of 75 μm (red), 270 μm (orange), 420 μm (blue), and 570 μm |
| (green) |
| Figure 4.16 I_{ds} - V_{ds} curves under different passivation conditions, presented in both |
| linear and logarithmic scales in the inset |
| Figure 4.17 LV., curves before and after the removal of the EVA polymer 77 |

| Figure 4.18 Schematic illustration of the wet-transferred back-gate BP FET 79 |
|----------------------------------------------------------------------------------------------------------|
| Figure 4.19 I_{ds} - V_{ds} for the BP FET at various V_g , including 0 V, -1 V, -2 V, -3 V, -4 V, |
| -5 V, -10 V, -20 V, and -30 V. The inset provides a zoom-in view of the I_{ds} -V $_{ds}$ curves |
| for a 5-nm BP FET at gate voltages of -2 V, -1 V, 0 V, 1 V, and 2 V |
| Figure 4.20 The transfer characteristics of a BP FET with a 75 μm-channel length on |
| a linear scale with a drain voltage of -0.1 V; the red dashed line indicates the linear fit |
| of I _{ds} . The inset displays the transfer characteristics for BP FETs with channel lengths |
| of 75 μm, 270 μm, 420 μm, and 570 μm on a logarithmic scale with a drain voltage |
| of -0.1 V |
| Figure 4.21 Dependence of mobility and on/off ratio on channel length |



List of Tables

| Table 1-1 Comparison of 2D BP nanoflakes and thin films produced using various |
|-------------------------------------------------------------------------------------|
| fabrication techniques |
| Table 2-1 Comparison summary: Mechanical Exfoliation vs. PLD |
| Table 3-1 Grüneisen parameter of different materials under various strain inducing |
| conditions |
| Table 4-1 Comparison of surface roughness of 2D materials before and after transfer |
| |
| Table 4-2 Comparison of thin-film FETs constructed using BP (same material) or wet |
| transfer (similar preparation methods)85 |



Chapter 1 Introduction

1.1 Background of two-dimensional materials

Two-dimensional (2D) materials are defined as a category of extremely thin, sheet-like crystals that have a thickness at the atomic or molecular level, while their lateral dimensions are usually in the micrometer range. Since the successful isolation of graphene by Novoselov and his group through the mechanical exfoliation of highly oriented pyrolytic graphite in 2004, there has been a surge of scientific interest in these materials due to their promising applications and fundamental properties. 2D materials offer several notable benefits compared to their bulk counterparts, such as enhanced electron mobility, adjustable bandgap energy, a strong optical response, superior thermal conductivity, exceptional environmental stability, and remarkable mechanical flexibility. 4-6

The unique structural characteristics of 2D materials arise from their strong intralayer covalent bonds coupled with weak interlayer van der Waals (vdW) forces. This combination allows for easy exfoliation and transfer to flexible substrates without concerns about crystal lattice mismatches.^{7,8} Additionally, the presence of interlayer vdW forces—rather than dangling bonds—results in minimal point and line defects between layers. This defect suppression is crucial as it reduces non-radiative carrier recombination, thereby enhancing photoelectric efficiency and conservation.^{9,10}

In recent years, 2D materials have garnered extensive research attention not only in the fields of electronics and optoelectronics but also in emerging applications such as flexible photonics and optics.^{11,12} Their ability to facilitate effective energy conversion

has made them particularly attractive for use in electrochemical energy storage devices, including solar cells.^{13,14} The integration of 2D materials into these technologies promises to enhance performance metrics significantly, paving the way for advancements in energy efficiency and sustainability.^{15,16}

As researchers continue to explore the enormous potential of 2D materials, their unique properties are expected to drive innovations across various applications.¹⁷ From improving the performance of electronic devices to providing some solutions for energy storage, the versatility and capabilities of 2D materials hold great promise for future technological developments.^{18,19} The ongoing investigation into their synthesis, material property characterization, and integration into practical applications will undoubtedly lead to exciting breakthroughs in both fundamental science and novel applied engineering.^{20–22}

1.2 Brief introduction of black phosphorus

Black phosphorus (BP) was first identified as an allotrope of phosphorus with semiconducting properties over a century ago.²³ Its potential remained largely unexplored until 2014, when researchers successfully exfoliated 2D BP and phosphorene (monolayer BP) with scotch tape.²⁴ This breakthrough positioned BP as a promising alternative to graphene, which, despite its high charge carrier mobility, lacks a bandgap in its electronic structure.^{25,26} This absence of bandgap largely limits applicability of graphene in various electronic and optoelectronic devices that require semiconducting characteristics.^{27,28}

In addition to BP, transition metal dichalcogenides (TMDs) have also attracted significant attention due to their substantial bandgaps and semiconducting

properties.^{29,30} While the TMD family collectively encompasses a broad spectrum of large bandgaps, the bandgap tunability of each individual TMD compound remains limited relative to that of BP, thereby constraining their applicability across a wider range of applications.^{31,32} In contrast, 2D BP features a moderate and tunable bandgap, which lies between that of graphene (0 eV)³³ and TMDs (1.0 eV-2.0 eV)^{34,35}, effectively spanning a wide range from visible to mid-infrared.^{36,37} The ability to scale down BP results in a thickness-dependent direct bandgap, along with impressive hole-dominated carrier mobility and notable on/off ratios.³⁸ Moreover, the orthorhombic lattice structure of BP lacks symmetry, which induces in-plane anisotropy.^{39,40} This unique feature allows for modulation of the optical and electrical properties based on crystal orientation. Due to these diverse and fascinating properties, BP has emerged as one of the most attractive materials within the 2D materials family.^{41,42} Its exceptional characteristics make it an ideal candidate for various applications, including biomedical devices^{43,44}, energy storage^{45,46}, optoelectronics, and photonics^{47,48}.

Significant efforts have been made in designing and fabricating high-performance BP-based devices through various manipulation strategies such as interface and defect modification⁴⁹, fabrication of stacked heterostructures⁵⁰, and bandgap engineering⁵¹. Despite the promising application potential of BP-based devices, challenges remain in scaling up and achieving controlled preparation of few-layer large-area thin films. Also, there are still several material properties of 2D BP that require more in-depth investigation. Understanding these properties is essential for optimizing the performance of BP in various applications. By conducting comprehensive research, we can better harness the unique characteristics of 2D BP for practical advanced technological applications.

1.3 Material structure and fundamental characteristics of BP

Phosphorus is known as one of the most common elements on Earth.⁵² It exists in several allotropes, including red phosphorus (RP)⁵³, white phosphorus (WP)⁵⁴, and BP. BP has garnered significant attention among all allotropes due to its unique properties and potential applications.⁵⁵ Research by Bachhuber et al. utilized quantum mechanical simulations to reveal that the vdW forces between layers are the primary attractive forces influencing the stability order of all known phosphorus allotropes.⁵⁶ These vdW interactions are crucial for holding the layers together, thereby facilitating the formation of bulk crystals. Among all the allotropes of phosphorus, orthorhombic BP is recognized as the most thermodynamically stable structure.⁵⁷

As illustrated in Figure 1.1a, the molecular structure of WP consists of P₄ molecules arranged at the corners of a tetrahedron, with each phosphorus atom singly bonded to the others. This P4 structure contains six P-P single bonds and four lone pairs of electrons. Unlike the ideal 90° angle formed by pure 3p orbitals, the bond angles between P-P-P in WP measure approximately 60.31°. ⁵⁸ Consequently, this tetrahedral arrangement is stabilized by arc-like bonds, which introduce ring strain and contribute to instability. ⁵⁹ In contrast, BP layers are formed from interconnected P₄ molecules in monolayer BP (also referred to as phosphorene). The sp³ hybridization process breaks the individual P₄ bonds and results in two distinct bond angles of 99.48° and 103.37°, as shown in Figure 1b. This alteration enhances the stability of BP as these angles approach the optimal tetrahedral angle of 109.5°.

Black phosphorus has garnered considerable interest due to its unique crystal structure, which gives rise to distinct characteristics. Unlike many other 2D semiconductors that exhibit a direct bandgap only at specific thicknesses, BP maintains a direct bandgap

feature regardless of the number of layers. 60,61 This property makes BP an excellent candidate for applications in effective photoelectric conversion and advanced lightemitting devices. The strong electronic state coupling within the layers of BP leads to notable differences in the bandgap across its bulk, single-layer, and few-layer forms. 62,63 Specifically, the bandgap of bulk BP is approximately 0.3 eV⁶⁴, while the theoretical studies suggest that the bandgap for monolayer and multilayer BP ranges from 1.51 eV to 2 eV, with variations arising from the different calculation methods employed. 65,66 Experimental investigations have also been conducted to measure the bandgap of BP, and similar to theoretical predictions, these results vary based on the techniques used. For instance, with application of surface-sensitive high-resolution scanning tunnelling spectroscopy, Liang et al. has reported a bandgap of 2.05 eV for monolayer BP, focusing on the topmost layer of the material.⁶⁷ In contrast, defectsinsensitive absorption spectroscopy indicates an optical bandgap of 1.73 eV for monolayer BP.⁶⁸ The lack of interlayer hybridization near the top of the valence band and the bottom of the conduction band is believed to contribute to the increased bandgap observed in single-layer BP. Despite fluctuations in theoretical and experimental values, a consistent trend emerges as the number of layers increases, the bandgap generally decreases due to vdW interactions between layers that promote band splitting. ⁶⁹

Another remarkable property that has attracted significant research interest is the high carrier mobility of BP compared to other materials in the TMDs family. Similar to TMDs, the mobility of 2D BP is also dependent on thickness. At a temperature of 120 K, a 15 nm thick BP exhibits hole mobility of 600 cm²/V·s along both light and heavy effective mass directions. To reach up to 1000 cm²/V·s. Remarkably, monolayer BP has been reported to

possess ultra-high hole mobility on the order of 10,000 cm²/V·s along with exceptional elastic properties.⁷³ Additionally, BP demonstrates a moderate current on/off ratio ranging from approximately 10⁴ to 10⁵.^{74,75} At room temperature, transistors employed from 5 nm thick BP nanosheets have shown a current on/off ratio of 10⁵ while exhibiting excellent current saturation characteristics.⁷⁶

Black phosphorus is also characterized by its puckered structure, which results in inplane anisotropy and gives rise to unique angle-dependent carrier mobility properties. Previous theoretical studies have indicated that both electron and hole mobilities in BP are anisotropic and asymmetric, with holes exhibiting higher mobility along both the zigzag and armchair directions. Specifically, the mobilities of electrons and holes in the zigzag direction are generally greater than those in the armchair direction, except in the case of monolayer BP, where the zigzag direction shows higher electron conductivity but lower hole conductivity. Nhis anisotropic behavior is primarily attributed to the differing effective masses of electrons and holes, which significantly influence transport characteristics. The remarkable angle-dependent properties of BP provide researchers with a new level of design flexibility for creating innovative optoelectronic and electronic devices that are not feasible with existing 2D materials.

Overall, these unique structural characteristics and material properties make BP an attractive material for a variety of applications in electronics and optoelectronics. As research continues to explore its capabilities and address challenges related to stability and scalability, BP holds great promise for future technological advancements in these fields.

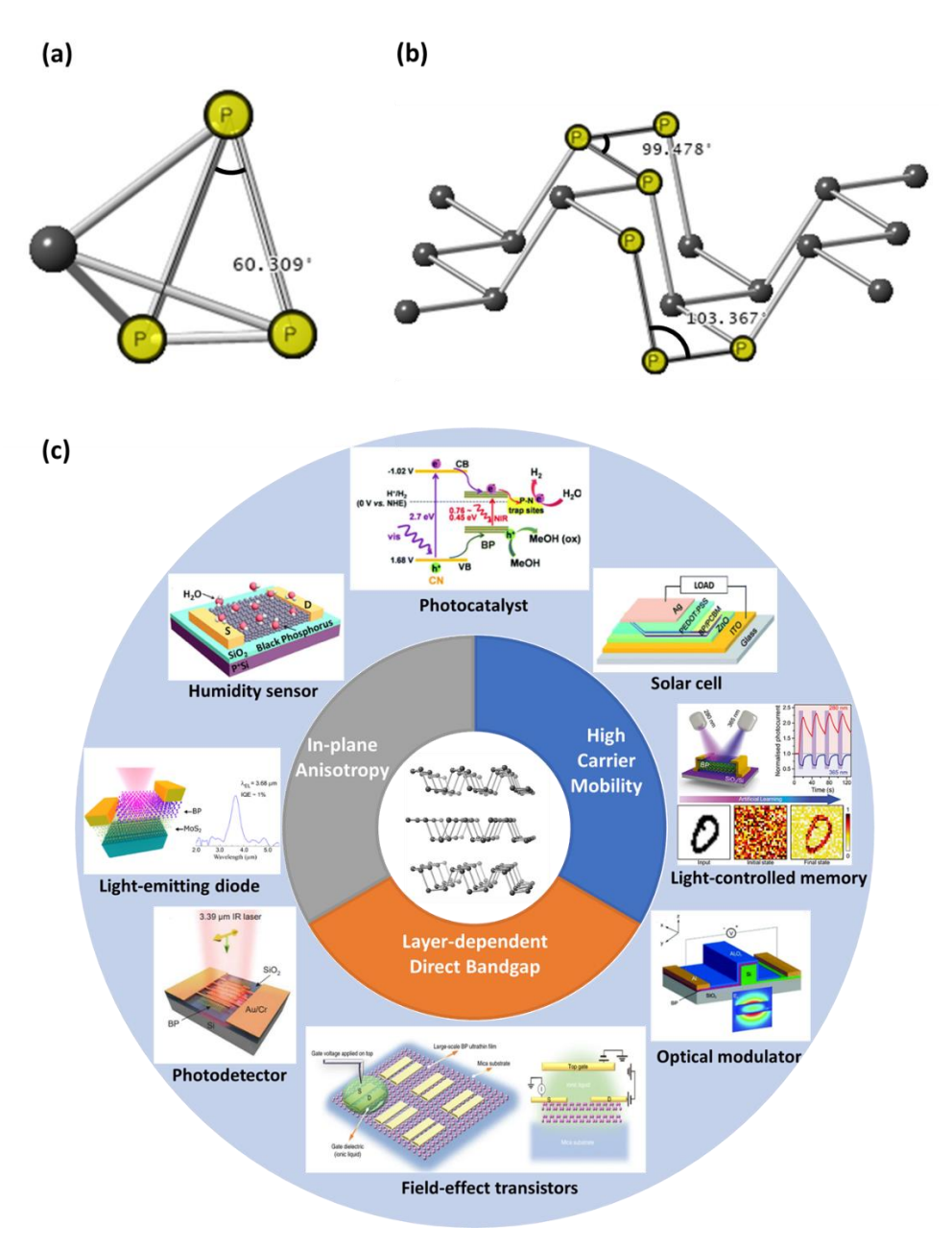


Figure 1.1 Schematic representation of (a) the tetrahedral WP P4 molecule, (b)molecular structure of monolayer phosphorene, and (c) the properties and corresponding applications of low-dimensional BP.^{83–90}

1.4 Synthesis of 2D BP

Since the identification of its semiconducting properties in 2014, 2D BP has attracted significant attention as a p-type semiconductor with considerable potential for various

applications.⁹¹ The performance of BP in nanoelectronics is heavily influenced by its manufacture techniques. Table 1-1 provides a summary and comparison of the electrical performance of 2D BP nanoflakes and thin films produced through different manufacturing methods.

Table 1-1 Comparison of 2D BP nanoflakes and thin films produced using various fabrication techniques.

| Manufacture | Thickness | Lateral | On/off | Hole mobility | Ref. |
|------------------------|-----------|-----------|-----------------|----------------------------------------------------|------|
| method | (nm) | dimension | ratio | (cm ² V ⁻¹ s ⁻¹) | |
| | | (μm) | | | |
| Mechanical | 5-10 | ~ 5 | 10 ⁵ | ~ 1000 | [24] |
| Exfoliation | | | | | |
| Mechanical | 5 | / | 10 ⁴ | 286 | [68] |
| Exfoliation | | | | | |
| Liquid-Phase | 5-20 | Few | 10^{3} | 0.58 | [92] |
| Exfoliation | | | | | |
| Solvent | 16-128 | Several | 10 ⁴ | 50 | [93] |
| Exfoliation | | | | | |
| Rapid thermal | 0.6 | Several | 105 | 337 | [94] |
| thinning | | | | | |
| Ar ⁺ plasma | 2-10 | Several | 10 ⁵ | 1150 | [95] |
| thinning | | | | | |

| Ion | 20 | <10 | ~ 10 | ~ 70 | [96] |
|----------------|--------|----------|----------|------------|------|
| bombardment- | | | | | |
| Free plasma | | | | | |
| etching | | | | | |
| Ozone | ~ 5 | ~ 40 | 132 | 59 | [97] |
| treatment | | | | | |
| RP to BP | 50 | 4000 | 200 | 0.5 | [98] |
| conversion | | | | | |
| Epitaxial | 5-10 | Hundreds | 10^{6} | 1400 | [99] |
| nucleation and | | | | | |
| lateral growth | | | | | |
| Pulsed laser | 1.1-12 | 10^{3} | / | 213 (295K) | [87] |
| deposition | | | | 295 (250K) | |

One of the key advantages of BP is its weak vdW interlayer interactions, which allow for easy exfoliation into single or few-layer nanosheets. ¹⁰⁰ This method is straightforward and able to produce high-quality 2D BP with minimal defects, though at relatively low yields. The thin layers produced through exfoliation typically measure only 5-50 µm², which is inadequate for meeting the demands of practical applications like integrated circuits. The pro-thinning treatments are often applied post-exfoliation to increase yields while allowing for adjustments in sample size, including thickness and dimensions. ¹⁰¹ However, challenges remain; issues such as plasma bombardment damage, non-uniform treatment from reactive oxygen species and UV light, and the

potential for amorphous phases or phase transitions during thermal processes and laser pruning have not been adequately addressed in the literature. Furthermore, the impact of surface treatment techniques on the electrical properties of the BP surface and heterojunction interfaces, as well as their effects on carrier transport in treated BP thin films and heterostructures, have not been thoroughly investigated. This gap limits the broader application of BP in innovative engineering solutions. In contrast to top-down methods that often require additional post-processing steps, there is a growing emphasis on developing wafer-scale bottom-up growth techniques for high-quality 2D films. Existing well-established methods for growing typical 2D materials at wafer scale could provide valuable insights for producing other 2D materials, marking a primary goal for future advancements in this field. However, achieving uniform growth of BP over large areas presents a significant hurdle in the fabrication and integration of various BP-based electronic, photonic, and mechanical devices. This challenge hinders the full realization of BP's potential in current semiconductor applications, such as integrated circuits. Although recent studies have made progress in the large-area development of 2D BP, only a few have successfully achieved largescale growth using bottom-up methods. This progress is crucial for advancing research and application development involving BP.

1.5 Transfer techniques for 2D materials

Transfer techniques are crucial for integrating 2D materials into a variety of functional applications. Among these methods, dry transfer and wet transfer are the two primary approaches used in device fabrication. 103,104

Dry transfer methods have emerged as a promising approach for the fabrication of 2D heterostructures. These techniques typically involve using a polymeric stamp or film

to pick up and transfer 2D material flakes from one substrate to another even without the use of solvents. These techniques offer several advantages but also come with some limitations. One of the most notable benefits is the ability to produce ultra-clean interfaces between layers, which is crucial for achieving optimal electronic performance in heterostructures. 105 Contamination can significantly degrade device characteristics, making this cleanliness a key factor in device quality. Dry transfer techniques also facilitate the creation of complex multilayer stacks with precise control over layer sequence and orientation, allowing for the fabrication of custom-designed heterostructures with tailored properties. 106,107 Another important advantage is the prepatterning capability. This method allows for pre-patterning of 2D materials before transfer, enabling the construction of complex device architectures designed for specific applications. This feature greatly expands the possibilities for device design and functionality. 108 Additionally, dry transfer methods minimize chemical exposure, avoiding the use of solvents and etchants that can potentially damage or contaminate the 2D materials. This is particularly beneficial for sensitive materials that may degrade upon exposure to chemicals. However, dry transfer methods also have some disadvantages that need to be considered. Despite being dry, some transfer methods still involve polymers that can leave residues on the 2D material surface. 109 These residues can affect the electronic properties of the transferred materials. The process of picking up and releasing 2D flakes can potentially cause mechanical damage, such as cracks or wrinkles, especially for large-area transfers. 110 This damage can compromise the electrical and mechanical properties of the transferred materials. Many dry transfer techniques rely on temperature control to manage adhesion between the polymer stamp and the 2D material. This temperature dependence can make the process sensitive and potentially limit the types of materials that can be transferred.¹¹¹



The complexity of dry transfer methods, which often require precise control over various parameters such as temperature, pressure, and alignment, can make the process challenging to master and potentially less reproducible. It is also worth noting that some dry transfer techniques may not be suitable for all types of 2D materials, particularly those that are highly air-sensitive or have strong adhesion to their growth substrates. While some dry transfer methods are compatible with large-area transfers, scaling up these processes for industrial production while maintaining the quality and precision of lab-scale transfers remains challenging. 114,115

Wet transfer methods, which typically involve an intermediate polymeric carrier like poly(methyl methacrylate) (PMMA), offer several advantages and disadvantages compared to dry transfer techniques for 2D materials. One of the primary advantages of wet transfer is its capability to handle larger areas of 2D materials, making it suitable for scaling up device fabrication. This is particularly important for applications that require large-area coverage or mass production. The polymeric carrier used in wet transfer also serves as a protective layer during the transfer process, helping to maintain the integrity of the 2D material as it is moved from one substrate to another. This protection can be crucial for more delicate or sensitive materials. Wet transfer methods are also known for their versatility, being compatible with a wide range of 2D materials and substrates. This flexibility allows researchers to experiment with various material combinations and device structures. Additionally, as a well-established and widely used technique, wet transfer benefits from extensive research and optimization, making it a reliable choice for many applications.

However, wet transfer methods also come with significant drawbacks. One of the most notable disadvantages is the introduction of polymer residues on the transferred 2D

structural defects in the 2D material, further impacting its quality and functionality. 124,125 Another concern with wet transfer is the potential for chemical contamination. 126 The exposure to solvents and etchants during the process can lead to undesired chemical interactions with the 2D material, potentially altering its properties. Indeed, the selection of appropriate polymers and solvents for transferring 2D materials becomes crucial due to the potential for undesired chemical interactions during the wet transfer process. The polymer must be chemically compatible with the 2D material to avoid reactions or degradation that could alter its intrinsic properties. Similarly, the solvent used to remove the polymer should effectively clean the surface without damaging or contaminating the 2D material. Etchants used in the process must effectively release the material from its growth substrate without causing chemical modifications or introducing impurities. The combination of polymer and solvent also affects the mechanical stress applied to the 2D material during transfer, potentially causing structural defects if not properly managed. Some polymers may leave persistent residues that are difficult to remove completely, altering the electronic properties of 2D materials. Furthermore, the transfer process can affect the stability of sample in ambient conditions, making the choice of polymer and solvent important for preserving its environmental stability.

material. 122,123 The transfer process can also introduce wrinkles, cracks, and other

Despite the challenges associated with wet transfer techniques, they remain necessary in 2D material research and device fabrication. Their ability to handle large areas and compatibility with a diverse range of materials and substrates make them crucial for numerous applications. Recognizing the limitations of traditional methods, recent studies are increasingly focusing on tailoring the selection of polymers and solvents to

the unique properties of specific 2D materials and the requirements of intended applications. This customized approach is essential due to the varying sensitivities of different 2D materials to chemical interactions and mechanical stresses. For example, while PMMA is often suitable for transferring graphene, more delicate materials such as phosphorene or TMDs may necessitate alternative polymers or transfer methods to preserve their intrinsic properties. Current researches are also aiming to address the limitations of wet transfer, focusing on reducing polymer residues, minimizing defects, and improving overall transfer quality. As these improvements continue, wet transfer methods are likely to remain an important tool in the development and production of 2D material-based devices. ^{127,128}

The choice between dry and wet transfer methods ultimately depends on the specific requirements of the application at hand. For instance, applications demanding high-quality interfaces and minimal contamination may favour dry transfer techniques, while those aiming for large area transfer might still rely on wet methods. Recent advancements have also led to the development of hybrid or quasi-dry transfer methods that aim to combine the advantages of both approaches. 129,130 As the field of 2D materials continues to evolve, we can anticipate the development of novel transfer techniques. These emerging methods will likely bridge the gap between existing dry and wet transfer approaches, offering innovative solutions to current limitations.

1.6 Objective of the research

The recent increase in interest surrounding 2D materials and their various applications has led to a considerable amount of research. Among these materials, substantial attention has been directed toward the dynamic tuning of interlayer structures to meet the demands of technological advancements. Strain engineering, due to its low cost



and straightforward implementation, has emerged as a promising strategy for enhancing the functionality of next-generation optoelectronic devices.

Among the various 2D materials, BP stands out due to its high in-plane anisotropy, making it an ideal candidate for novel optoelectronic applications that exploit anisotropic characteristics. The investigation of ultrathin BP nanosheets presents a unique opportunity to explore these anisotropic properties in greater detail. In contrast to other 2D materials, the unique structural characteristics of BP enable modified responses to strain, resulting in improved performance in optoelectronic devices.

The novelty of researching the anisotropic characteristics of ultrathin BP nanosheets lies in their potential to revolutionize device design and functionality. By understanding how strain affects these properties, researchers can develop advanced optoelectronic devices with improved efficiency and adaptability. This focus on BP not only contributes to the broader field of 2D materials but also positions it as a key player in the future landscape of flexible electronics.

To comprehensively investigate the various characteristics of 2D BP, it is essential to study the material across different device categories. A critical prerequisite for such investigations is the successful transfer of large-scale 2D materials from their growth substrates to a variety of target substrates. This transfer process is fundamental as it enables the integration of 2D BP onto diverse substrates, facilitating the exploration of its properties across multiple device platforms.

Among the various transfer methods available, wet transfer techniques—utilizing common polymers such as PMMA or polystyrene (PS) as adhesive layers—are widely regarded as the predominant approach for transferring large-scale 2D materials. Numerous efforts have been made to address and alleviate the challenges associated

with the wet transfer process for 2D materials. These efforts include optimizing the transfer process itself, exploring alternative supporting polymer films, and carefully selecting suitable solvents that aid in delamination.

Despite the widespread adoption of wet transfer techniques and ongoing efforts to meet associated challenges, there remains a significant need for further research and development focused specifically on the wet transfer of large-area BP thin films. This necessity arises from the immense potential and unique properties of BP for a wide range of device applications. As researchers aim to leverage the capabilities of 2D BP in practical wafer-scale applications, understanding and refining the wet transfer process will be crucial.

1.7 Organization of thesis

The organization of the thesis is as follows:

Chapter 1 Introduction: This chapter begins with an overview of common 2D vdW layered materials, highlighting their unique properties and diverse applications. It then provides a brief introduction to BP, followed by the discussion of its material structure and fundamental characteristics. The chapter also explained how synthesis methods may influence the performance of BP-based nanoelectronic devices. Finally, it addresses the importance of transfer techniques in the fabrication of BP devices.

Chapter 2 Experimental methods: This chapter outlines the experimental techniques employed in this thesis. It starts with a discussion of the fabrication processes used to prepare ultrathin 2D materials. Next, it details the methods used for characterizing samples and assembling BP-based electronic devices. The chapter concludes with a description of the setup for evaluating the electrical performance of these devices.



Chapter 3 Strain engineering for tuning polarized Raman spectra of BP nanoflakes: In this chapter, an electromechanical device is employed for variable biaxial strain application to explore the anisotropic Raman response of ultrathin BP nanosheets.

Chapter 4 Clean transfer method for preparing centimeter-scale BP thin films on silicon substrates for field-effect transistors: This chapter present a wet transfer method that utilizes EVA polymer along with an EG solution to successfully transfer high-quality BP thin films onto centimeter-scale silicon substrates. After completing this successful wet transfer, a FET array was created, showcasing remarkable uniformity and continuity.



Chapter 2 Methodology

This chapter outlines the primary experimental methods employed in this thesis. The preparation of black phosphorus (BP) nanoflakes was achieved through mechanical exfoliation, while BP thin films were fabricated using pulsed laser deposition (PLD), a widely recognized physical vapor deposition (PVD) technique.

Following fabrication, the BP nanoflakes were dry transferred onto the substrate for device construction, whereas the BP thin films underwent a wet transfer process. The material characteristics were evaluated using a variety of techniques, including X-ray diffraction (XRD), Raman spectroscopy, and high-resolution transmission electron microscopy (HRTEM) to assess the crystalline phase and quality of the materials. To characterize the surface topography and thickness of the samples, atomic force microscopy (AFM) was utilized.

For the piezoelectric substrate, we employed single crystalline (1-x)[Pb(Mg₁/₃Nb₂/₃)O₃]-x[PbTiO₃] (PMN-PT), which generates strain when subjected to an electric field. A 532 nm laser served as the excitation source for our experiments. The current-voltage (I-V) characteristics of the devices were measured using a semiconductor analyser.

2.1 Preparation methods of 2D BP

Mechanical exfoliation and PLD are two prominent techniques for preparing 2D materials, each with distinct advantages and drawbacks. Mechanical exfoliation is known for producing high-quality materials with minimal defects and low-temperature requirements, but it is labour-intensive and offers limited control over thickness and

uniformity. In contrast, PLD provides versatility in material deposition, precise control over film thickness, and the ability to maintain stoichiometry, making it suitable for complex multi-component films. However, PLD can be more complex and costly due to the need for specialized equipment. In this thesis, we employed both mechanical exfoliation and PLD to prepare 2D BP and subsequently fabricated devices for related testing.

Table 2-1 Comparison summary: Mechanical Exfoliation vs. PLD

| Feature | Mechanical Exfoliation | PLD |
|------------------------|---------------------------|-------------------------|
| Quality | High quality but variable | High quality with |
| | | stoichiometric control |
| Preparation difficulty | Easy | Difficult |
| Scalability | Limited | More scalable with |
| | | automation |
| Control over thickness | Limited | Relatively higher |
| Size of sample | Micron order | Cm-level |
| Cost | Relatively low | Higher due to equipment |

2.1.1 Mechanical exfoliation

Mechanical exfoliation is one of the most widely employed methods for fabricating 2D nanoflakes. This technique involves applying a force to overcome the vdW interactions between the layers of a bulk crystal, typically using adhesive tape. Importantly, the in-plane covalent bonds within each layer remain intact, enabling the extraction of monolayer or few-layer 2D flakes.

The procedure starts with applying the adhesive side of a piece of tape to the surface of the bulk crystal. The tape, now containing the adhered crystals, is repeatedly pasted onto and torn away from another adhesive surface to achieve appropriately thin and uniform nanoflakes. Subsequently, the tape with the exfoliated 2D materials is adhered to the target substrate. As illustrated in Figure 2.1, some monolayer and few-layer thin flakes remain on the substrate after the tape is removed. When an appropriate substrate is utilized, these exfoliated samples can be examined under an optical microscope.

While mechanical exfoliation is fundamentally a random method whose yield is greatly influenced by different factors, it can produce high-quality samples with clean surfaces on various substrates at room temperature. The BP nanoflakes utilized in this thesis were obtained through mechanical exfoliation from bulk crystals purchased from HQ Graphene.

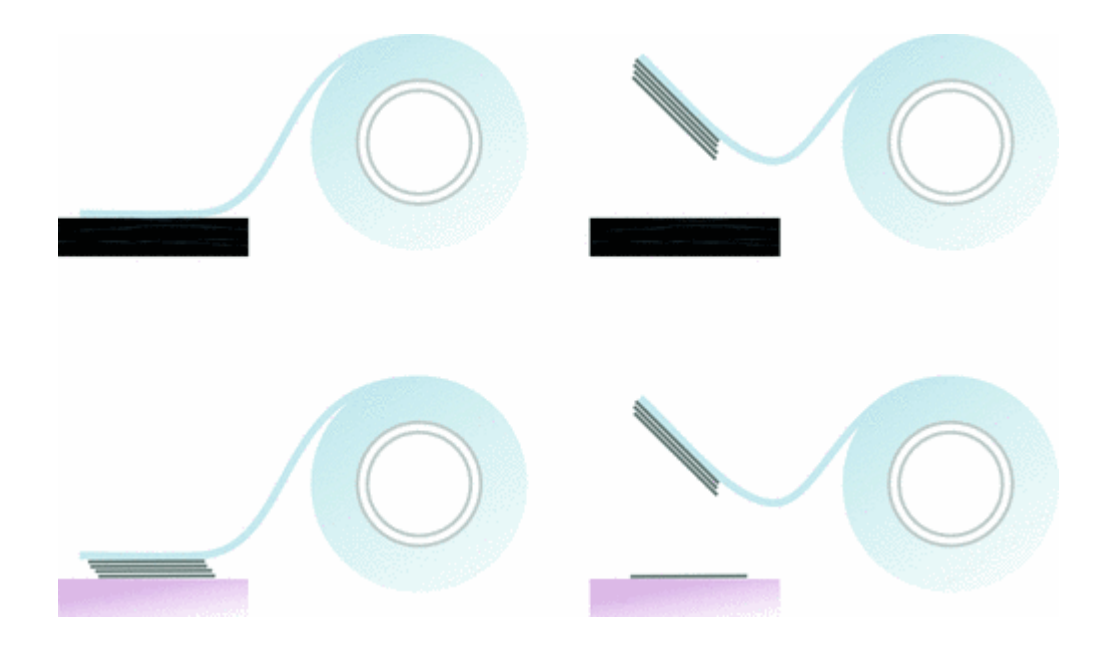


Figure 2.1 Schematic illustration of mechanical exfoliation process. ¹³¹

2.1.2 Pulsed laser deposition approach

Pulsed Laser Deposition is a versatile PVD technique widely utilized for the fabrication of thin films. In this process, a high-energy pulsed laser beam is focused onto a target material within a vacuum chamber, resulting in the vaporization of the target and the formation of a plasma plume. This plume consists of energetic particles that travel towards a substrate, where they deposit and coalesce to form a thin film (shown in Figure 2.2). PLD is renowned for its ability to produce high-quality crystalline films with precise control over composition and thickness, making it suitable for various applications, including microelectronics and optical devices.

The PLD process can be conducted under ultra-high vacuum conditions or in the presence of background gases, enabling tailored atmospheric conditions that enhance film quality. Key advantages of PLD include its adaptability to different materials, the capability to create multi-component films while maintaining stoichiometry, and relatively low substrate temperature requirements. However, challenges such as slower deposition rates and higher costs compared to other methods can limit its use primarily to high-tech applications.

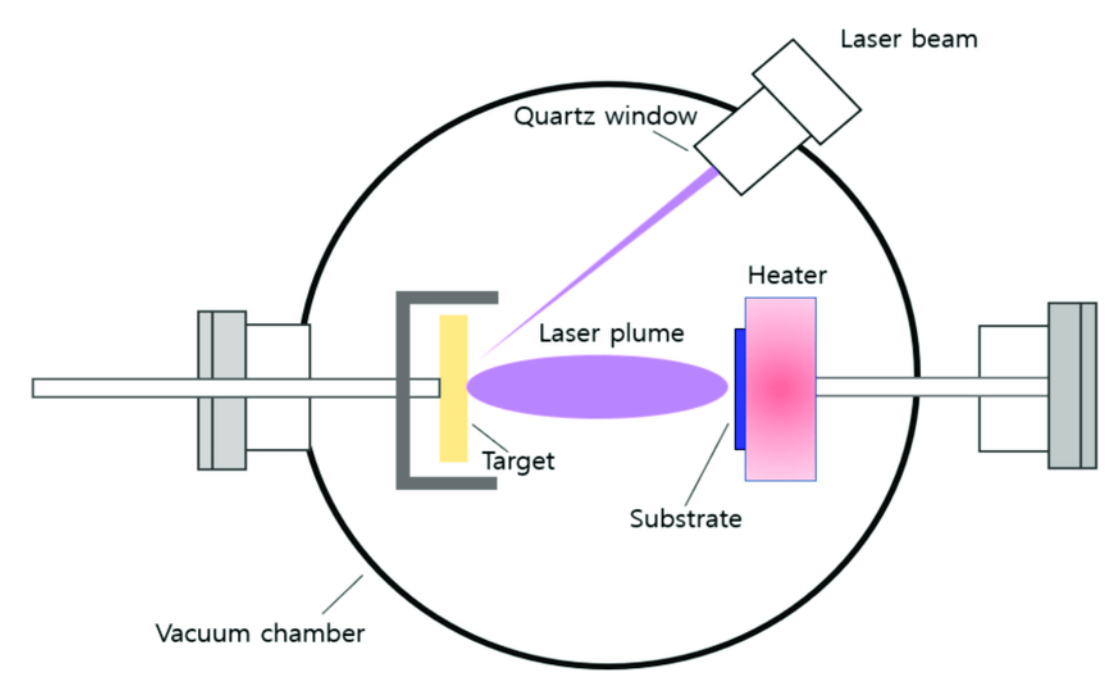


Figure 2.2 Schematic diagram of the main components within a PLD system¹³²

In this thesis, few-layer BP thin films were prepared using PLD, following established methodologies. To guarantee a clean interface, a surface-stripped mica substrate measuring 1 cm by 1 cm was placed directly into the growth chamber for BP deposition.

Throughout the deposition process, the mica substrate was rotated while the BP crystal holder stayed in place, which ensured uniform deposition and stability of the plasma plume. After the deposition was finished, dry nitrogen gas was introduced into the growth chamber, and the sample holder was removed from the heater to promote rapid cooling of the BP film to room temperature. The samples were then transported in sealed containers filled with an inert gas to avoid degradation.

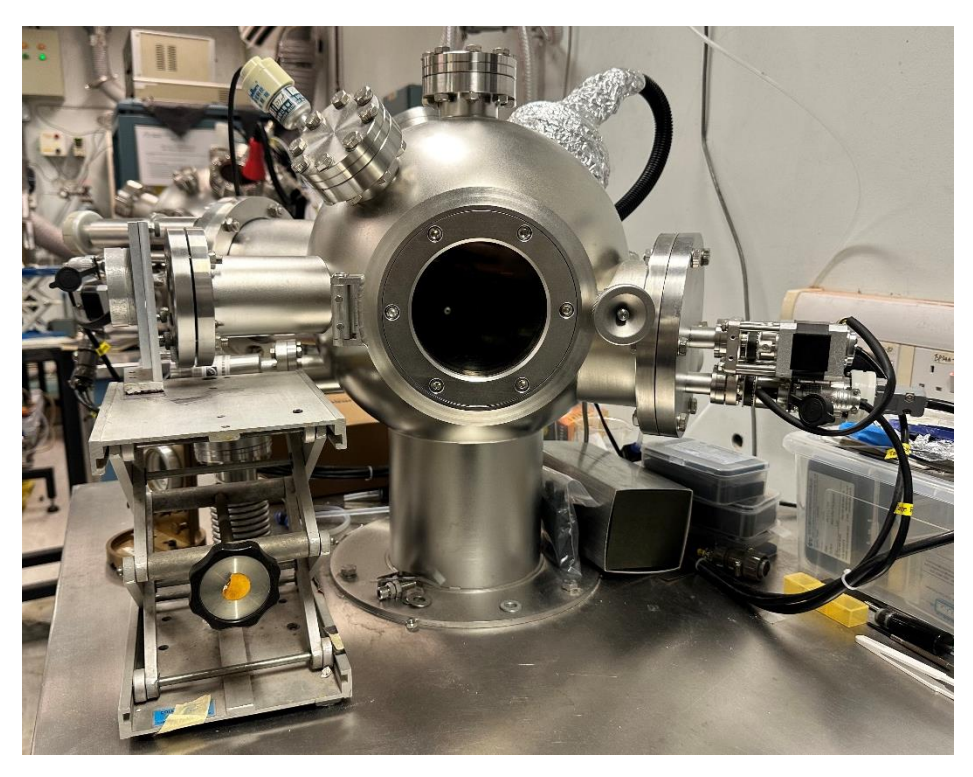


Figure 2.3 Photo of the PLD chamber utilized for BP thin film deposition

2.2 Characterization process for 2D BP

2.2.1 Optical microscope

The optical microscope is a straightforward and effective tool for obtaining information about the location, shape, and thickness of sample materials. Its operating principle relies on the interference of reflected light at distinct media interfaces. When a sample is added, it causes changes in optical paths and disturbances in opacity, leading to an optical contrast between the bare substrates and the 2D materials. Optical microscopes utilize visible light to illuminate samples, allowing for the visualization of fine details. They can achieve magnifications ranging from a few times to several thousand times, making them invaluable in materials science for characterizing thin films and nanostructures.

In comparison to other substrates, silicon covered with 285 nm of silicon dioxide (SiO₂/Si) is the most frequently utilized for the observation of 2D materials. The choice of substrate significantly influences the quality of the optical contrast observed. In the case of SiO₂/Si, part of the incident light is transmitted through the silicon dioxide layer, while another portion is reflected at each interface between the air, SiO₂, and silicon. The intensity of the light that is collectively reflected changes due to interference effects and is affected by factors like sample thickness, absorption coefficient, and differences in refractive index.

In comparison, mica is another substrate utilized in this thesis. Mica provides a relatively flat and smooth surface that facilitates the growth of 2D materials; however, it generally offers lower optical contrast than SiO₂/Si due to its transparency and refractive properties. In our experiments, there is a notable distinction between the mica with PLD-deposited BP thin film and the bare mica substrate.

2.2.2 X-ray diffraction

X-ray diffraction is a powerful non-destructive technique used to investigate the crystallographic structure of materials. It operates by irradiating a sample with incident X-rays and measuring the angles and intensities of the scattered beams that emerge from the material. A key application of X-ray diffraction (XRD) is the identification of materials through their distinct diffraction patterns. In addition to phase identification, XRD provides insights into how the actual structure of a material deviates from its ideal configuration due to internal stresses and defects. X-rays are a form of electromagnetic radiation, while crystals consist of ordered arrays of atoms. When incident X-rays interact with the electrons in the crystal lattice, they scatter, a process known as elastic scattering. This scattering generates a regular pattern of

spherical waves, which interfere with one another. Constructive interference occurs at specific angles, leading to observable reflections in the diffraction pattern, as described by Bragg's law: $2d\sin\theta=n\lambda$, where d is the distance between parallel diffracting planes, θ is the incident angle, n is an integer, and λ is the wavelength of the X-ray beam. The clarity and intensity of these reflections offer important insights into the atomic structure and properties of the crystal, such as lattice parameters, strain, grain size, and phase composition. The wavelength of X-rays generally falls within the same range as the distances between crystal lattices, from 1 to 100 angstroms, which makes them especially suitable for producing diffraction patterns. In this thesis, XRD analyses of the as-deposited BP thin films were conducted using a Rigaku SmartLab 9 kW system with Cu K α radiation ($\lambda = 1.5406$ Å).

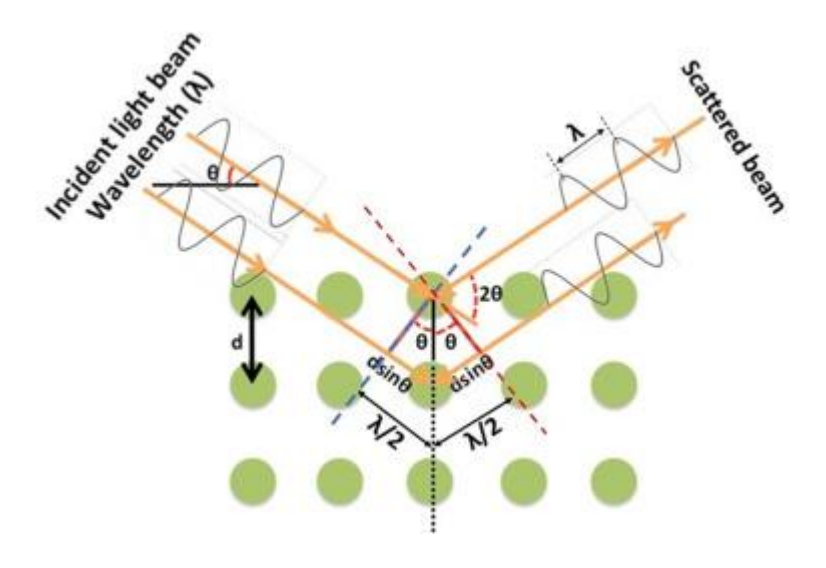


Figure 2.4 Schematic illustration of the working principle of XRD¹³³

2.2.3 Atomic force spectroscopy

The AFM measurements were conducted using an Asylum MFP-3D Infinity system in tapping mode to determine the thickness of the few-layer BPs. It is widely recognized as one of the most effective techniques for investigating materials at the nanoscale.

AFM not only provides detailed 3D topographical structures but also offers a wealth of surface information, making it invaluable for researchers and technologists. This technique can achieve atomic resolution and measure height variations down to the angstrom scale with minimal sample preparation.

The fundamental principle of AFM involves a sharp tip attached to a cantilever that scans the surface of a sample. As the tip gets closer to the material, the attractive forces between the tip and the surface led to a deflection of the cantilever. When the tip makes contact with the surface, repulsive forces take over, leading to further deflection. The two main operating modes of AFM are contact mode and tapping mode, which is also referred to as dynamic mode. In contact mode, the cantilever is pressed against the surface, and an electronic feedback loop constantly measures the interaction force to ensure a consistent deflection while performing raster scanning. This mode is effective for obtaining high-resolution topography but can potentially damage both the tip and the sample. In contrast, tapping mode reduces the contact between the tip and the surface to prevent damage to both. In this mode, the cantilever oscillates near its resonance frequency, allowing for sinusoidal motion. As the tip approaches the sample, attractive or repulsive interactions alter this motion. A feedback loop maintains a constant amplitude of oscillation rather than a static deflection, resulting in precise topographical mapping.

AFM is particularly adept at measuring surface roughness, which is crucial for characterizing material properties. It quantitatively assesses roughness parameters such as arithmetic roughness (R_a) and root-mean-square roughness (R_q) by analyzing height variations across scanned surfaces. This capability enables researchers to distinguish between smooth and rough surfaces with high fidelity. Compared to other

microscopy techniques, AFM offers unparalleled lateral resolution due to its mechanical probing method, which bypasses the diffraction limit associated with optical microscopy.

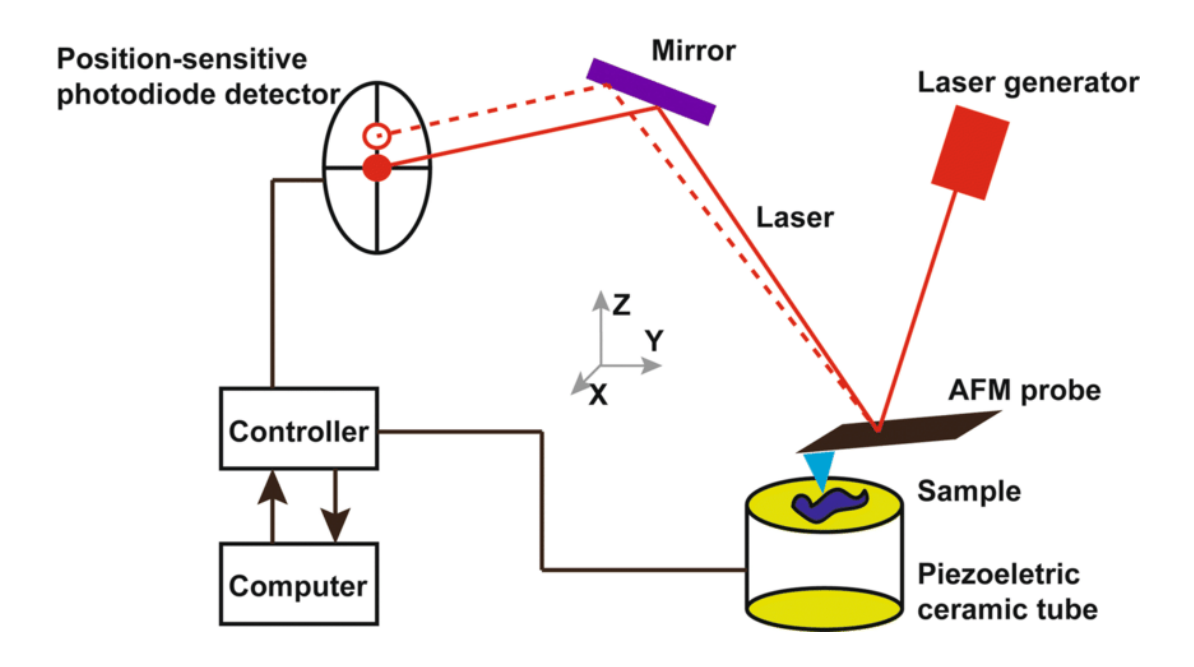


Figure 2.5 Schematic illustration of the working principle of AFM¹³⁴

2.2.4 Transmission electron microscopy

High-Resolution Transmission Electron Microscopy (HRTEM) is a powerful analytical technique used to investigate the crystal structure of materials at the atomic level. In this thesis, HRTEM analyses were conducted using a JEOL 2100F field emission transmission electron microscope to explore the crystallographic characteristics of mechanically exfoliated black phosphorus (BP) nanoflakes.

The JEOL 2100F operates at an accelerating voltage of 200 kV, providing high spatial resolution with a lattice resolution of up to 0.23 nm. This capability allows for detailed visualization of atomic arrangements within the material. HRTEM utilizes a parallel beam of electrons that transmits through thin samples, generating images based on coherent elastic scattering. The resulting high-resolution images enable researchers to

observe fine structural details, including crystal defects, phase distributions, and grain boundaries.

During the HRTEM analysis, the samples were prepared to be sufficiently thin to allow electron transmission, typically below 100 nm in thickness. This ensures that the electron beam can penetrate the sample without significant scattering losses. The high-resolution images obtained provide insights into the atomic-scale features of the nanoflakes, contributing to a deeper understanding of their structural integrity and potential applications in nanoelectronics.

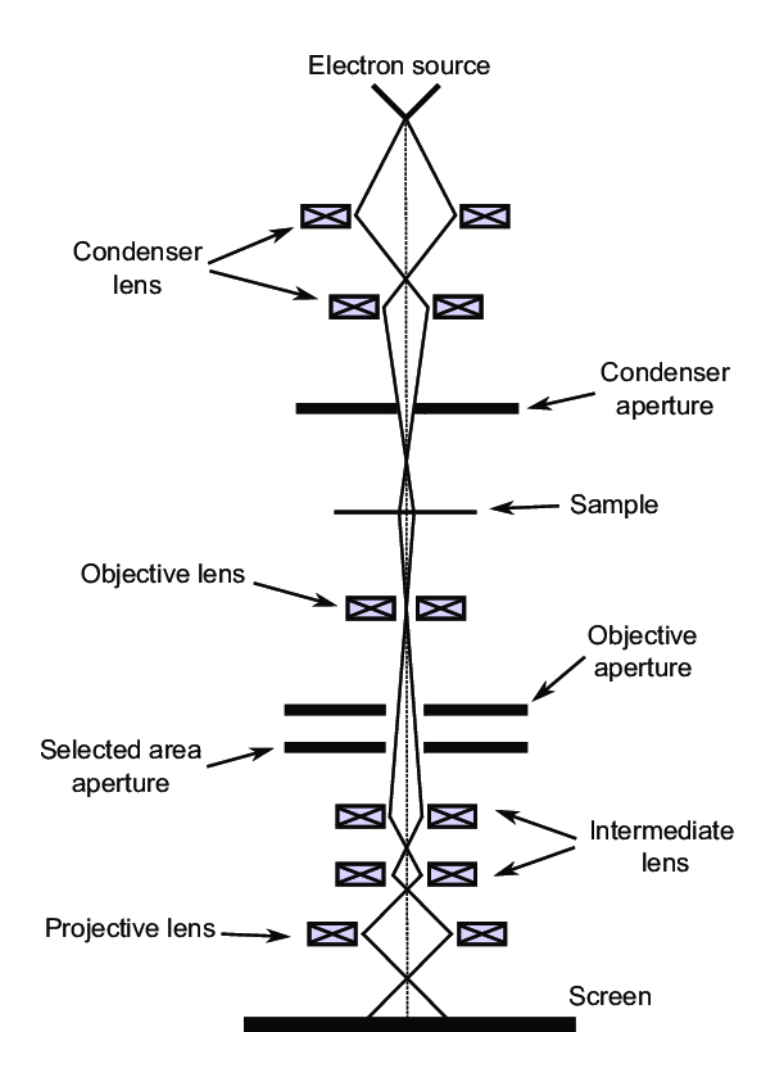


Figure 2.6 Schematic illustration of TEM¹³⁵



2.2.5 Raman spectroscopy

Raman spectroscopy is a non-destructive chemical analysis technique that provides detailed information about chemical structures, phases, polymorphs, crystallinity, and molecular interactions based on the interaction between incident light and the chemical bonds of a material. This light scattering method employs a high-intensity laser to illuminate the sample, leading to the scattering of incoming light by the molecules within it. In this process, Rayleigh scattering occurs when most of the scattered light retains the same wavelength as the incident laser, yielding no valuable data. In contrast, Raman scattering involves a small fraction of light being scattered at different wavelengths, which is dependent on the chemical structure of the specimen. In a Raman spectrum, the intensity and positions of the wavelengths of the scattered light are depicted as a series of peaks. When light strikes a molecule, it causes polarization within the molecular electron cloud due to the oscillating electromagnetic field generated by the photon. This interaction elevates the molecule to a higher energy state, forming a transient complex known as a virtual state. Because of the instability of this virtual state, the photon is quickly reemitted as scattered light.

Stokes Raman scattering, named after G.G. Stokes, occurs when a molecule absorbs energy from the photon and is stimulated to a higher vibrational state during scattering. As a result, the scattered photon loses energy, leading to an increase in. Conversely, anti-Stokes Raman scattering happens when a molecule releases energy wavelength by relaxing to a lower vibrational state; in this case, the scattered photon gains energy, resulting in a decrease in wavelength. Both Stokes and anti-Stokes processes occur at similar rates on a quantum mechanical level. Nevertheless, because of statistical distributions, specifically the Boltzmann distribution, the majority of molecules tend

to exist in their ground vibrational state. Consequently, Stokes scattering is statistically more probable than anti-Stokes scattering, making Stokes Raman scatter more readily detectable in Raman spectroscopy.

In this thesis, Raman spectra were obtained using a WITEC Confocal Raman system equipped with a 532 nm laser as the excitation source to analyze the material characteristics. Additionally, polarized Raman spectroscopy tests were conducted to further investigate the properties of mechanical-exfoliated BP nanoflakes under different strain conditions. The measurements were at the same position on the sample in 15° increments from 0° to 180°. This range corresponds to the angle between the polarization direction of the incident laser and the orientation of the sample.

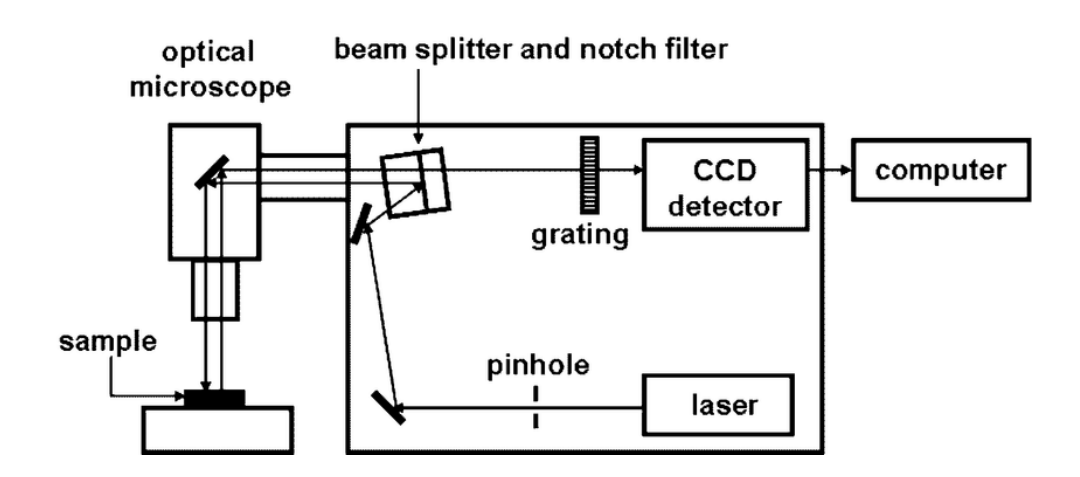


Figure 2.7 Schematic illustration of Raman spectroscopy ¹³⁶

2.3 Device fabrication process

2.3.1 Photolithography

Photolithography has emerged as one of the most widely used techniques for patterning polymers for past 30 years, serving as a method to transfer patterns from a mask to a substrate surface. This technique involves applying a light-sensitive material



known as photoresist to the surface of a substrate. A photomask containing the desired pattern is then placed over the photoresist, and ultraviolet (UV) light is shone through the mask. This exposure alters the solubility of the photoresist in specific areas, allowing for selective development that removes either the exposed or unexposed regions, thereby transferring the pattern onto the substrate. Photolithography allows for the rapid and consistent fabrication of structures with desired shapes at both micron and nanoscale dimensions, making it invaluable in various fields.

The following section outlines the detailed steps and parameters employed in our photolithography process. Initially, the substrate was placed on a spin coater, and suction was applied using a vacuum pump to secure it in place. A positive photoresist, AZ5214, was then applied to the substrate, which was chosen to achieve higher resolution in the final patterns. The spin coater's speed was subsequently adjusted: it accelerated to 500 rpm over 5 seconds and maintained this speed for an additional 5 seconds before increasing to 4000 rpm over 5 seconds and holding that speed for 30 seconds. This spinning process ensured that the thickness of the applied photoresist did not exceed 1 µm. Next, the hot plate was set to 110°C and baked the photoresist for 3 minutes. After that, we positioned the mask over the photoresist-coated substrate and aligned it in the desired orientation with the aid of a microscope. Once properly aligned, UV light was directed through the quartz mask onto the substrate for 8s, allowing the patterns from the mask to be transferred onto the photoresist. Following exposure, we applied AZ300MIF developer to selectively remove portions of the photoresist and create the desired patterns. The sample was immersed in the developer for approximately 20 seconds before being rinsed with deionized (DI) water to complete the process.

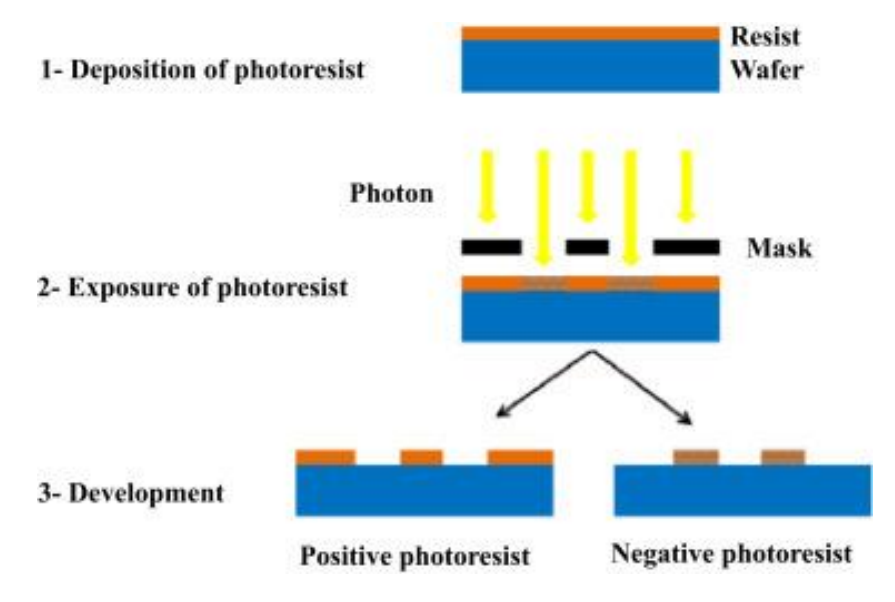


Figure 2.8 Overview of photolithography ¹³⁷

2.3.2 Electron beam evaporation

Electron Beam (E-beam) evaporation is a type of PVD that utilizes an electron beam to evaporate target materials, converting them into a gaseous state for deposition onto a substrate. This process takes place in a high vacuum chamber, where vaporized atoms or molecules condense to create a thin film coating on the substrate. The direct energy transfer from the electron beam to the target material allows for the effective evaporation of metals with high melting points, making E-beam evaporation particularly advantageous for various applications. A major advantage of E-beam evaporation is its fast deposition rates, which can vary from 0.1 nm to 100 nm per minute. This results in denser film coatings with improved adhesion to substrates. Furthermore, E-beam evaporation offers a high material utilization efficiency relative to other PVD methods, contributing to cost savings. Unlike traditional methods that heat the entire crucible, E-beam systems focus energy solely on the target material, minimizing contamination and reducing the risk of heat damage to the substrate. A multiple crucible E-beam evaporator can deposit several layers from different target

materials without breaking the vacuum, making it adaptable for various lift-off masking processes. In this study, Denton E-beam evaporation was employed to create metal electrodes. After E-beam evaporation, a lift-off procedure may be required to remove any excess metal film that does not form part of the pattern electrodes on the substrate. Typically, the metal films can be removed by submerging the substrate in acetone solution.



Figure 2.9 Photo of the Denton Explorer E-beam deposition system



2.3.3 Dry transfer

Multilayer BP nanoflakes were obtained from high-quality crystals sourced from HQ Graphene and transferred onto SiO₂/Si substrates through mechanical exfoliation. The polyvinyl alcohol (PVA) films utilized during this process were prepared by drying a 4% PVA aqueous solution on a CD for 48 hours. To transfer the flakes, they were mechanically picked up from the SiO₂/Si substrate using the PVA film. Subsequently, both the sample flakes and the PVA film were adhered to a polydimethylsiloxane (PDMS) stamp. To minimize strong interactions between the PVA film and the 2D flakes, the temperature during the picking operation was carefully controlled at 55 °C for 5 minutes. High drying temperatures can lead to significant interactions between the PVA film and the 2D materials, adversely affecting the yield rate. Once the 2D material flakes were successfully attached to the PVA film, they were oriented onto a PMNPT substrate that had pre-fabricated electrodes. To ensure effective connections between the materials and electrodes, the device was heated to 55 °C for an additional 5 minutes after alignment. Finally, to prevent the degradation of 2D BP, a layer of poly(methyl methacrylate) (PMMA) was applied over the structure.

2.3.4 Wet transfer

Following the BP thin film is deposited through PLD, a solution of EVA (Aldrich, 40 wt % vinyl acetate, 10 wt % dissolved in xylene) was spin-coated onto the sample at 1500 rpm for 60 seconds. The coated sample was then placed in an oven at 80 °C for 60 minutes to cure the EVA layer effectively. Following the curing process, the EVA/BP film was soaked in EG solvent at 50 °C for half an hour. This step aided in the separation of the EVA/BP film from the growth substrate with the help of EG. Once detached, the film was carefully transferred onto the target substrate with ensuring

alignment and integrity. To ensure proper adhesion of the transferred composite, it was then placed in a vacuum drying oven at 50 °C for half an hour. Following this, the sample was soaked in tetrahydrofuran (THF) for 30 minutes to selectively remove the EVA film, leaving behind the BP layer on the target substrate.

2.4 Device characterizations

After constructing the device, the electrical performance of the samples was evaluated using a specialized measurement system. This system comprises a probe station equipped with micro-manipulators and hyperfine micrometer probes situated within a high-vacuum chamber, and the Keithley 4200A-SCS Semiconductor Parameter Analyzer. As illustrated in Figure 2.9, the vacuum chamber features a temperature control system that enables a range of testing conditions for electrical characterization across different devices. Under microscopic observation, the micromanipulators facilitate the precise movement and positioning of the micrometer probes. Once the probes contact the device electrodes, voltage can be applied through the source, drain, and gate electrodes via the Keithley 4200A-SCS Semiconductor Parameter Analyzer. This setup allows for the measurement and analysis of various output characteristics of the device, including source-drain current-voltage (I-V) curves, gate leakage current, and transfer characteristic curves.



Figure 2.10 Photograph of the device electric measurement system



Chapter 3 Exploring the anisotropic properties of BP with PMN-PT substrates

3.1 Introduction

Compared to their bulk counterparts, two dimensional (2D) materials exhibit numerous unique properties that make strain engineering a highly promising approach for discovery and manipulation. Their ultrathin structure and exceptional mechanical flexibility allow them to sustain much larger strains without fracturing, unlike bulk materials which typically crack at low strains. This high deformability enables a wider tunability of their properties through strain. Moreover, the confinement of the crystal structure to a two-dimensional plane makes their electronic and optical properties highly sensitive to lattice distortions induced by strain, enhancing the modulation of band structure and related properties. . 139,140

In addition, most of the atoms in 2D materials are exposed at the surface, so strain directly alters atomic bond lengths and angles, strongly affecting electronic and optical responses—effects that are less pronounced in bulk materials where many atoms are buried inside. ^{141,142} The ability to host spatially varying strain patterns, such as wrinkles or strains induced by patterned substrates, allows nanoscale modulation of band structure and properties that are difficult or impossible to achieve in bulk materials. Furthermore, external strain can be precisely applied to 2D materials, enabling dynamic and reversible control of their behavior, which bulk materials generally lack due to their brittleness and thickness. ^{143,144}

Strain engineering also enhances the application potential of 2D materials by improving performance in energy storage, catalysis, and electronic/optoelectronic devices through optimized adsorption, diffusion, and carrier dynamics. ¹⁴⁵ To fully harness these unique strain-dependent properties for device applications, fundamental research is essential. Therefore, in this section, we focus on investigating the polarized Raman spectra of 2D materials under biaxial strain to gain deeper insight into their strain-dependent behavior and potential for tunable device engineering.

There are two primary methods to apply strain to 2D materials. The first involves stretching or bending a 2D material placed on a flexible substrate, which induces uniaxial strain along a specific direction. The second method employs a piezoelectric substrate to generate biaxial strain. Unlike mechanically induced uniaxial strain, biaxial strain can be precisely tuned by adjusting the voltage applied to the substrate, enabling more accurate modulation. 148,149

In this study, we utilize the single-crystalline material [Pb(Mg_{1/3}Nb_{2/3})O₃]-x[PbTiO₃] (PMN-PT) with x=0.3 as as the piezoelectric substrate due to its exceptional electromechanical properties and converse piezoelectric capabilities. PMN-PT is well known for its unique dielectric characteristics, including an exceptionally high piezoelectric coefficient (d₃₃) and electromechanical coupling factor. ^{150,151} The d₃₃ value of single-crystal bulk PMN-PT exceeds 2000 pC/N, which is roughly four times greater than that of Pb[Zr_xTi_{1-x}]O₃ (PZT) and nearly thirty times higher than that of BaTiO₃ (BTO). ¹⁵² This outstanding performance makes PMN-PT an ideal choice for generating strain in 2D materials.

3.2 Interfacial strain engineering of BP by PMN-PT substrates

Figure 3.1 presents a schematic illustration of the device fabrication process for black phosphorus (BP) on a piezoelectric PMN-PT substrate. Multilayer BP nanoflakes were mechanically exfoliated from bulk crystals obtained from HQ Graphene and deposited onto SiO₂/Si substrates. Before the transfer process, 30 nm gold (Au) thin films were deposited on both sides of the PMN-PT substrate, acting as bottom and top electrodes, respectively, using electron-beam evaporation. The few-layer BP was then dry transferred onto the PMN-PT substrate using a polyvinyl alcohol (PVA) film. To minimize interactions between the BP flakes and the substrate during this process, the temperature was maintained at 55 °C. Following the transfer, the sample was coated with PMMA to protect BP from degradation under ambient conditions. A Keithley 2410 Source Meter was employed to apply bias voltage to the PMN-PT substrate, following an initial polarization with an electric field of 10 kV/cm.

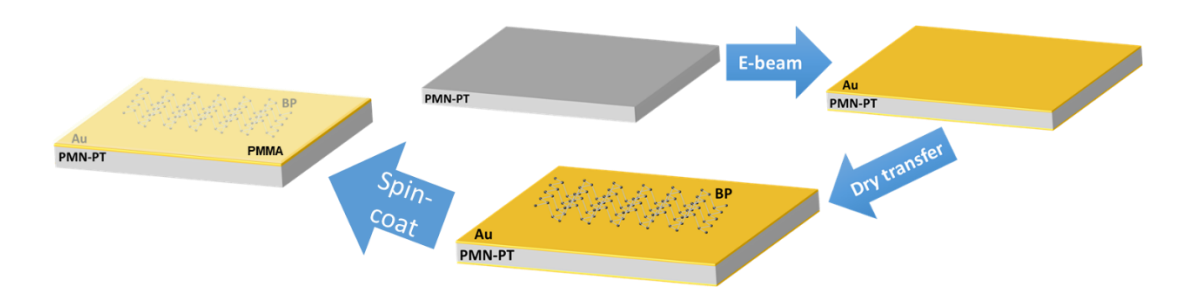


Figure 3.1 Schematic illustration of device fabrication for BP on a piezoelectric PMN-PT substrate

Previous studies have indicated that both positive and negative bias voltages can induce compressive strain.¹⁵³ In this study, an in-plane compressive strain was induced in the PMN-PT substrate by applying a 500 V bias voltage, which concurrently compressed both the BP nanosheets and the poly(methyl methacrylate) (PMMA). For

application of tensile strain, we pre-strained the PMN-PT substrate, whose recovery process takes several hours. During this time, the device was fabricated. Because the recovery force of PMN-PT is quite small, PMMA served not only to firmly secure the BP nanoflakes and prevent slipping but also to enhance the tensile strain induced by PMN-PT. As an elastic polymer, PMMA gradually returns to its original shape after compression, which amplifies the tensile strain applied to the BP nanoflakes during the recovery of substrate. As a result, negative and positive bias voltages were applied with a gradient of 0.04% strain for every 100 V to generate compressive and tensile strains, respectively, throughout this research.

Moreover, the significantly lower resistance of gold ($\sim 0.02~\mu\Omega$) compared to the PMN-PT dielectric substrate ($G\Omega$ range) ensures that nearly the entire bias voltage is dropped across the substrate. In this configuration—where the BP film resides on the substrate surface without direct electrical contacts or gating—there is neither experimental evidence nor theoretical justification to expect a substantial electric field within the BP layer (shown in Figure 3.2). The voltage gradient primarily develops across the bulk of the PMN-PT substrate, leaving the surface-mounted BP largely unaffected by the applied electric potential.

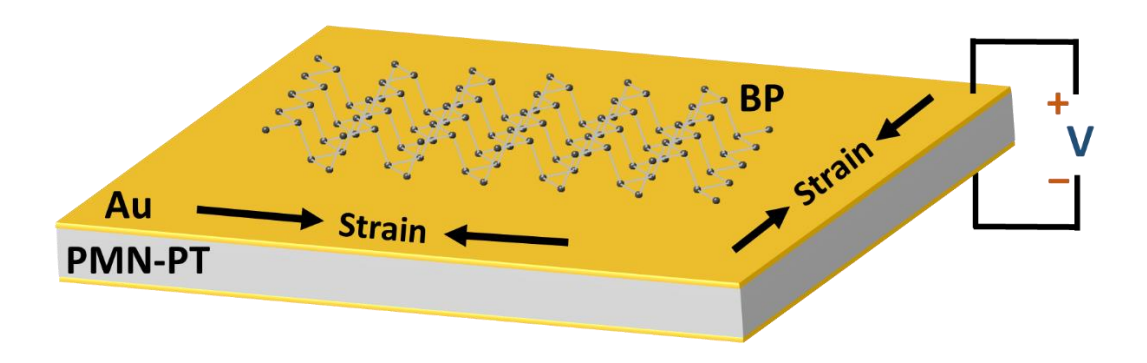


Figure 3.2 Schematic illustration of the device structure for BP on a piezoelectric PMN-PT substrate

3.3 Material characterization of BP nanoflakes

As shown in Figure 3.3, the atomic force microscopy (AFM) measurements were performed in tapping mode to assess the thickness of the few-layer BP flake, which was found to be approximately 8 nm (~16 layers), exhibiting a smooth and flat surface.

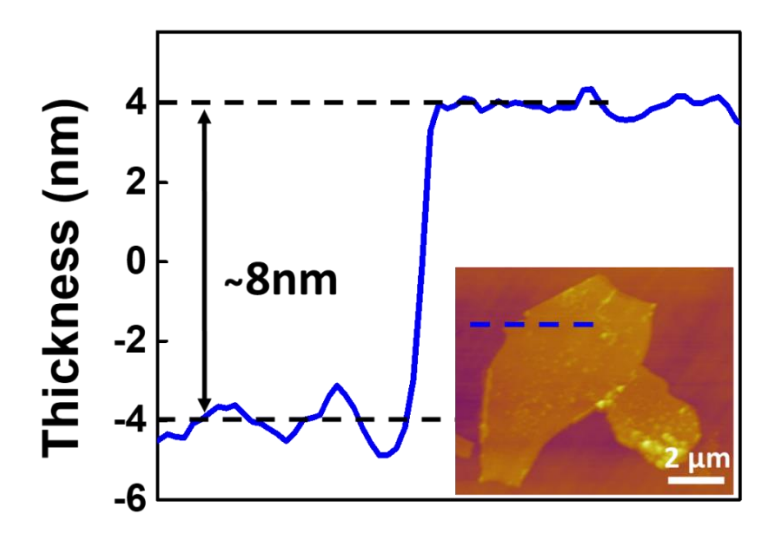


Figure 3.3 AFM height profiles of the mechanical-exfoliated BP nanoflakes. Inset: corresponding AFM image.

To further investigate the microscopic crystal structure of the mechanically exfoliated BP films, HRTEM analyses were conducted with a JEOL 2100F microscope. The planview image presented in Figure 3.4 reveals a highly ordered arrangement of BP atoms, with no apparent defects. The lattice constant measured along the 100 direction is 0.327 nm, aligning with findings from prior studies.

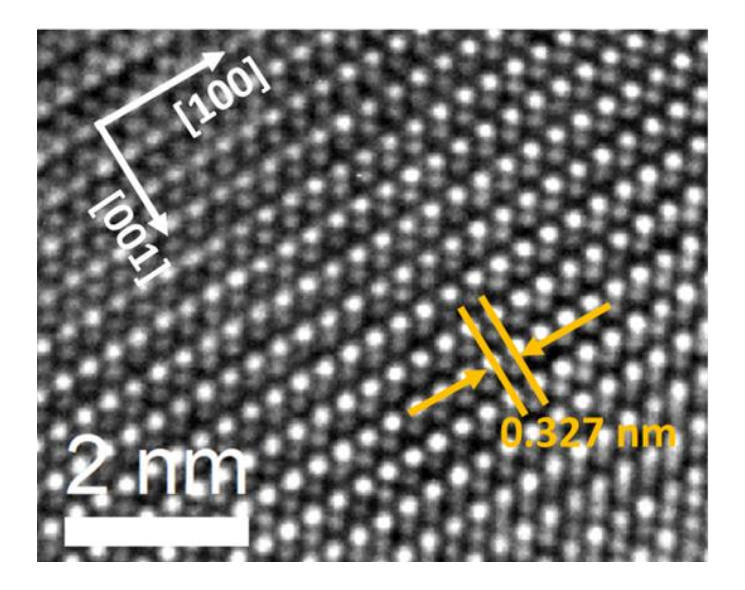


Figure 3.4 HRTEM image of the mechanical-exfoliated BP nanoflakes.

Additionally, the selected-area electron diffraction (SAED) pattern shown in Figure 3.5 indicates that the BP sample is highly crystalline and exhibits a typical orthogonal lattice structure.

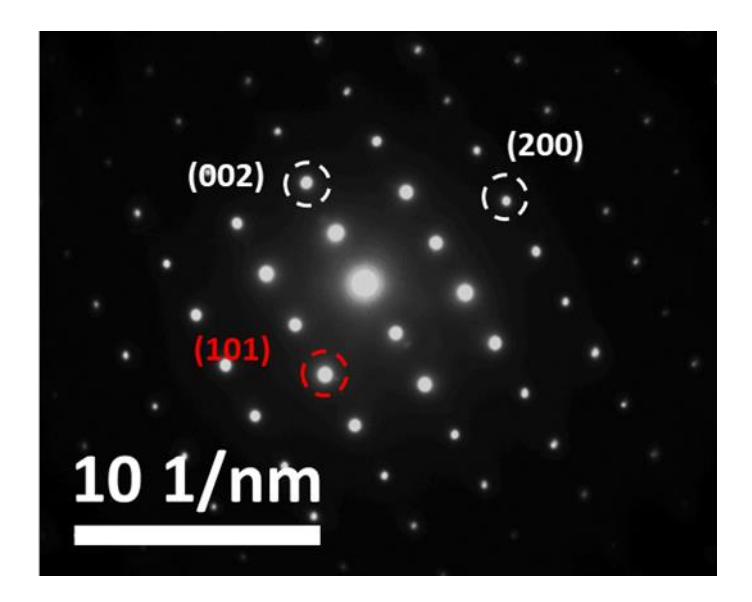


Figure 3.5 SEAD pattern of the mechanical-exfoliated BP nanoflakes.

Raman spectroscopy was employed using a WITEC Confocal Raman system with a 532 nm laser as the excitation source, featuring a spot size of 1 μ m to analyze the

vibrational and optical characteristics of the material. To prevent damage to the sample, a low laser power of less than 0.5 mW was utilized during the experiments. As illustrated in Figure 3.6, three characteristic Raman peaks were identified at 365 cm⁻¹, 442 cm^{-1} , and 471 cm^{-1} , corresponding to the out-of-plane mode (A_g^1), in-plane mode along the zig-zag direction (B_{2g}), and in-plane mode along the armchair direction (A_g^2), respectively. These findings are consistent with previous literature on BP.¹⁵⁴

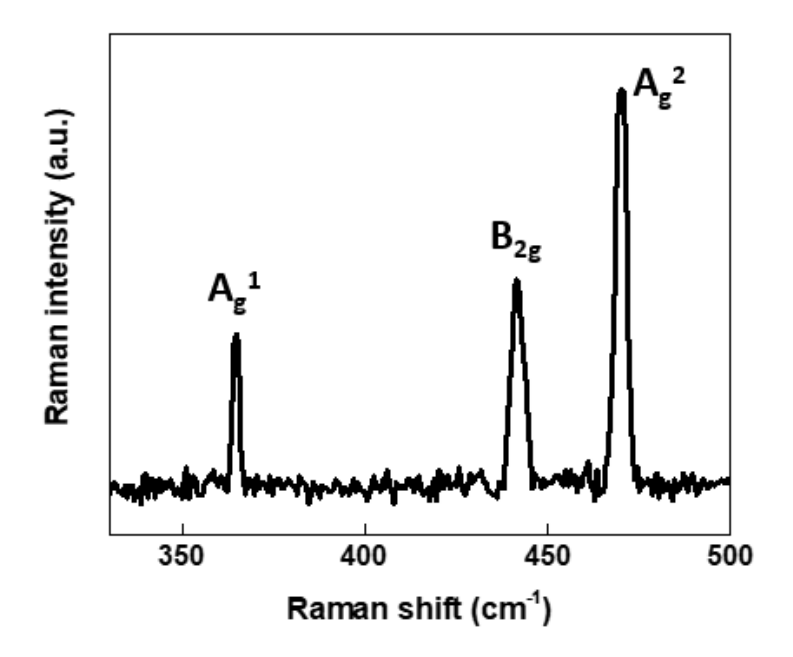


Figure 3.6 Raman spectrum of the mechanical-exfoliated BP nanoflakes.

3.4 Anisotropic characteristic of BP via polarized Raman spectroscopy

To explore the electron-photon and electron-phonon interactions in BP, polarized Raman spectra were systematically collected from a single sample. The measurements were conducted at the same position, with the polarization direction of the incident laser rotated in 15° increments from 0° to 180°, as the set-up shown in Figure 3.7. This

155

approach ensured better control over variables and enhanced data reliability, as the angle between the polarization direction and the sample orientation was carefully managed.

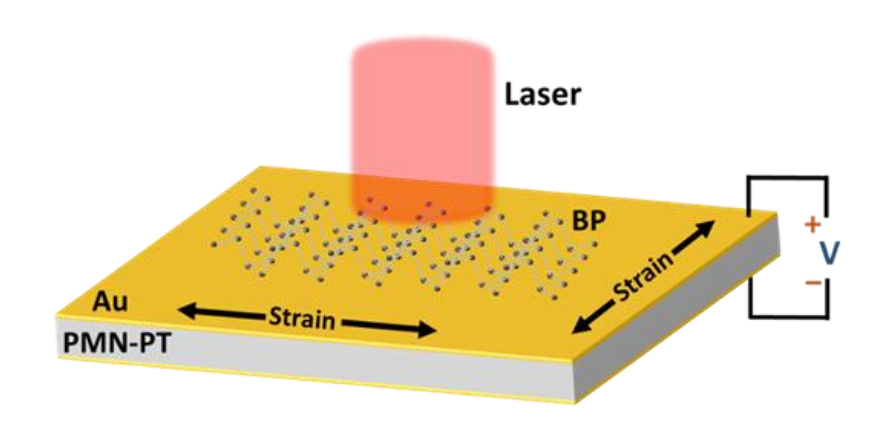


Figure 3.7 Schematic illustration of Raman spectra acquisition using an electromechanical device that applies external biaxial strain.

Figure 3.8 illustrates that the initial polarized incident laser is aligned parallel to the analyzer, revealing a significant dependence of Raman intensities for three characteristic modes on the polarization angles. Notably, both the $A_{\rm g}^{1}$ and $A_{\rm g}^{2}$ modes exhibit similar trends, diminishing at 0° and reaching their maximum intensities at 90° .

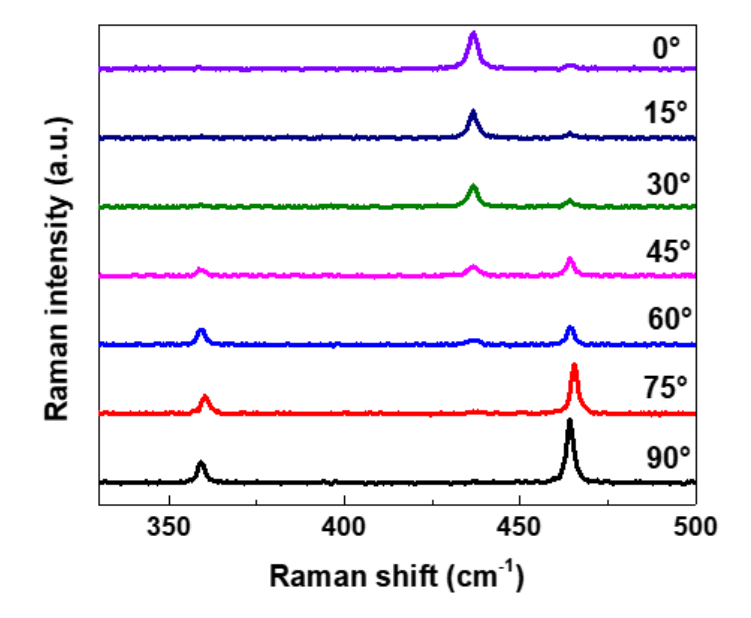


Figure 3.8 Polarized Raman spectra of BP nanosheets obtained at different polarization angles.

The intensity is governed by the vibrational symmetry of the scattering system, as dictated by the Raman selection principle. This intensity reaches its peak when the incident light polarization aligns with the atomic displacement, and its minimum when perpendicular. In monolayer black phosphorus, the $A_{\rm g}^2$ mode exhibits a distinctive characteristic: atomic vibrations predominantly occur along the armchair (x) direction. Consequently, the Raman scattering signal is most pronounced when the excitation beam polarization coincides with this x-axis. ¹⁵⁶

To highlight this behaviour, a polar plot of the A_g^2 mode is presented in Figure 3.9. The intensity fluctuation closely follows a mathematical pattern. The observed variation can be accurately described by combining a cosine-squared function of θ :

$$I(A_g) = \left[\frac{a-c}{2}\cos(2\omega - \theta) + \frac{(a+c)}{2}\cos(\theta)\right]^2$$
 3.1

In this context, θ represents the angular difference between the x-axis and the polarization direction of the incident laser; a and c present the corresponding parameters in Raman tensors of A_g mode, and ω is the angle between the zigzag direction and scattered light polarization.¹⁵⁷

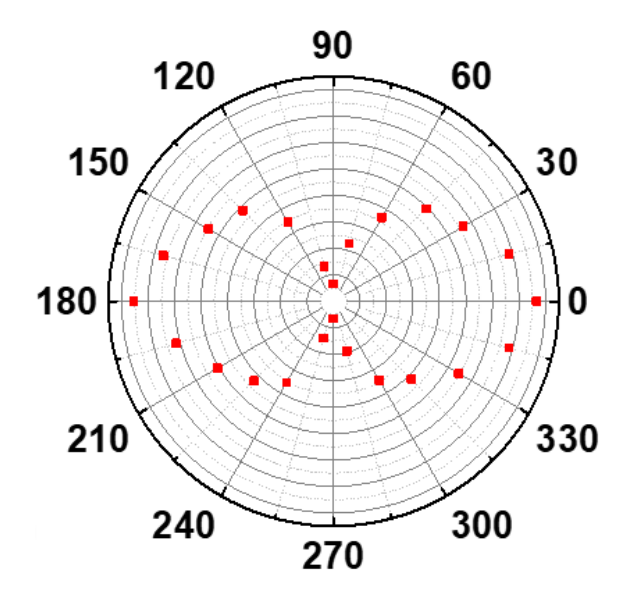


Figure 3.9 Polar plots illustrating the intensity variations of the $A_{\rm g}^{\,2}$ Raman peak

Conversely, the B_{2g} mode displays an inverse relationship. As presented in Figure 3.10, it achieves highest intensity at 0° and lowest at 90° . The observed intensity variation of the B_{2g} mode can be accurately described by a mathematical model similar to that of the A_g mode.

$$I(B_{2g}) = e^2 [\cos(2\omega + \theta)]^2$$
 3.2

In this expression, e represents the Raman tensor element specific to the B_{2g} mode. The other parameters retain their meanings from the A_g equation. The observed variations in intensity among these modes can be attributed to the anisotropic structure of BP. This anisotropy leads to distinct responses in Raman intensity based on

polarization angle, underscoring the complexity of electron-phonon interactions within this material.

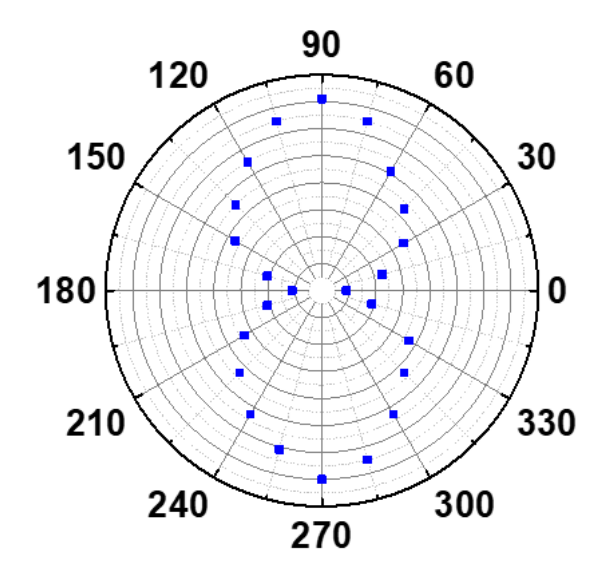


Figure 3.10 Polar plots illustrating the intensity variations of the $B_{\rm 2g}$ Raman peak

3.5 Raman spectroscopy of BP under biaxial strain

Zigzag and armchair configurations represent two fundamental types of uniaxial strain in materials science, particularly in the study of 2D materials. These configurations provide a framework for understanding how materials respond to directional stress along specific crystallographic orientations.

Biaxial strain, in contrast, presents a more complex scenario. It can be conceptualized as the superposition of these two uniaxial strains, resulting in a multidimensional stress state. While uniaxial strain is relatively straightforward to understand and apply, biaxial strain introduces additional complexities due to its multidirectional nature. In the case of biaxial strain, the applied force is not uniform across all directions, often resulting in varying strain magnitudes along different axes. This non-uniformity becomes especially significant when considering anisotropic materials, where

properties differ depending on the direction of measurement. The interplay between the inherent anisotropy of material and the non-uniform biaxial strain can lead to complex deformation patterns and property changes. Understanding these strain configurations is crucial for predicting and manipulating the properties of 2D materials, as strain can significantly influence their electronic, optical, and mechanical characteristics.

The typical Raman spectra of BP nanoflakes subjected to various biaxial tensile and compressive strains are depicted in Figure 3.11. Significantly, the application of tensile strain leads to a redshift in the three characteristic peaks, whereas compressive strain causes a blueshift. For a compressive strain of -0.2%, the shifts observed for the A_g¹, B_{2g} and A_g^2 modes were 6.2, 15.3, and 12.2 cm⁻¹/%, respectively. Conversely, under a tensile strain of 0.2%, the shifts for these modes were -6.2, -12.2, and -12.2 cm⁻¹/%, respectively. The application of strain in two-dimensional materials like BP alters the lattice constants and vibrational characteristics, leading to these shifts in Raman peaks. 158 The out-of-plane $A_{\rm g}{}^{\rm l}$ mode corresponds to vibrations of the top and bottom phosphorus atoms within the same layer moving in opposite directions, while the B_{2g} and $A_{\rm g}^{\ 2}$ modes relate to in-plane vibrations of phosphorus atoms in different orientations. Since the PMN-PT substrate produces in-plane biaxial strain, it was noted that the horizontal deformation of BP is greater than the vertical deformation, suggesting that the B_{2g} and ${A_g}^2\mbox{ modes}$ are more sensitive. The Grüneisen parameter γ serves as a measure of phonon frequency fluctuations in response to strain and is defined as:

$$\gamma = \frac{-1}{2\omega_0} \frac{\partial \omega}{\partial \varepsilon}$$
 3.3

where ω_0 and ω represent the Raman frequencies under zero and finite biaxial strain conditions, respectively, and ε is the applied biaxial strain. This can be simplified as:

$$\gamma = -\frac{\Delta\omega}{2\omega_0\varepsilon} \tag{3.4}$$

In our study, the Grüneisen parameters for the A_g^1 , B_{2g} , and A_g^2 modes with application of -0.2% compressive strain were found to be -1.28, -1.74, and -1.30, respectively. For 0.2% tensile strain, the parameters were 1.28, 1.39, and 1.30. The B_{2g} Grüneisen parameter under compressive strain is slightly greater than that under tensile strain, likely due to slippage during strain application; thus, some strain induced by the piezoelectric PMN-PT substrate may not have fully transferred to the BP nanoflakes.

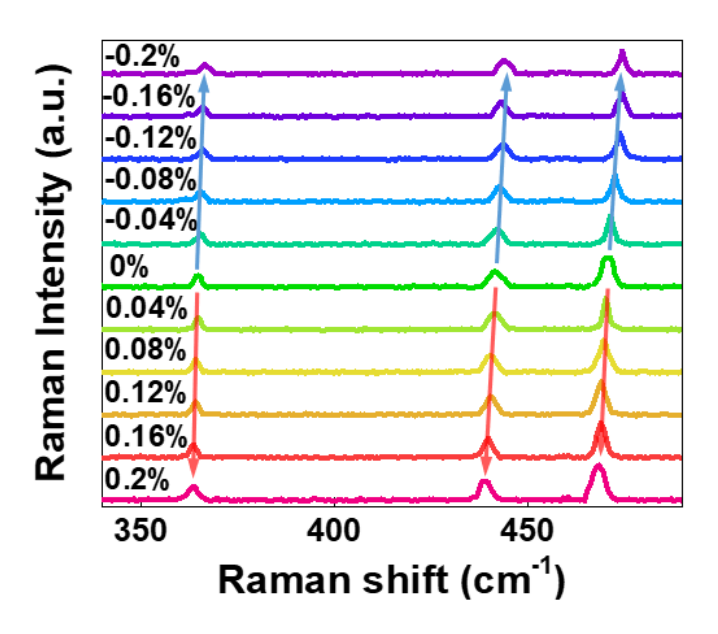


Figure 3.11 Raman spectra of the BP sample on a PMN-PT substrate subjected to various biaxial strains

Comparing these results with those from MoS_2 (approximately 1.06 under uniaxial strain)¹⁵⁹ and previously reported values for the A_g^2 Grüneisen parameter in BP (around 0.01 along the armchair direction)¹⁵⁷, it becomes evident that piezoelectric

substrate-induced biaxial strain offers a robust method for modifying and investigating lattice vibrations, as shown in Table 3-1.

Table 3-1 Grüneisen parameter of different materials under various strain inducing conditions.

| Material | Methods for | Grüneisen | Ref. |
|-----------------------------------|--------------------|-------------------------------------|-----------|
| | inducing strain | parameter | |
| Graphene | High pressure | 1.4 | 160 |
| Graphene | Flexible substrate | 1.9 | 161 |
| MoS ₂ | Flexible substrate | 1.06 | 159 |
| α-In ₂ Se ₃ | PMN-PT | 1.44 | 153 |
| BP | Flexible substrate | $0.01~({\rm A_g}^2)$ | 157 |
| BP | PMN-PT | 1.30 (A _g ²) | This work |

Figure 3.12 illustrates the BP structure with five key structural parameters: A_1 , A_2 , and A_3 denote distances between phosphorus atoms, while θ_1 and θ_2 represent angles between these atoms. The A_g^1 mode primarily involves out-of-plane atomic vibrations with minimal in-plane contribution and is orthogonal to the A_g^2 mode. In contrast, the B_{2g} mode is entirely in-plane and shows different dependencies on structural parameters. Alterations in A_1 , A_2 , and θ_1 have minimal impact on A_g^1 vibrations due to their predominant out-of-plane nature; however, changes in A_3 and θ_2 significantly influence A_g^1 shifts. The applied strain enhances or diminishes θ_2 shear-like motion between adjacent sublayers. Although this increases the restoring force between the sublayers in-plane, it decreases the force out-of-plane, resulting in a softening of the A_g^1 mode while strengthening the A_g^2 mode. When tensile strain stretches A_1 and

enlarges θ_1 , it extends atom separation along the y-axis, thereby reducing restoring forces along both x- and y-axes—contributing to significant redshifts observed in both B_{2g} and A_g^2 modes. The interlayer interaction strength is reflected by A_3 ; however, its low intensity indicates that interlayer restoring forces are negligible compared to those within layers (in-plane and out-of-plane). Thus, modifications to A_3 can be effectively disregarded in this context.

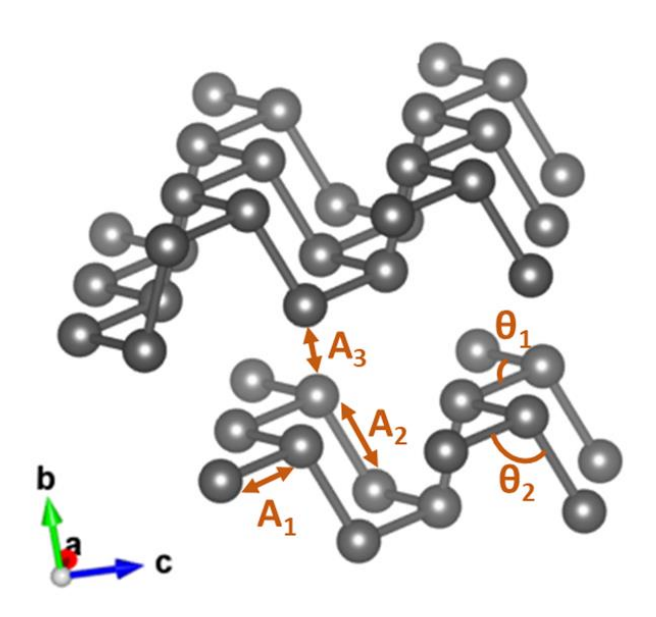


Figure 3.12 The 3D representation of BP structures includes specific definitions for various structural parameters.

The Raman spectra for BP under various strain conditions are presented in Figure 3.13. The intensities of the three Raman peaks show an increase under tensile strain and a decrease under compressive strain. This section concentrates on the in-plane B_{2g} and A_g^2 Raman peaks, as the anisotropic optical properties of few-layer BP under biaxial strain are more responsive than those seen in the interlayer structure. The observed intensity variations in Raman spectra under strain could arise from three interrelated

mechanisms. First, strain-induced lattice structure modifications alter the lattice constants and symmetry of material, which directly affect phonon vibration modes and their Raman activity by changing the scattering cross-section. Second, the Raman tensor—which governs the polarization-dependent coupling efficiency between incident and scattered light—becomes modified under strain, leading to measurable intensity changes even for identical vibrational modes. Furthermore, in anisotropic materials like BP, strain modulates optical anisotropy by perturbing the electronic structure and directional optical response of the crystal, thereby enhancing polarization-dependent intensity variations that correlate with the strain axis. These mechanisms collectively demonstrate how strain engineering provides a powerful tool for probing fundamental material properties through Raman spectroscopy.

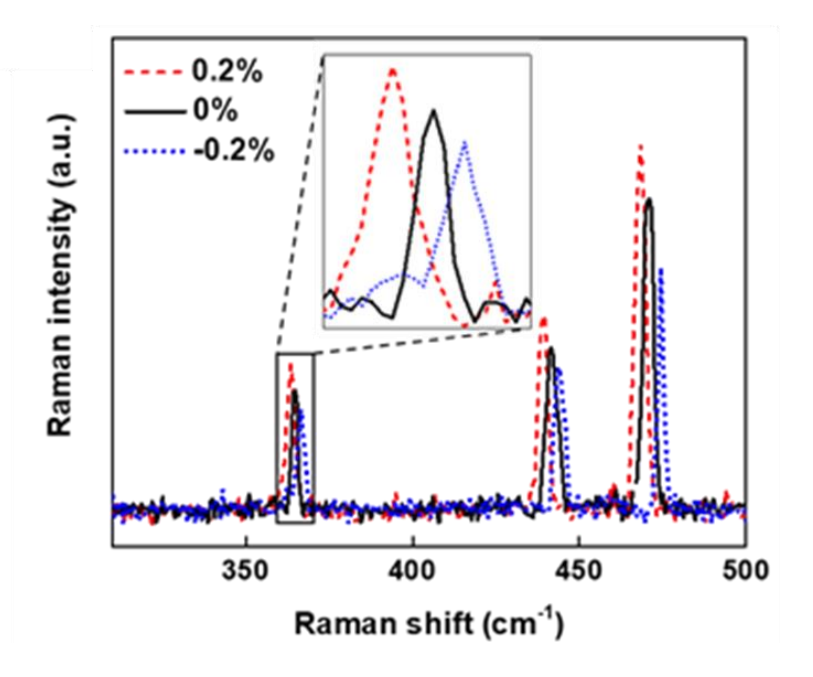


Figure 3.13 Polarized Raman spectra of the BP nanoflake under conditions of no strain, 0.2% tensile strain, and -0.2% compressive strain. Inset: A magnified view of the region surrounding the $A_{\rm g}^{-1}$ peak.

Figures 3.14 and 3.15 illustrate polar plots of the polarized Raman intensities for the B_{2g} and A_g^2 peaks under different strain levels. Notably, the Raman peak intensities for the A_g^1 and A_g^2 modes remain out of phase with the B_{2g} mode, consistent with results shown in Figures 3.6 and 3.7. Following the application of a tensile strain of 0.2% and a compressive strain of -0.2%, the intensity of the B_{2g} mode increased by approximately 35% at 90° but decreased by 14% under compressive strain at the same angle; however, it remained nearly unchanged at 0°.

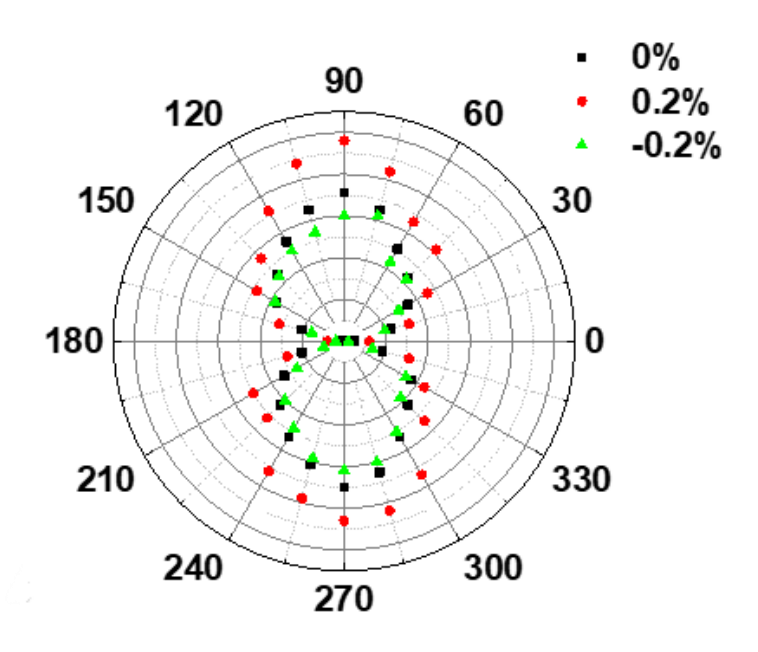


Figure 3.14 Polar plot illustrates the polarized Raman peak intensities for the B_{2g} mode under various biaxial strain conditions.

In contrast, the Raman intensities of the A_g^2 peaks rose by about 29% and fell by 12% at 0° , with minimal variation at 90° . The BP crystal shows comparable deformation behavior in both the armchair and zigzag orientations. It can be inferred that the A_g^2 and B_{2g} modes exhibit stronger electron-phonon interactions under tensile strain, while these interactions weaken under compressive strain, particularly when subjected to polarized light at angles of 0° and 90° , respectively. This analysis highlights the

sensitivity of BP vibrational modes to applied strain, emphasizing their potential applications in flexible electronics and optoelectronic devices.

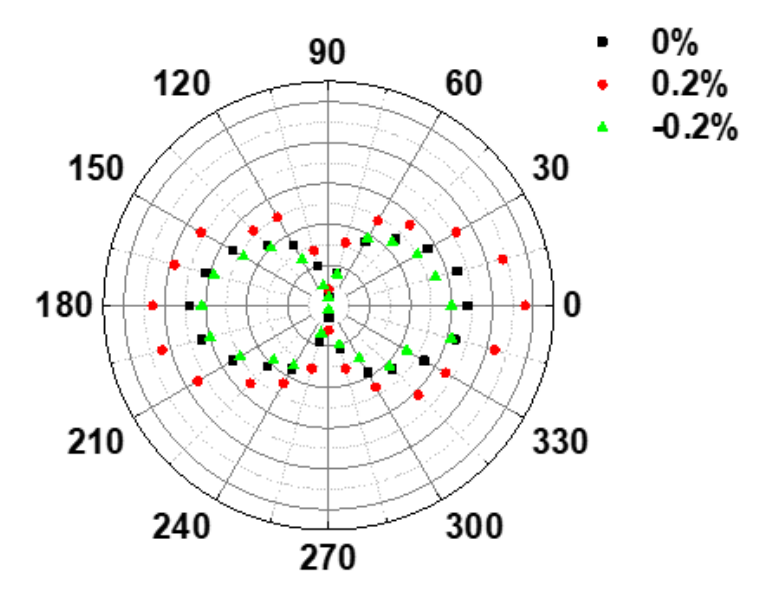


Figure 3.15 Polar plot illustrates the polarized Raman peak intensities for the ${\rm A_g}^2$ mode under various biaxial strain conditions.

3.6 Conclusion

In summary, we have shown that the features of polarized Raman spectra of BP can be effectively adjusted by applying biaxial strain generated by a piezoelectric PMN-PT substrate. By carefully adjusting the bias voltage on the substrate, we can effectively generate and apply biaxial strain to BP samples, resulting in significant shifts in the Raman spectra. To explore the vibrational behavior of ultrathin BP under various strain conditions, we calculated the Grüneisen parameter. The strain response observed in BP is probably attributed to changes in bond lengths and angles caused by the applied biaxial strain. Our analysis of the polarized Raman spectroscopy results indicates that electron-phonon interactions can be adjusted via this strain.



This research provides an effective approach for examining how the piezoelectric PMN-PT substrate influences the electrical and optical properties of BP materials. Moreover, our results could be applied to investigate additional strain-dependent phenomena and a range of applications in photonics, strain sensing, and energy harvesting.



Chapter 4 Preparation of centimetre-scale BP-based devices on silicon substrates

4.1 Introduction

Two-dimensional (2D) black phosphorus (BP) exhibits remarkable carrier mobility and the capacity to support high current densities, making it an excellent candidate for advanced functional devices. ^{163–166} The bandgap of BP is tunable, ranging from 0.3 eV in its bulk form to approximately 2 eV in monolayers, positioning it within the energy range of conventional semiconductors used in transistor applications. Additionally, its anisotropic electrical properties make BP a promising material in the field of nanophotonics. 156,167 These outstanding characteristics present potential solutions to various development challenges and facilitate the integration of 2D materials into the information technology sector.⁵⁷ Earlier research mainly concentrated on mechanically exfoliated BP-based back-gate FETs on silicon substrates, where the channel width and device dimensions were naturally limited by the micrometer size of the nanoflakes. This limitation significantly hindered the transition to practical electronic circuits and systems. To address this issue, Chen et al. described the synthesis of single-crystal BP films with sub-centimeter dimensions and a thickness of approximately 290 nm on SiO₂/Si substrates, showcasing remarkable device performance. 168 Our research group has also successfully fabricated ultrathin centimeter-scale BP on mica substrates using PLD.87 However, the predominant use of mica substrates is not typical in the current silicon-centric semiconductor industry, highlighting the necessity for an effective transfer process that integrates our BP thin



films with complementary metal-oxide-semiconductor (CMOS)-compatible substrates while their high crystallinity and properties can be preserved.

Among the various transfer techniques available, the wet transfer method is frequently utilized for transferring as-grown 2D materials, typically using poly(methyl methacrylate) (PMMA) or Polystyrene (PS) as adhesive layers. 114,169 Nonetheless, this approach requires immersing samples in aqueous solutions, which is not suitable for the sensitive nature of BP and may result in degradation or reduced crystal quality. 170,171 Additionally, removing large-scale BP thin films from mica substrates can easily cause cracks or wrinkles because of their fragility, negatively impacting carrier mobility and overall device performance. 172,173 Consequently, there is an immediate need for focused research to create effective methods for transferring large-scale BP thin films while preserving their beneficial properties. To tackle the issues related to wet transfer processes, it is crucial to investigate alternative supporting materials for transfer, choose suitable solvents, and enable the delamination of BP films from mica substrates onto silicon substrates.

In this section, we present a clean transfer strategy aimed at producing centimeter-scale, high-quality few-layer BP films that have been grown on silicon substrates using precisely controlled pulsed laser deposition (PLD). Ethylene-vinyl acetate (EVA) polymer and ethylene glycol (EG) have been chosen as the adhesive layer and medium to maintain the excellent crystalline quality and properties of BP during the transfer process. Significantly, we have successfully created large-scale bottom-gate few-layer BP FET arrays on SiO₂/Si substrates that demonstrate exceptional uniformity. These FET device arrays exhibit outstanding electrical properties, such as high carrier mobility and substantial current switching ratios that are comparable to those of as-

grown BP films on mica substrates. This study reveals that the wet transfer method can successfully produce scalable, high-crystallinity BP-based arrays while maintaining significant electrical performance and allowing for more intricate device design options across various applications.

4.2 Growth conditions for BP via PLD

The BP crystal source from SMART-ELEMENTS and the mica substrate were positioned in respective holders approximately 36 mm apart within the chamber. The growth was conducted at an ultra-high vacuum pressure of around 1.6×10^{-9} Torr, with the mica substrate maintained at a temperature of 300 °C. A 248 nm KrF excimer pulsed laser, functioning at a repetition frequency of 5 Hz and a laser intensity of 1.2 J/cm², was utilized to create a plasma plume that contained large BP clusters. The ablated clusters in the physical vapor were then transported to the mica surface, where a few-layer BP thin film was deposited at a regulated substrate temperature.

4.3 Fabrication process for FETs

After the growth of the BP thin film, a solution of EVA was prepared, consisting of 40 wt% vinyl acetate and 10 wt% dissolved in xylene. This solution was then spin-coated onto the sample at a speed of 1500 rpm for 1 minute. Following this, the coated sample was placed in an oven at 80 °C for 1 hour to cure the EVA layer. Subsequently, the EVA/BP film was soaked in EG solvent at 50 °C for half hour, which aided in detaching the EVA/BP film from the growth substrate. The detached film was then carefully transferred onto the target substrate. To guarantee adequate adhesion, the transferred composite was put in a vacuum drying oven and heated at 50 °C for half hour.

Following this step, the sample was immersed in tetrahydrofuran (THF) for 30 minutes to selectively eliminate the EVA film.

For device preparation, standard photolithography using a Suss MA6 Aligner and electron-beam evaporation techniques were employed to pre-deposit a strip electrode array consisting of 10 nm titanium (Ti) and 50 nm gold (Au) on a SiO₂/Si substrate. The BP thin film, created through PLD, was subsequently wet-transferred onto the SiO₂/Si substrate with Ti/Au electrodes, ensuring direct contact between the Au electrodes and the BP thin film for the assembly of FET arrays.

4.4 Characterization of BP and FET arrays

The Raman spectra was examined using a high-resolution confocal μ -Raman microscope (Horiba HR 800), which employed a 488 nm excitation laser source and featured a spot size of 1 μ m. To prevent damage to the nanoflakes, the laser power was maintained at a minimal level of approximately 1 μ W. The thickness and surface topography of the BP films were evaluated using a commercial atomic force microscope (Asylum Research MFP-3D) functioning in tapping mode. X-ray diffraction analysis of the as-deposited thin films was conducted using a Rigaku SmartLab 9 kW system, employing Cu K α radiation (λ = 1.5406 Å).

For device characterization, a Keithley 4200 Semiconductor Parameter Analyzer was used, paired with a probe station (Lake Shore Model CRX-6.5K) that included a microscope, vacuum chamber, and a micromanipulator featuring precision tips measuring in the micrometer range. This combination of advanced characterization techniques allowed for a comprehensive evaluation of the structural and electronic properties of BP thin films.



4.5 Clean transfer process of BP

Figure 4.1illustrates the transfer process for BP thin films. The BP film was first developed on a mica substrate using the earlier established PLD technique. A polymer solution was first spin-coated onto the BP film to facilitate the wet transfer. Given the sensitivity of BP layers to degradation from exposure to oxygen and moisture, EG was chosen as the wet medium. 174 Notably, before the entire assembly was immersed in the EG solution at 50°C for 1 hour, one edge of the polymer/BP film was intentionally scratched to allow easier penetration of the EG solution between the mica substrate and the as-grown BP film. After this, the polymer/BP film was gently peeled off from the mica substrate and placed onto the target substrate. To enhance adhesion, any remaining EG solution at the interface between the BP film and the target substrate was removed by evaporation in a vacuum drying oven at 50 °C for half hour. Ultimately, THF was employed to eliminate the polymer layer.

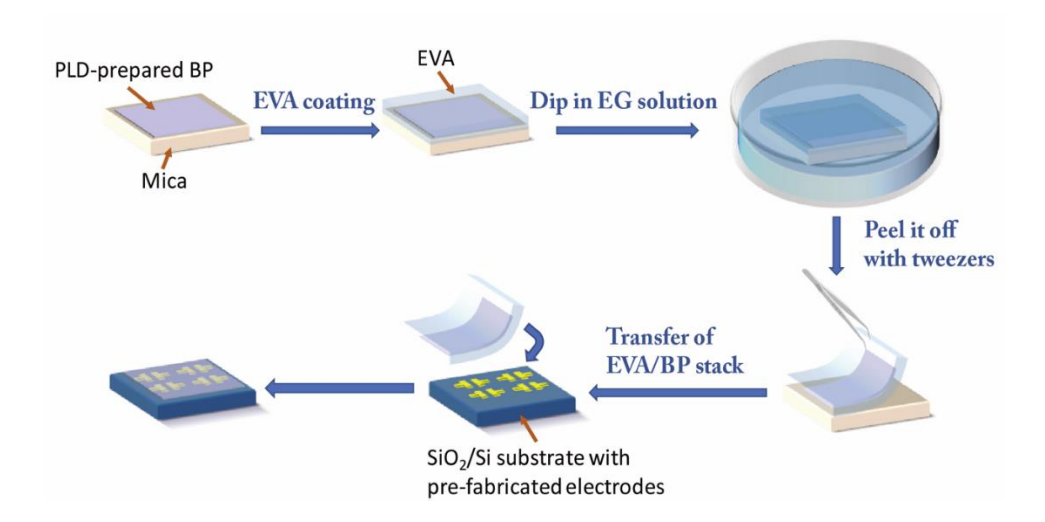


Figure 4.1 Schematic diagram of wet transfer process of PLD-deposited BP thin film with EVA polymer assisted in EG solution.

4.6 Adhesion analysis of different interfaces

Figures 4.2 present photographic and optical microscopic images of the BP thin film following its wet transfer onto a SiO₂/Si substrate via the EVA-assisted method. The complete separation of the BP film from the mica substrate is evident, with the transferred large-area BP thin films appearing clean, continuous, and uniform, exhibiting no noticeable cracks or wrinkles. This indicates a successful transfer from mica to SiO₂/Si substrate.

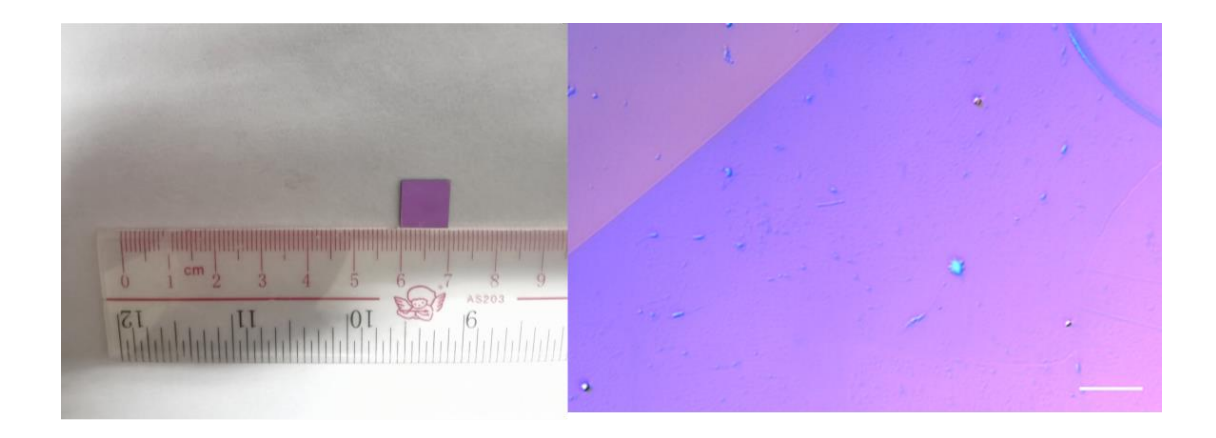


Figure 4.2 Left: Optical photo and Right: Microscopic images of wet-transferred BP on SiO₂/Si substrate (scale bar:10 μm).

In contrast, when PS was employed as the support layer for transferring BP film, as shown in Figure 4.3, only minimal transfer from the mica substrate was achieved.

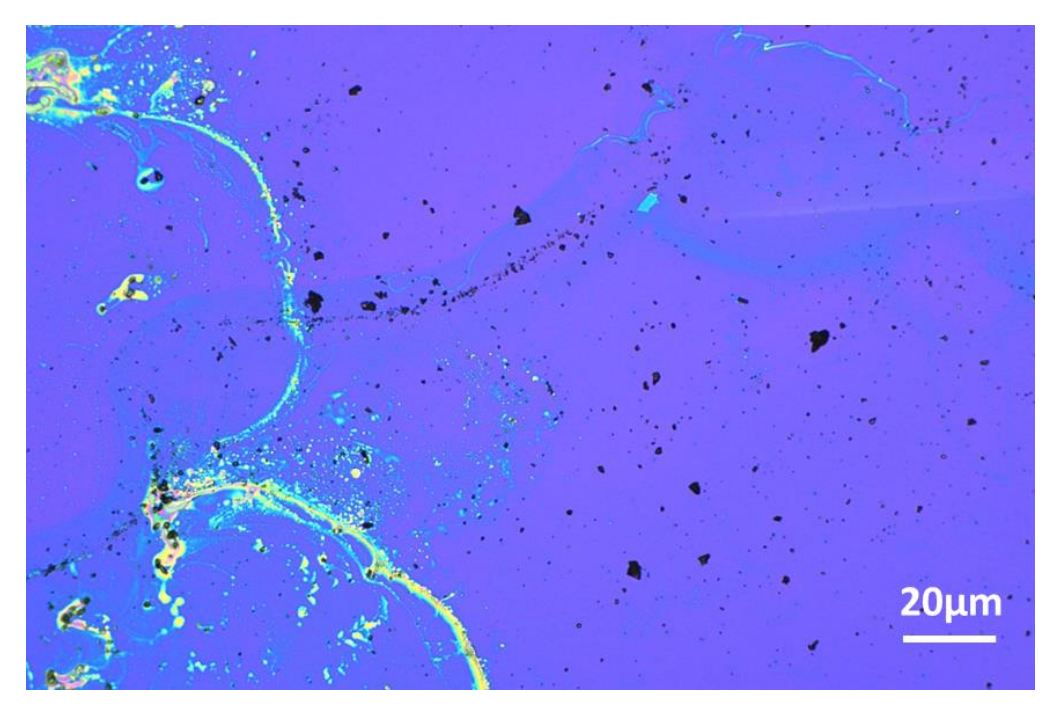


Figure 4.3 Microscopic image of wet-transferred BP sample on the SiO₂/Si substrate using PS polymer in EG solvent.

A critical element in the successful transfer of large-area BP films from mica substrates is managing adhesion at the interface between the polymer and the thin film. This adhesion management is crucial as it directly impacts the integrity, quality, and functionality of the transferred BP film. Proper adhesion control serves multiple essential purposes: ensuring clean detachment of the BP film from the mica substrate; preventing film damage or fragmentation during the transfer process and maintaining desirable properties of BP while shielding it from environmental degradation.¹⁷⁵

The key to successful transfer lies in achieving a delicate balance of forces, where the adhesion between the polymer and BP must be greater than that between BP and mica. This differential adhesion is critical for several reasons. It allows the BP film to be lifted cleanly from the mica substrate without leaving residues or fragments behind. Additionally, it provides the necessary mechanical support to maintain the structural

integrity of the BP film during the transfer process. Furthermore, it helps overcome the van der Waals forces that bind the BP to the mica, facilitating a complete and uniform transfer.

The thermodynamic work of adhesion offers a qualitative assessment of adhesion between different interfaces, calculated using the formula:

$$W_{AB} = \gamma_A + \gamma_B - \gamma_{AB} \tag{4.1}$$

where γ_A and γ_B correspond to the surface energies of phases A and B, respectively, while γ_{AB} denotes the interfacial energy between these phases. According to Owen-Wendt, Young's, and Fowkes' equations¹⁷⁶, this can be further expressed as:

$$W_{AB} = 2(\gamma_A^d \gamma_B^d)^{1/2} + 2(\gamma_A^p \gamma_B^p)^{1/2}$$
 4.2

where γ^d and γ^p indicate dispersion and polar components, respectively. To investigate the adhesion between different surfaces, we assessed the contact angles of EG and glycerol on various surfaces, as shown in Figure 4.4.

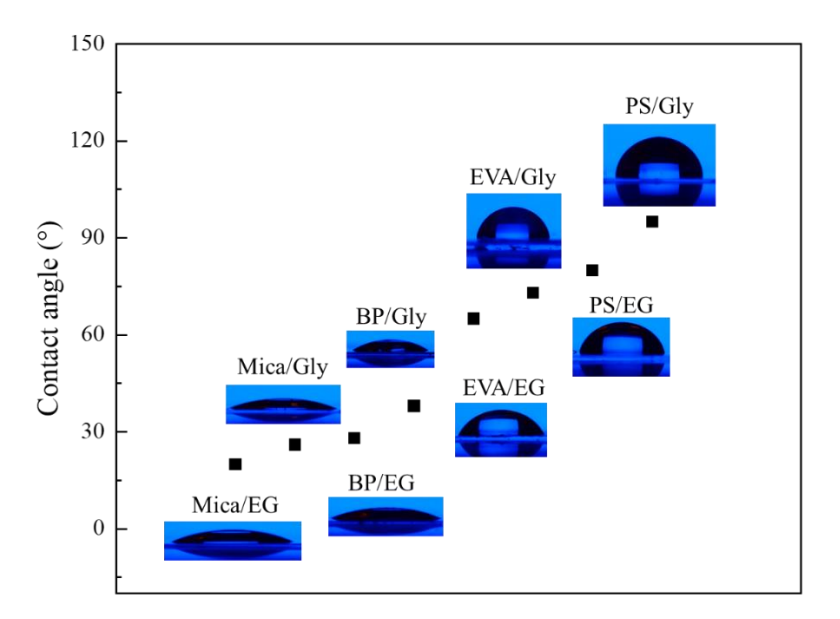


Figure 4.4 Contact angle measurements of EG and glycerol (Gly) on different surfaces.

Based on the measurements, we compiled the adhesion results between various surfaces in Figure 4.5. Our findings reveal that adhesion between EVA and BP is stronger than that between BP and mica, suggesting that EVA can effectively detach the BP film from its mica substrate. In contrast, the adhesion between PS and BP is less robust than that between BP and mica, suggesting that the BP film is more likely to stay attached to the mica substrate.

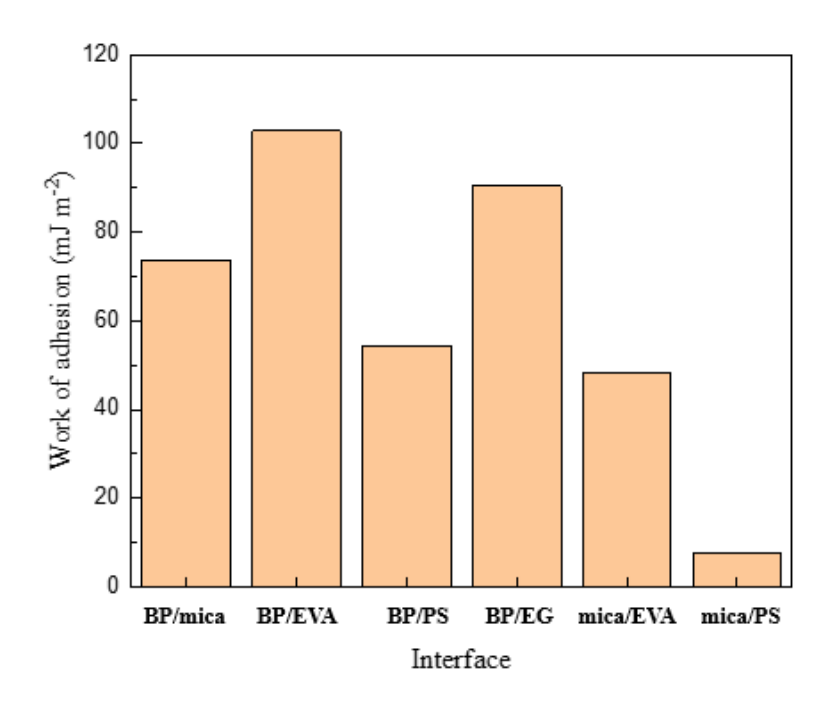


Figure 4.5 Work of adhesion at various interfaces.

Moreover, as shown in Figure 4.6, EVA is a copolymer containing polar functional groups such as carbonyl and hydroxyl groups, which promote strong dipole interactions with BP film, thereby enhancing adhesion. Its rubber-like elasticity also allows EVA to closely conform to the atomic-scale terraces of the mica substrate beneath the BP, increasing the effective contact area and further strengthening the adhesion. In contrast, PS is a rigid, glassy polymer that lacks polar functional groups, resulting in weak intermolecular interactions with the BP film. Moreover, rigidity of

PS limits its ability to conform to the uneven mica surface, leading to poorer contact and consequently weaker adhesion compared to EVA.

Figure 4.6 Molecular formula of (a) EVA and (b) PS

We evaluated the transfer efficiency of BP from a mica substrate using two distinct solvents: isopropyl alcohol (IPA) and EG. These solvents were chosen for their unique properties that might make them suitable for the transfer process of 2D BP. IPA, widely used in electronics manufacturing, offers several advantageous characteristics. Its low boiling point of 82.6°C allows for rapid evaporation post-transfer. Additionally, the miscibility of IPA with water and polar nature promotes effective interaction with many 2D materials, potentially facilitating the transfer process. ¹⁷⁸ In contrast, EG presents a different set of beneficial properties. With a higher boiling point of 197.3°C and increased viscosity compared to IPA, EG provides an extended window for manipulation during the transfer process. This characteristic may contribute to maintaining the structural integrity of the 2D material throughout the transfer. ¹⁷⁹ Both solvents serve the primary purpose of reducing adhesion forces between the 2D material and its substrate, a crucial factor in successful transfers. However, their distinct properties lead to varying outcomes in the transfer process. Figure 4.7 illustrates a schematic representation of the peeling processes in these two solvents, highlighting the differences in their mechanisms.

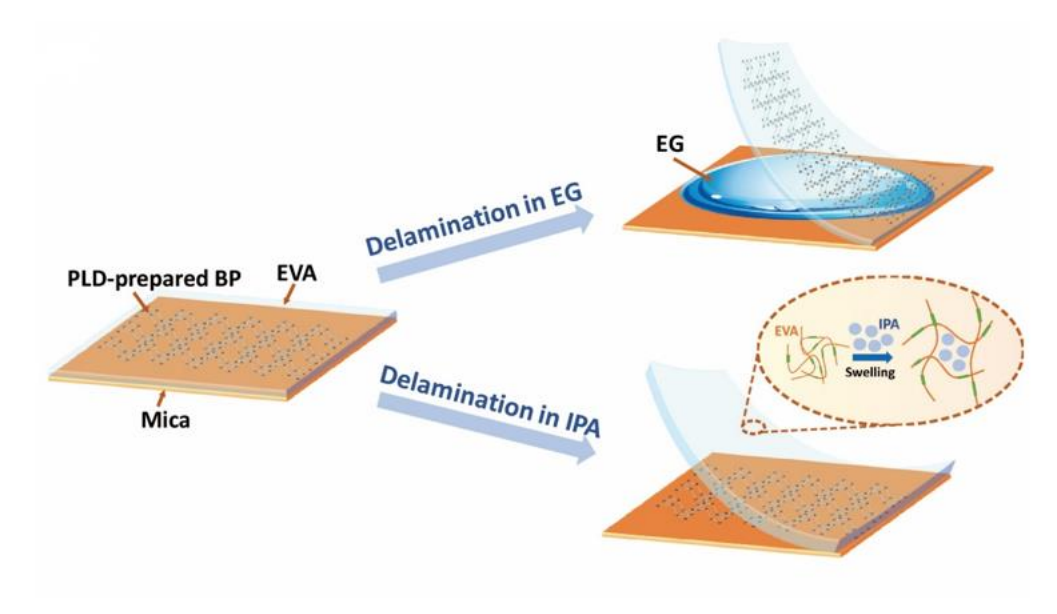


Figure 4.7 Schematic representation of the delamination process in EG and IPA solutions during peeling.

Our study found that immersing EVA in IPA solution can led to considerable swelling of the polymer, increasing its thickness by about 50% compared to its original size. This effect can be explained by the strong interaction between IPA and EVA, largely due to the higher polarity of IPA. When EVA is immersed in IPA, the solvent's polar properties enable IPA molecules to infiltrate the polymer matrix. This infiltration disrupts intermolecular forces and diminishes the interactions between EVA chains, causing the polymer network to expand or swell. This swelling makes the adhesive bond more vulnerable to disruption or failure, resulting in limited transfer of the BP film from the mica substrate, as illustrated in Figure 4.8.

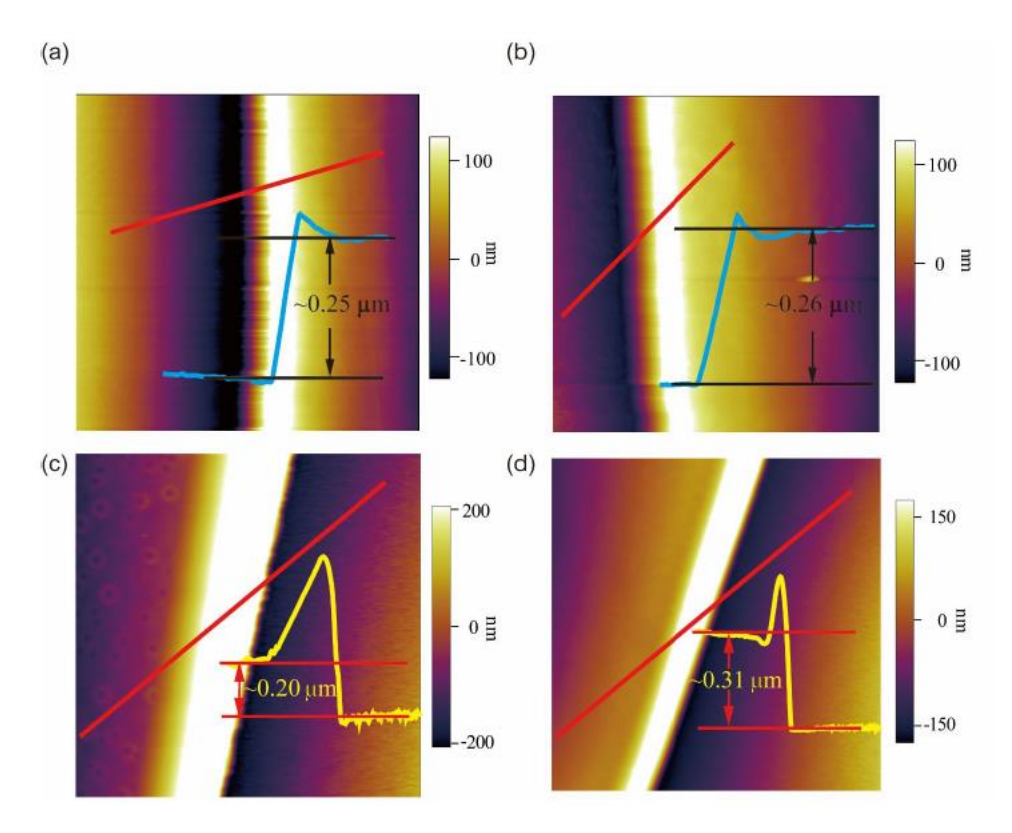


Figure 4.8 AFM topography and height analysis of the EVA polymer is presented in (a) before and (b) after immersion in EG solvent. A comparable analysis of the EVA polymer is shown in (c) before and (d) after immersion in IPA solvent.

In contrast, when EVA was immersed in the non-polar EG solvent, its thickness remained almost unchanged, and no penetration occurred. Consequently, EVA and EG were selected as the adhesive layer and transfer solvent, respectively, to enhance the transfer of the BP film (see Figure 4.9). As the EVA/BP film is slowly peeled away, the EG solvent continues to infiltrate the gap, ultimately facilitating the complete separation of the EVA/BP film from the mica substrate.

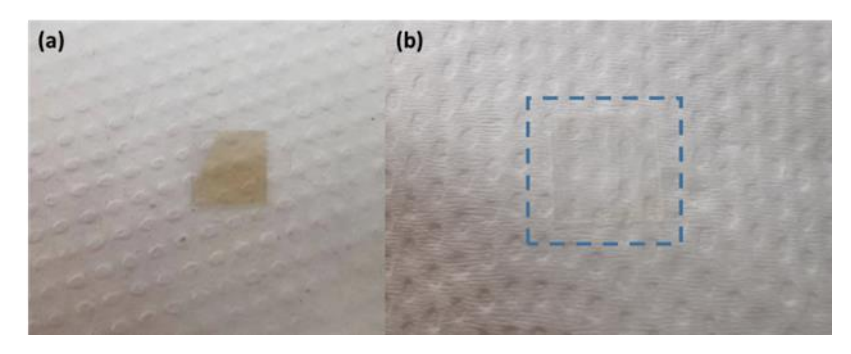


Figure 4.9 Optical image of BP sample on mica substrates (a) after direct growth, (b) after wet transfer with EVA polymer in EG solvent

4.7 Material characterization of BP thin films

To deduce the thickness and roughness of the few-layer BP sheet, AFM measurements were conducted both before and after the wet transfer process. As illustrated in Figure 4.10, the thickness and roughness of the as-grown BP on a mica substrate were about 5.2 nm and 46.46 pm, respectively.

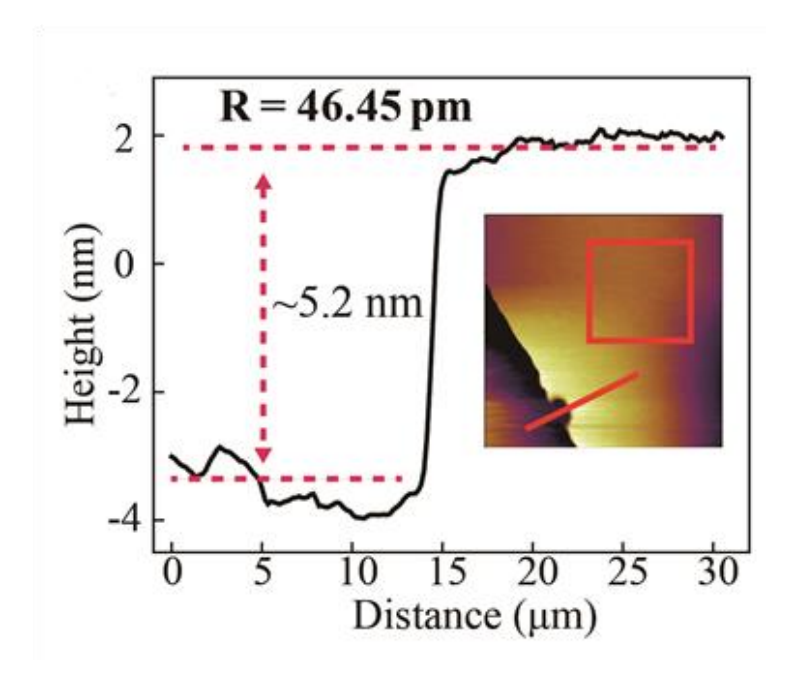


Figure 4.10 The AFM height profile of direct-grown BP thin films on a mica substrate.

Figure 4.11 indicates that following the wet transfer, the thickness of the BP thin film remained almost the same. The slight increase in both thickness and roughness of the BP thin film after wet transfer can be attributed to several interrelated factors. During the transfer process, microscopic residues of the transfer polymer (EVA) may remain on the BP surface, contributing to both increased thickness and roughness. Additionally, impurities from the solution or the environment can become trapped between the BP film and the new substrate or on the BP surface, leading to local variations in thickness and increased surface roughness. The mechanical manipulation involved in the transfer can also induce strain or create wrinkles in the film, manifesting as increased roughness and slight variations in thickness. Furthermore, the interaction between the BP film and the new substrate may differ from its interaction with the original growth substrate, potentially leading to slight changes in film morphology and thickness. Water molecules trapped between the BP film and the new substrate during transfer can contribute to increased thickness and surface irregularities as well.

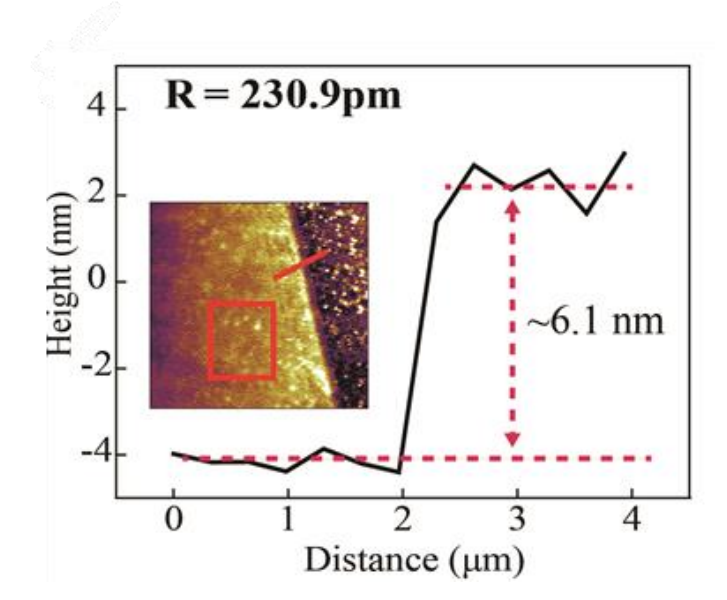


Figure 4.11 The AFM height profile of wet-transferred BP thin films onto a SiO₂/Si substrate.

Table 4-1 clearly shows that all 2D materials experience an increase in surface roughness after transfer, primarily due to polymer residues, wrinkles, and strain introduced during the process. For instance, graphene, MoS₂, and WS₂ transferred onto various substrates via polymer-assisted wet methods all exhibit roughness increases reaching several nanometers. In our study, BP transferred from mica demonstrates a roughness increase from approximately 0.046 nm to 0.23 nm.

Although this represents an increase, the final roughness remains significantly lower than the values reported for other 2D materials after transfer, indicating a relatively cleaner and smoother surface in our process.

Table 4-1 Comparison of surface roughness of 2D materials before and after transfer

| 2D Material | Substrate | Roughness | Roughness | Method | Ref. |
|------------------|-------------|------------|-----------|--------------------|-------|
| | | Before | After | | |
| | | Transfer | Transfer | | |
| | | (RMS, nm) | (RMS, nm) | | |
| Graphene | Copper foil | ~0.3 – 0.5 | ~1 – 5 | PMMA-assisted | [180] |
| | | | | wet transfer; | |
| | | | | polymer residues | |
| | | | | and wrinkles | |
| | | | | increase roughness | |
| MoS ₂ | Sapphire | ~0.2 – 0.4 | ~2 - 8 | Polymer-assisted | [181] |
| | | | | wet transfer; | |
| | | | | wrinkles and | |
| | | | | polymer residues | |
| | | | | contribute | |

| WS ₂ | Sapphire | ~0.3 | ~3 – 7 | Similar to MoS ₂ ; | [182] |
|-----------------|----------|--------|--------|-------------------------------|-------|
| | | | | capillary or | |
| | | | | bubbling transfer | |
| | | | | methods | |
| BP | Mica | ~0.046 | ~0.23 | Wet transfer with | This |
| | | | | EVA polymers; | work |
| | | | | roughness | |
| | | | | increases due to | |
| | | | | polymer residues | |
| | | | | and transfer- | |
| | | | | induced strain | |

Figure 4.12 displays the XRD patterns for the bare mica substrate, as-grown BP on mica, and wet-transferred BP on a SiO₂/Si substrate. The distinct diffraction peaks identified for both the mica substrate and the wet-transferred BP correspond to the monoclinic structure of mica and the orthorhombic structure of BP, respectively, offering direct evidence of the high crystallinity of the BP thin films produced by PLD. It is important to note that the intensity of the XRD peaks for the original as-grown BP is relatively weak compared to that of mica, making it challenging to identify BP peaks due to their proximity to those of mica. This issue is addressed after transferring BP onto the SiO₂/Si substrate, where the BP peaks appear clear and distinct in the XRD spectrum, enabling a more precise characterization of the BP thin film.

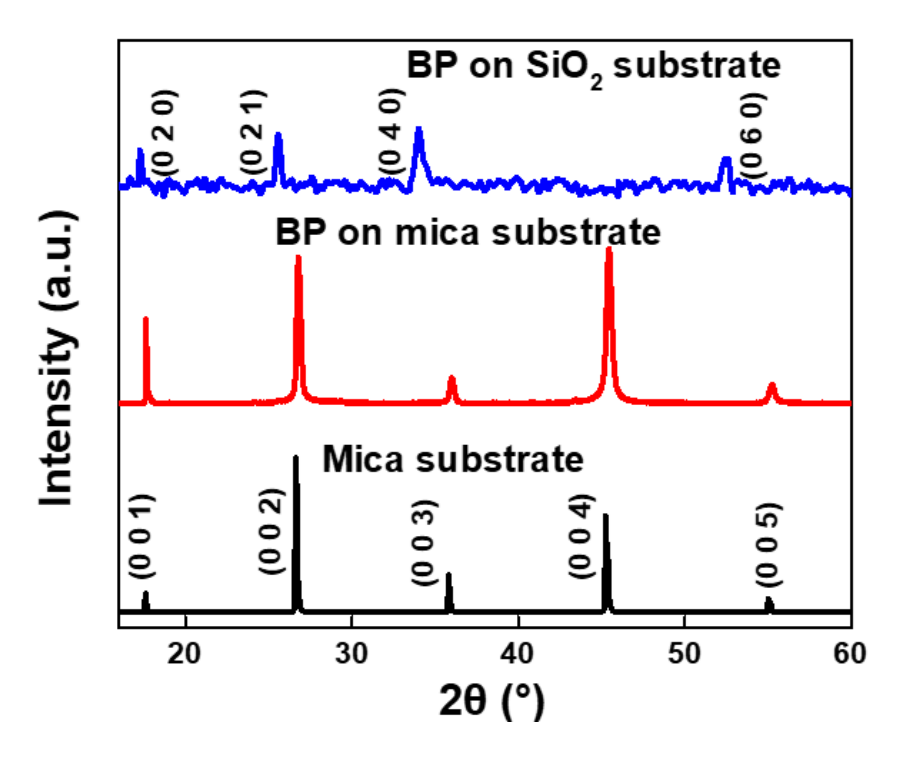


Figure 4.12 XRD patterns for the bare mica substrate, as-grown BP, and wettransferred BP.

Additionally, Raman spectroscopy was employed to characterize the BP thin films before and after wet transfer, as shown in Figure 4.13. Based on previous studies, three characteristic Raman peaks were identified at 365 cm $^{-1}$ (out-of-plane mode, A_g^{-1}), 442 cm $^{-1}$ (in-plane mode along zig-zag direction, B_{2g}), and 471 cm $^{-1}$ (in-plane mode along armchair direction, A_g^{-2}). The positions and intensities of these three peaks remained unchanged after the wet transfer process, suggesting that the quality of the sample has been maintained. These results indicate that the wet transfer technique employed successfully preserves both the integrity and structural properties of PLD-grown BP thin films.

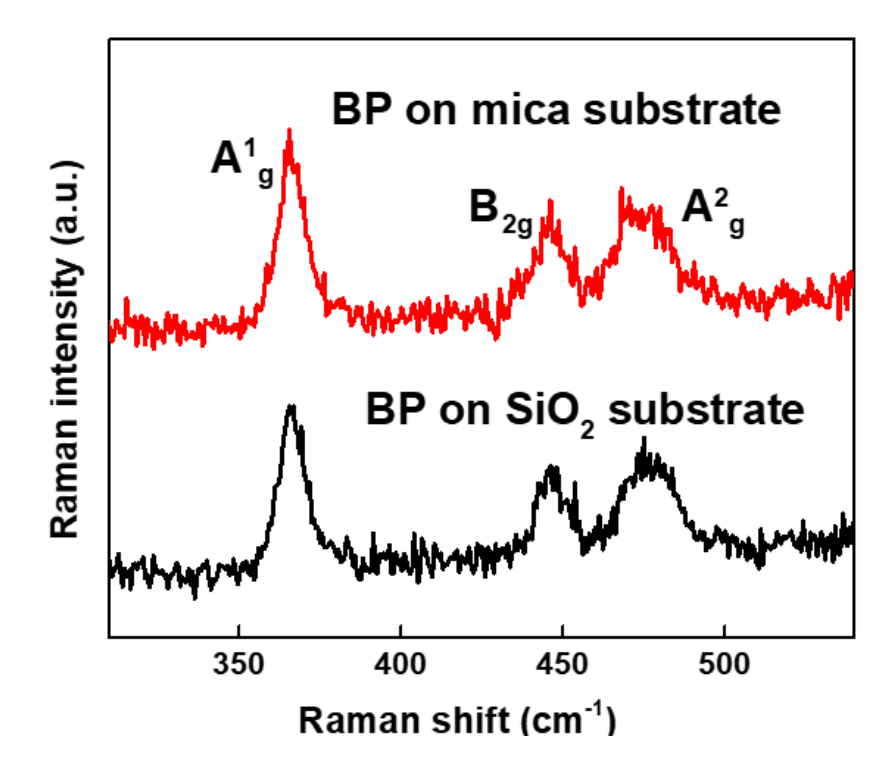


Figure 4.13 Raman spectra of BP thin films before the wet transfer process (on mica substrate) and after the transfer to SiO₂/Si substrate.

4.8 Electrical properties of BP-based FETs

To evaluate the homogeneity and electrical performance of the transferred BP thin film, we created an array of stripe Ti/Au electrodes with different channel lengths. As shown in Figure 4.14, the lengths of the four channels, highlighted in red, orange, blue, and green, are 70 µm, 270 µm, 420 µm, and 570 µm, respectively. The fabrication of FETs with varying channel lengths is crucial as it allow for direct measurement of key electrical parameters such as carrier mobility, on/off ratio, and threshold voltage, which are essential for evaluating the quality and potential applications of the BP thin film. By creating devices with a range of channel lengths, we can assess how the properties of BP thin films scale with size, demonstrating its potential for large-area applications. Comparing the performance of FETs across different channel lengths

provides insight into the uniformity of the BP film over large areas, with consistent performance indicating high-quality film transfer and excellent material homogeneity. Through the fabrication and characterization of these FET arrays, we can comprehensively evaluate the electrical properties, uniformity, and scalability of the transferred BP thin film.

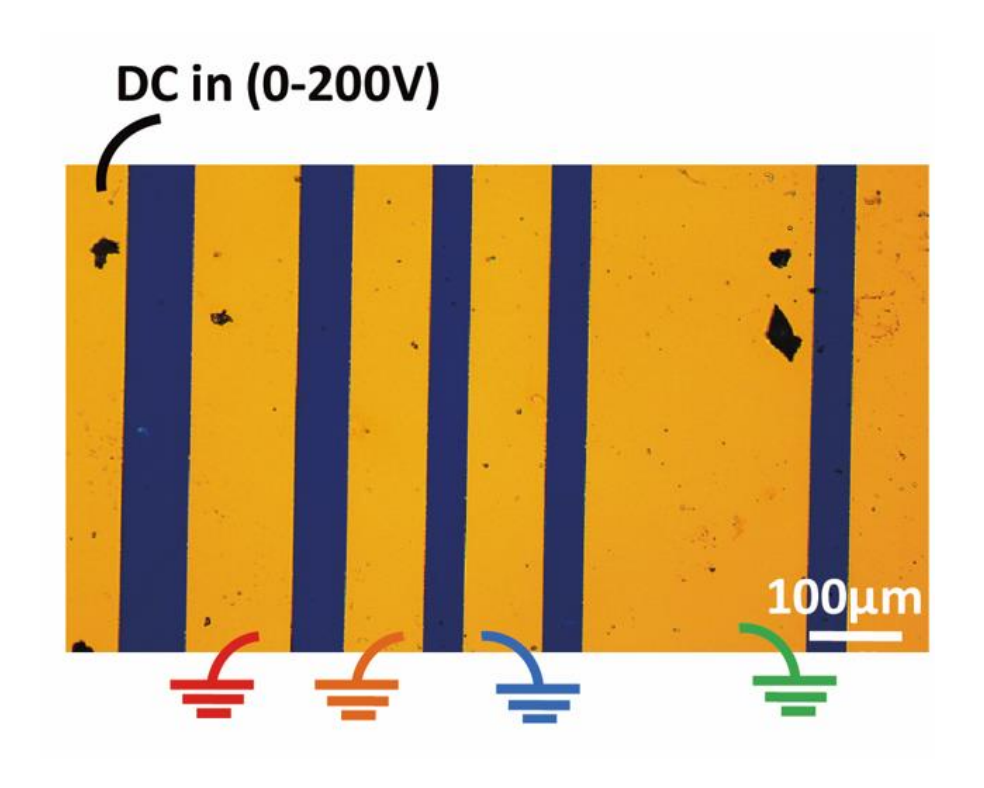


Figure 4.14 An optical microscope image of wet-transferred BP FET arrays with varying channel lengths on a SiO₂/Si substrate.

The drain current (I_{ds}) against drain voltage (V_{ds}) characteristics of the as-fabricated BP FETs with different channel lengths are summarized in Figure 4.15. Notably, the output current exhibits only a slight decrease as the channel length increases, indicating exceptional uniformity and continuity of the BP thin film across a large area. This modest reduction in output current with increasing channel length can be attributed to several interrelated factors. As the channel length grows, so does its resistance, requiring carriers to travel a greater distance. This extended path naturally

impedes current flow and increases the probability of carrier collisions with lattice vibrations (phonons) and impurities. These scattering events lead to reduced carrier mobility, thereby diminishing current flow. Additionally, for a given drain-to-source voltage, the electric field along the channel decreases as the length increases. This reduced field strength results in lower carrier velocities, further contributing to the slight current decrease. The observed minimal current reduction across different channel lengths underscores the high quality and consistency of the BP thin film.

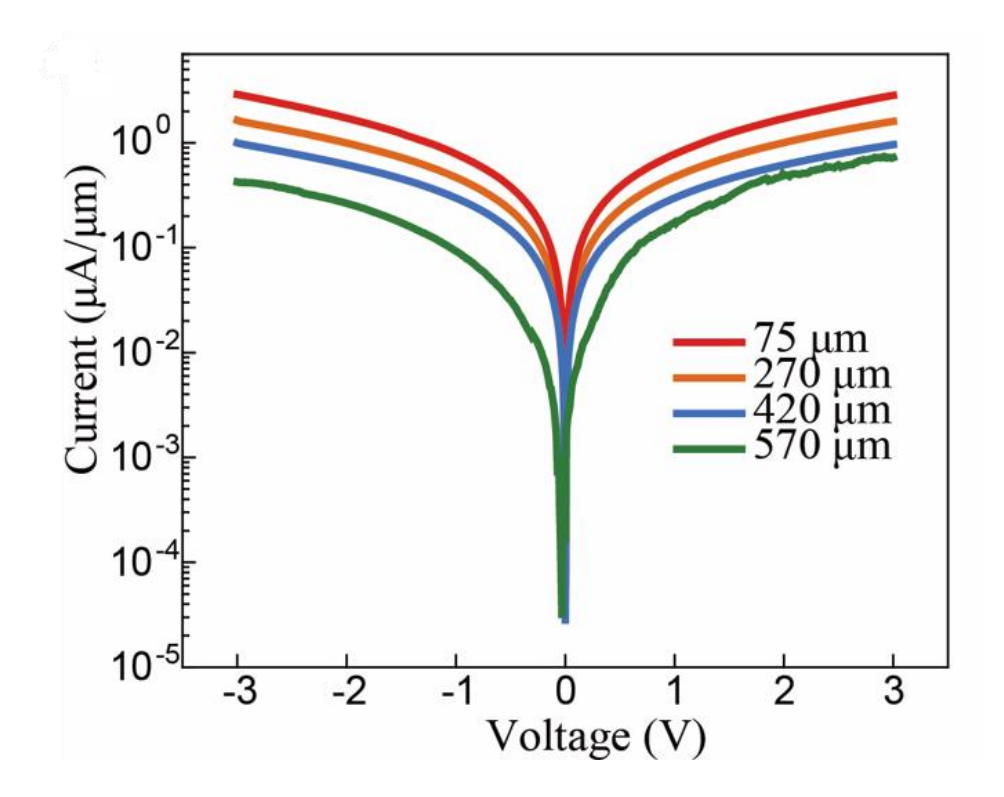


Figure 4.15 Drain current (I_{ds}) versus drain voltage (V_{ds}) curves for BP FETs with channel lengths of 75 μ m (red), 270 μ m (orange), 420 μ m (blue), and 570 μ m (green).

We also examined the I_{ds} - V_{ds} characteristics of BP FETs on SiO_2/Si substrates, both with and without an EVA polymer coating, after being exposed to ambient conditions overnight to assess the passivation effect of the polymer. The BP FETs with and without passivation were exposed to the same conditions for an equivalent duration. A

comparison of the results presented in Figure 4.16 demonstrates that using a polymer coating as a passivation strategy is highly effective in maintaining the performance of FETs fabricated with the wet-transferred BP. After 24 hours of exposure to ambient conditions, the output current of the unpassivated BP FET fell to only 0.01% under a -3 V bias, whereas the output current of the passivated BP FET decreased to about 75% of its initial value.

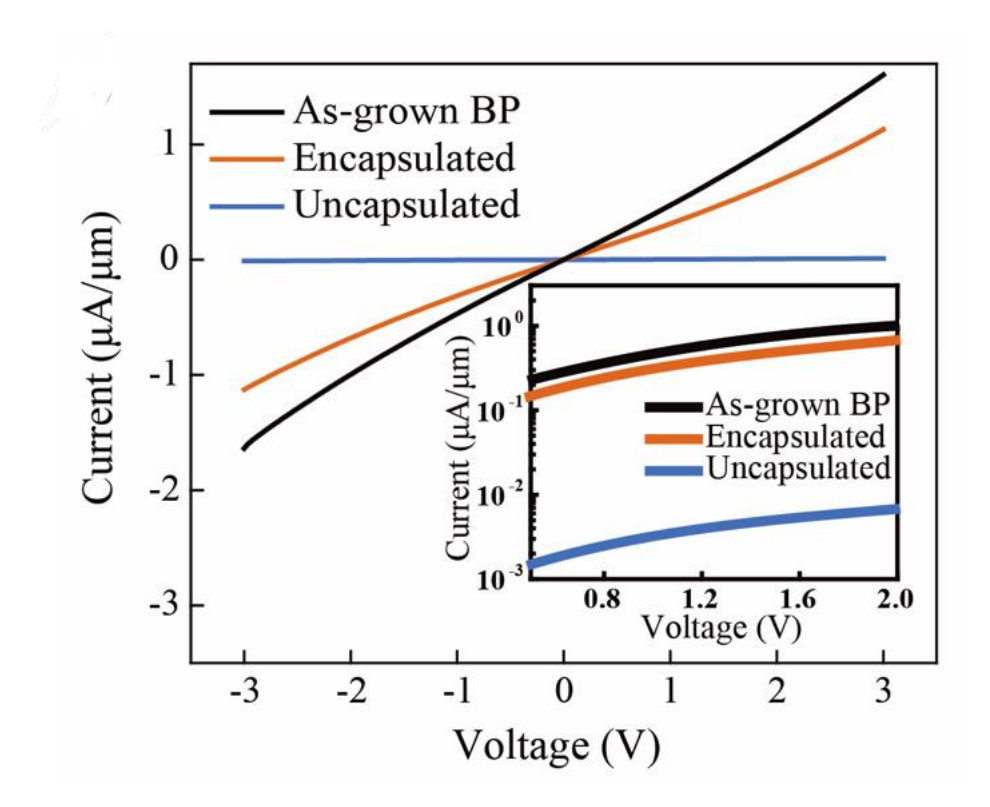


Figure 4.16 I_{ds} - V_{ds} curves under different passivation conditions, presented in both linear and logarithmic scales in the inset.

Figure 4.17 shows the output currents before and after removing the EVA polymer to assess the impact of immersing the device in THF solvent during the polymer removal process. When BP undergoes oxidation upon air exposure, its output current typically decreases exponentially. However, in our measurements before and after polymer removal, the output current remains within the same order of magnitude. Such

variations are common and expected between two BP devices fabricated using the same method. Therefore, we conclude that the device still maintains its efficiency despite the observed changes. The results demonstrate that this removal procedure has a negligible effect on device performance, highlighting the effectiveness of the chosen method. The successful removal of EVA polymer without significantly compromising BP device performance can be attributed to several key factors. THF exhibits selective solubility, effectively dissolving EVA while showing low reactivity with BP. This selectivity is crucial for preserving the integrity of the BP layer. Moreover, the brief exposure time during the process is carefully calibrated to be sufficient for EVA dissolution without risking damage to the underlying BP structure.

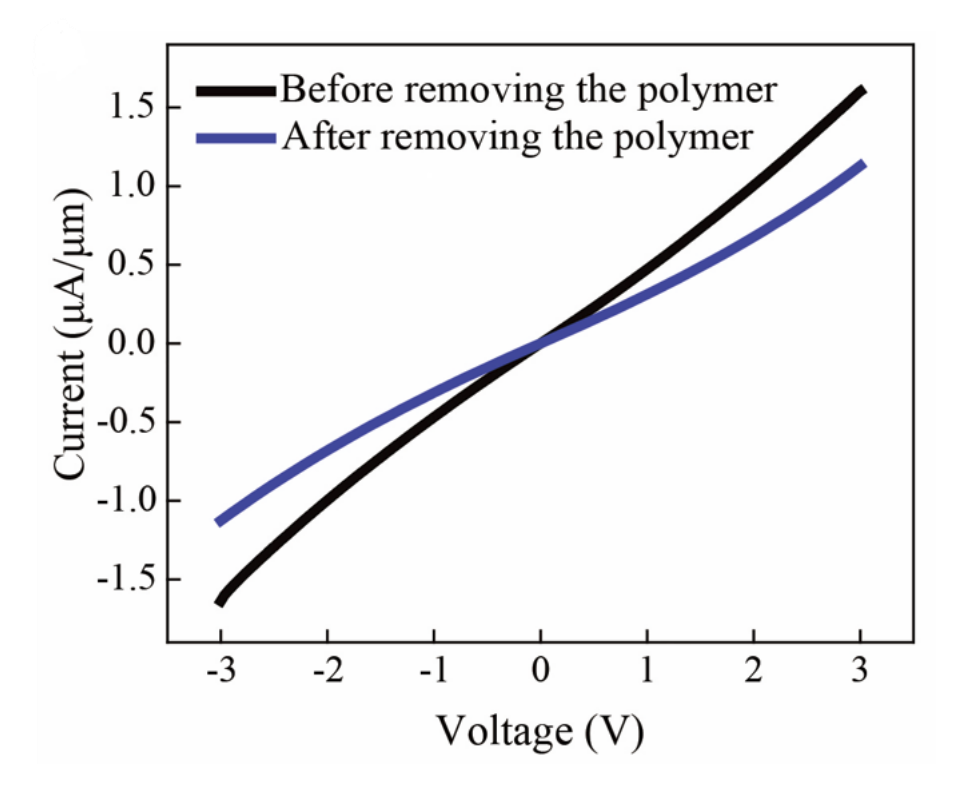


Figure 4.17 I_{ds}-V_{ds} curves before and after the removal of the EVA polymer.

Figure 4.18 presents a schematic representation of an as-fabricated BP FET utilizing a heavily doped silicon substrate as the back gate. This bottom-gate configuration offers

a multitude of advantages that extend beyond simplified manufacturing processes. One of the primary benefits of this design is the improved carrier mobility resulting from reduced surface scattering. The back-gate structure also provides enhanced electrostatic control over the channel, leading to better overall device performance. Additionally, the lower parasitic capacitances inherent in this configuration contribute to improved high-frequency performance, making these devices suitable for advanced electronic applications. The channel exposed in back-gate FETs offers significant practical advantages. It facilitates easier material characterization, allowing researchers to employ various spectroscopic and microscopic techniques without interference from a top gate structure. This exposed surface also enables direct optical access to the channel, making these FETs particularly well-suited for optoelectronic applications and photodetectors. Moreover, this configuration provides a versatile platform for further innovation. It facilitates the integration of additional components and the development of more complex structures above the BP thin film, including dual gates or heterojunctions.

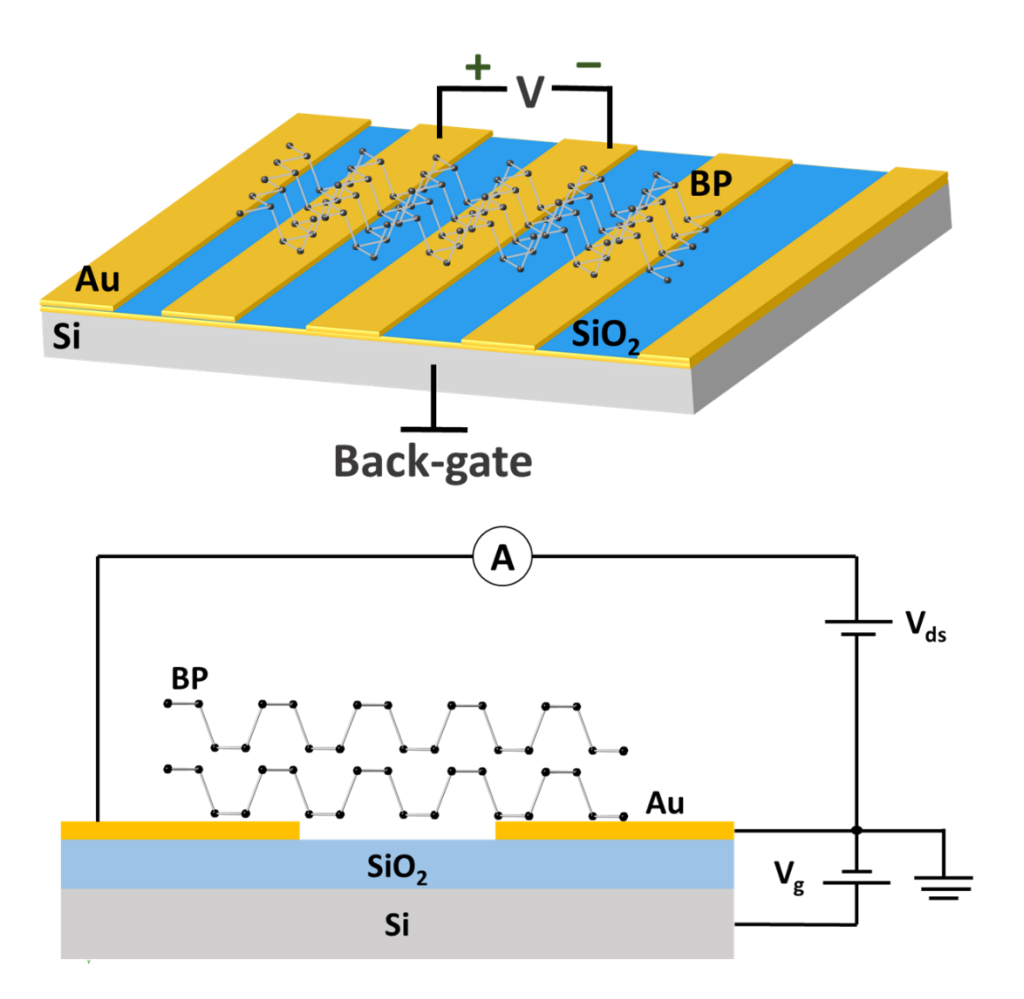


Figure 4.18 Schematic illustration of the wet-transferred back-gate BP FET.

The well-defined output characteristics of a BP FET with a thickness of approximately 5 nm and a channel length of 75 μ m, evaluated under ambient conditions, are shown in Figure 4.19. The inset displays the I_{ds} - V_{ds} output characteristics close to the origin, revealing a linear correlation between gate voltage (V_g) and output current. However, when a substantial negative gate bias is applied, a non-linear trend emerges, indicating a small Schottky barrier may arise between the BP thin films and the Au electrodes.

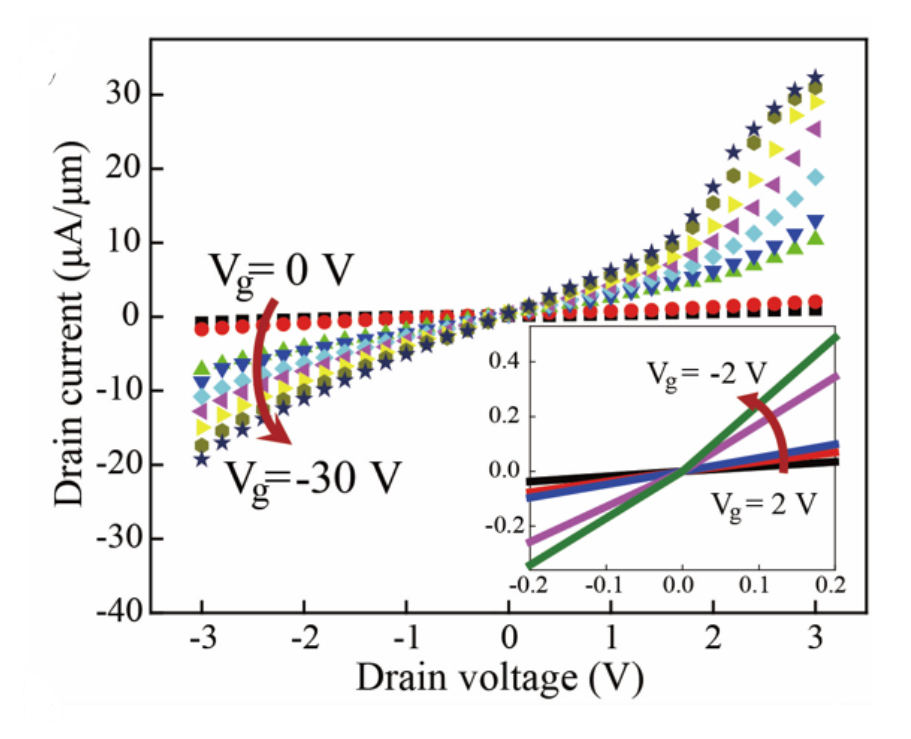


Figure 4.19 I_{ds} -V_{ds} for the BP FET at various V_g, including 0 V, -1 V, -2 V, -3 V, -4 V, -5 V, -10 V, -20 V, and -30 V. The inset provides a zoom-in view of the I_{ds} -V_{ds} curves for a 5-nm BP FET at gate voltages of -2 V, -1 V, 0 V, 1 V, and 2 V.

The transfer characteristics are plotted in Figure 4.20 on a linear scale, revealing that the field-effect mobility of the BP FET is calculated to be 293 cm²/V·s using the formula:

$$\mu_{FE} = \frac{L}{W \cdot C_g \cdot V_{ds}} \frac{dI}{dV_g} \tag{4.1}$$

where L stands for the channel length, W is the channel width, C_g indicates the capacitance density of the back-gate dielectric, and dI/dV_g represents the field-gating efficiency determined by aligning the slope of the curve in its linear operating range.

The inset of Figure 4.19 shows a logarithmic-scale relationship between gate voltage and source-drain current for the BP device on a silicon substrate covered with a 300



nm SiO₂ layer, measured under ambient conditions. With a V_{ds} of -0.1 V applied, we observed a modulation of I_{ds} by up to 3.6×10^3 times.

In a previous study, our group fabricated top-gate FETs using 5 nm-thick BP grown by PLD on mica substrates, employing ionic liquid as the gate dielectric. These devices achieved a carrier mobility of 213 cm²/V·s and an on/off ratio of 5×10³ at 295 K. In contrast, our current work with wet-transferred BP FETs demonstrates superior performance, exhibiting a remarkable carrier mobility of 293 cm²/V·s and an on/off ratio of up to 3.6×103. This enhancement indicates that the wet-transferred BP thin films not only maintain but potentially improve charge carrier transport efficiency while preserving consistent switching behavior. This can be attributed to several synergistic factors. Primarily, back-gate structures typically yield higher carrier mobility due to reduced surface scattering and enhanced electrostatic control over the channel. ¹⁸³The silicon substrate likely provides a superior interface quality with the BP film compared to mica, potentially minimizing interface scattering. ¹⁸⁴ Furthermore, the use of high-quality thermally grown SiO₂ as the gate dielectric in the back-gate configuration offers improved interface characteristics and lower trap densities compared to the ionic liquid used in the top-gate design. ¹⁸³ Additionally, the exposed BP channel in the back-gate structure may encounter fewer surface interactions that could hinder carrier transport, contributing to the overall performance enhancement.

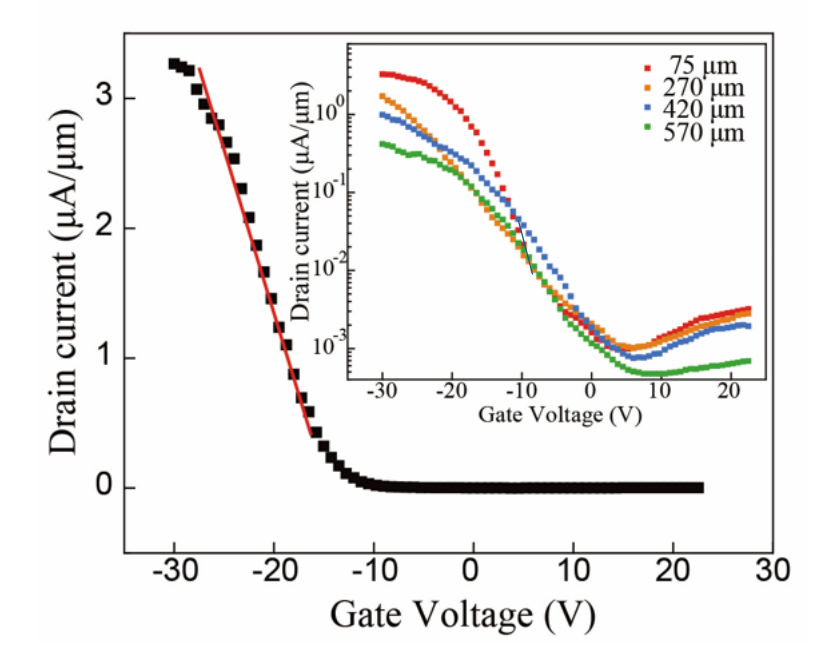


Figure 4.20 The transfer characteristics of a BP FET with a 75 μ m-channel length on a linear scale with a drain voltage of -0.1 V; the red dashed line indicates the linear fit of I_{ds}. The inset displays the transfer characteristics for BP FETs with channel lengths of 75 μ m, 270 μ m, 420 μ m, and 570 μ m on a logarithmic scale with a drain voltage of -0.1 V.

Figure 4.21 demonstrates the impact of channel length on field-effect mobility and the on/off ratio. As the channel length increases from 75 μ m to 570 μ m, both mobility and on/off ratio remain relatively stable, with only minor decreases observed. This reduction could be linked to a rise in defects and traps associated with longer channel lengths. These results further support the notion that wet-transferred BP thin films preserve high quality and integrity compared to the original as-grown BP.

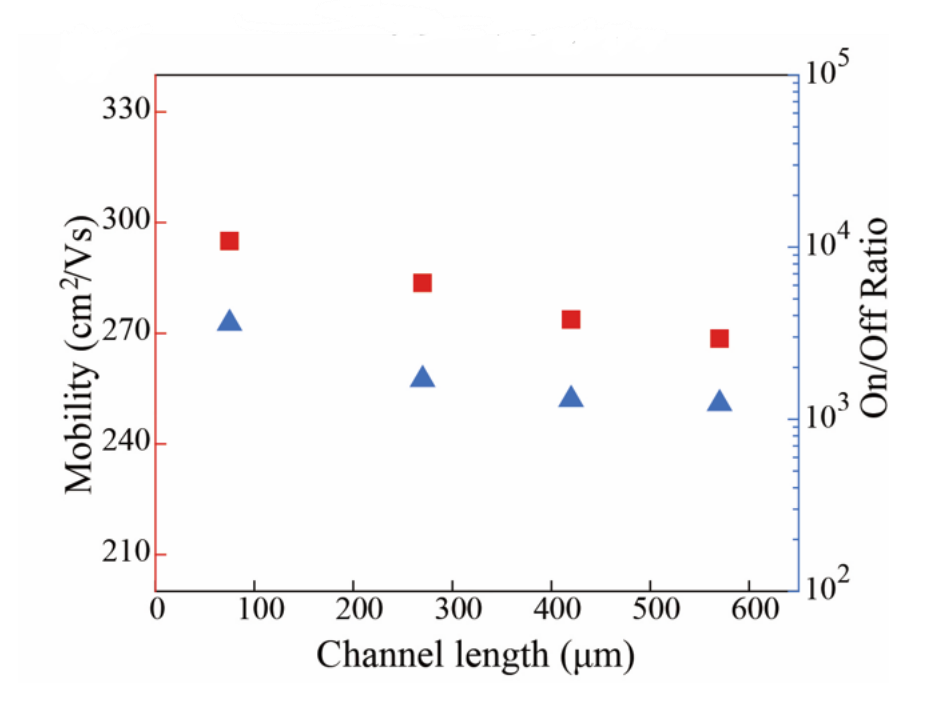


Figure 4.21 Dependence of mobility and on/off ratio on channel length.

The transfer process we developed ensures exceptional surface cleanliness and preservation of crystal structure, potentially contributing to the observed enhancements in carrier mobility. Table 4-2 provides a comprehensive comparison of FET performance derived from BP prepared through various methods and wettransferred MoS₂. Our large-scale BP preparation technique offers distinct advantages over direct mechanical or liquid exfoliation from high-quality BP bulk crystals, including uniform films with significantly larger lateral areas and reduced thickness while utilizing consistent device structures on silicon substrates.

Our devices demonstrate remarkable performance, achieving a field-effect mobility of 295 cm²V⁻¹s⁻¹ and an on/off ratio of 3.6×10³. Our devices demonstrate promising performance, achieving a field-effect mobility of 295 cm²V⁻¹s⁻¹ and an on/off ratio of 3.6×10³. These results show an improvement over our previous work on as-grown BP FETs on mica substrates, which exhibited a mobility of 213 cm²V⁻¹s⁻¹ and a similar

on/off ratio. This improvement underscores the effectiveness of our wet transfer technique in preserving and potentially enhancing the electrical properties of BP films.

In comparison to other BP-based devices, our FETs show competitive performance. While CVD-grown BP on SiO₂/Si substrates has demonstrated exceptionally high mobility (6500 cm²V⁻¹s⁻¹) and on/off ratio (around 10⁵). It is also important to note that these devices were significantly thicker (290 nm) than our 5 nm films. Mechanically exfoliated BP devices of similar thickness (~10 nm) showed comparable on/off ratios but lower mobility, while liquid-exfoliated BP devices exhibited substantially lower performance metrics.

Notably, our BP FETs outperform widely studied MoS₂-based devices in terms of mobility. Although MoS₂ devices generally demonstrate higher on/off ratios (10⁶-10⁹), their mobilities typically range from 4.5 to 35 cm²V⁻¹s⁻¹, significantly lower than our achieved 295 cm²V⁻¹s⁻¹. This highlights the potential of BP as a high-mobility 2D semiconductor for next-generation electronics.

Our findings indicate that the combination of PLD growth and wet transfer techniques can yield BP FETs with promising characteristics. This approach not only enables the production of devices with larger lateral dimensions but also achieves a balance between high mobility and a favorable on/off ratio. Furthermore, our FETs exhibit impressive sensitivity to minor changes in back-gate voltage, attributed to the unique properties of BP. This exceptional sensitivity makes BP highly suitable for applications demanding precise control and manipulation of electrical signals, thereby enhancing its functionality and performance in electronic devices and circuits.

Table 4-2 Comparison of thin-film FETs constructed using BP (same material) or wet transfer (similar preparation methods)

| | Preparation | Substrate | Thickness | Dimension | On/off | Field-effect | Ref. |
|---------|-------------|----------------------|-----------|-----------------|----------------------------------|----------------------|-------|
| | method | | (nm) | s | ratio | mobility | |
| | | | | (µm) | | $(cm^2V^{-1}s^{-1})$ | |
| BP | PLD + wet | SiO ₂ /Si | ~5 | 104 | 3.6×10^3 | 295 | This |
| | transfer | | | | | | work |
| | | | | | | | [185] |
| BP | PLD | Mica | 5 | 104 | ~5×10 ³ | 213 | [87] |
| BP | CVD | SiO ₂ /Si | 290 | 10 ³ | ~105 | 6500 | [168] |
| BP | Mechanical | SiO ₂ /Si | ~10 | 5 | ~104 | ~100 | [186] |
| | exfoliation | | | | | | |
| BP | Liquid | SiO ₂ /Si | 12 | 0.8 | ~10³ | 0.58 | [92] |
| | exfoliation | | | | | | |
| MoS_2 | CVD + wet | SiO ₂ /Si | 0.91 | ~20 | 10 ⁶ -10 ⁷ | 35 | [187] |
| | transfer | | | | | | |
| MoS_2 | CVD + wet | SiO ₂ /Si | 0.7 | ~40 | 108-109 | 7.6 | [188] |
| | transfer | | | | | | |
| MoS_2 | CVD + wet | SiO ₂ /Si | 10 | 10^{3} | 10 ⁵ | 4.5 | [189] |
| | transfer | | | | | | |

4.9 Conclusion

In conclusion, we present a wet transfer technique that effectively transfers high-crystalline, PLD-grown BP ultrathin films on a centimeter scale from mica to SiO₂/Si substrates, using EVA polymer as the transfer layer and EG as the wet medium. The

excellent adhesion characteristics of the EVA transfer layer, enhanced by the presence of polar groups in its polymer structure, are crucial for facilitating the efficient transfer of large BP films. Furthermore, obtaining conformal contact between the EVA adhesive layer and the BP film is essential because of the mechanical properties of the materials involved.

After successfully transferring large-area BP films, we fabricated few-layer BP FET arrays that displayed impressive homogeneity. Further investigations revealed that our FET devices exhibited exceptional electrical characteristics, including high carrier mobility and a substantial current switching ratio. Overall, the methodology proposed for preparing uniform large-area BP films on highly compatible silicon substrates shows significant potential for the future integration of scalable 2D thin films into electronic and optoelectronic devices. This work underscores the considerable promise of this approach to advance various fields.



Chapter 5 Conclusion and future prospectives

5.1 Conclusion

Since the innovative work reported by Novoselov et al. in 2004, which successfully exfoliated graphene from bulk graphite using scotch tape, two-dimensional (2D) materials have emerged as a prominent research focus due to their extensive potential applications in different areas. Initially, exfoliation served as the primary top-down method for producing monolayer and few-layer nanoflakes during the early exploration of 2D materials. This technique allowed for the efficient separation of high-quality multilayer 2D materials from single-crystalline bulk states, enabling thorough investigations into their fundamental properties. However, its limitations in achieving precise control over thickness and lateral dimensions hinder large-scale production, prompting the development of various processes aimed at creating highquality, uniform, 2D materials with large area. Among these materials, 2D black phosphorus (BP) has attracted considerable attention as a promising alternative to graphene due to its tunable bandgap, which lies between that of graphene and TMDs. Additionally, 2D BP demonstrates exceptional carrier mobility and a significant on/off ratio. For successful commercialization, it is crucial to establish robust techniques for producing large-area BP-based devices on various substrates under easily controlled conditions.

In this thesis, we first employed a piezoelectric actuator to conduct biaxial strain engineering, enabling the investigation of the anisotropic Raman response of ultrathin BP. Our results indicated that three characteristic peaks experienced a redshift under tensile strain and a blueshift under compressive strain. We also calculated the

Grüneisen parameters to study the relationship between strain—both tensile and compressive—and the phonon behavior of crystalline BP. The physical mechanisms behind the observed Raman response under strain were discussed, emphasizing their connection to changes in bond angles and lengths within BP. Additionally, we highlighted how modulation of biaxial strain could affect the anisotropic dispersion of BP, indicating its significant potential for innovative polarized light detection applications.

In the second part of the thesis, we developed a strategy to clean transfer centimeter-scale BP films grown via precisely controlled pulsed laser deposition (PLD) from mica to silicon substrates. We selected ethylene-vinyl acetate (EVA) polymer and ethylene glycol (EG) as the adhesive layer and medium to maintain the superior crystalline quality and properties of BP throughout the transfer process. Notably, we successfully fabricated large-scale bottom-gate few-layer BP field-effect transistor (FET) arrays on SiO₂/Si substrates, exhibiting exceptional homogeneity. Our FET arrays demonstrated outstanding electrical characteristics, including high carrier mobility and a significant current switching ratio comparable to the as-grown BP films on mica substrates. This study reveals that the wet transfer method can effectively produce scalable, high-crystallinity BP-based device arrays while preserving outstanding electrical performance, thereby enabling more complex design possibilities across a variety of applications.

5.2 Future Perspectives

The realization of large area 2D BP synthesis represents a critical frontier in the field of 2D materials. The exceptional properties of BP position it as a key player among 2D materials, offering unique opportunities for next-generation electronic and

optoelectronic devices. However, addressing the challenges associated with its scalable production and environmental stability are crucial for unlocking its full potential in future technological innovations.

Current fabrication methods for high-quality 2D BP primarily rely on bottom-up techniques, such as mechanical or liquid exfoliation from bulk crystals. While these methods have been instrumental in early research, they lack the scalability required for industrial applications. To achieve significant global technological impact, it is imperative to develop synthesis methods that facilitate the monolithic integration of transistors with interconnects and other components. This necessitates the production of BP thin films on a wafer scale, a challenge that remains at the forefront of research in this field.

A critical aspect of large-area BP synthesis is the interface between BP and the growth substrate. This interface profoundly influences the growth kinetics, ultimately determining the morphology and crystallinity of the films. Moreover, substrate interactions can modulate the electronic properties of BP through charge transfer and strain effects, offering both challenges and opportunities for material property modification. Understanding and controlling these substrate-BP interactions is vital for both fundamental research and application development. By revealing the impact of different substrates on the properties of BP, researchers can gain deeper insights into its intrinsic characteristics and behavior. This knowledge, in turn, enables the optimization of device performance for specific applications in electronics, optoelectronics, and sensing.

The development of large-area BP synthesis techniques is driven by several compelling factors. Wafer-scale production is essential for integration with existing

semiconductor manufacturing processes, ensuring industrial viability. Large-area growth facilitates the fabrication of multiple devices with consistent properties on a single substrate, crucial for device uniformity and reliability. Furthermore, continuous BP films could enable novel applications in flexible electronics, large-area sensors, and energy harvesting devices, expanding the potential impact across various technological domains.

As research in this field progresses, several key areas merit further investigation. Novel growth techniques that mitigate environmental sensitivity of BP while maintaining material quality are important. In-depth studies of substrate-BP interactions to elucidate growth mechanisms and optimize interface engineering will be crucial. The development of passivation strategies to enhance the stability of large-area BP films without compromising their unique properties remains a significant challenge. Additionally, the exploration of heterostructures and hybrid systems incorporating large-area BP holds promise for leveraging its exceptional characteristics in complex device architectures.

Another critical challenge facing the widespread adoption of 2D BP is its inherent instability in ambient environments. Although bulk BP is recognized as the most stable allotrope among phosphorus forms, transitioning to few-layer structures makes it highly reactive with oxygen and moisture in the air, which can disrupt its crystal structure. Most protective strategies developed thus far have focused on small-area applications of 2D BP, leaving a significant gap in addressing its stability for larger-scale uses. The susceptibility of BP to oxidation poses substantial challenges, leading to low reliability and repeatability during wafer-scale fabrication. To effectively harness the unique properties of BP in electronic components, these issues must be

resolved. Future research should prioritize the development of robust protective measures that can safeguard BP from environmental degradation while maintaining its desirable electrical characteristics. This may involve exploring novel encapsulation techniques, developing more effective passivation layers, or engineering BP-based heterostructures that inherently enhance stability. Additionally, in-situ characterization methods to monitor the degradation process and understand the mechanisms of environmental interactions will be invaluable in designing effective protection strategies.

In conclusion, while black phosphorus holds great promise as a versatile material for next-generation electronic devices, overcoming the barriers related to its scalable production and environmental stability is essential. The realization of large-area, high-quality BP synthesis methods, coupled with effective strategies to ensure long-term stability, will be pivotal in bridging the gap between the promising properties of BP and real-world applications. The journey towards harnessing the full potential of 2D BP is complex and multifaceted, requiring collaborative efforts across disciplines. Success in these endeavors will not only advance our fundamental understanding of 2D materials but also pave the way for transformative technologies that harness the unique attributes of BP. The potential impact of BP in flexible electronics, high-performance sensors, and novel optoelectronic devices underscores the importance of continued investment in this field. By overcoming the current limitations, BP could emerge as a cornerstone material in the next generation of electronic technologies, potentially revolutionizing areas such as telecommunications, energy harvesting, and biomedical sensing.



References

- 1. Kong, X. *et al.* Elemental two-dimensional nanosheets beyond graphene. *pubs.rsc.org*.
- Wang, Z. et al. Two-dimensional light-emitting materials: preparation, properties and applications. pubs.rsc.org.
- 3. Novoselov, K. S. *et al.* Electric field in atomically thin carbon films. *Science* (1979) **306**, 666–669 (2004).
- 4. Khan, K., Tareen, A., Aslam, M., ... R. W.-J. of M. & 2020, undefined. Recent developments in emerging two-dimensional materials and their applications. *pubs.rsc.org*.
- 5. Kumbhakar, P., Gowda, C. C., Materials, C. T.-F. in & 2021, undefined. Advance optical properties and emerging applications of 2D materials. *frontiersin.org*.
- Qiao, H. et al. Tunable Electronic and Optical Properties of 2D Monoelemental Materials Beyond Graphene for Promising Applications. Energy and Environmental Materials 4, 522–543 (2021).
- 7. Bian, Z., Miao, J., Zhao, Y. & Chai, Y. Strong Interlayer Interaction for Engineering Two-Dimensional Materials. *Acc Mater Res* **3**, 1220–1231 (2022).
- 8. Stark, M. S., Kuntz, K. L., Martens, S. J. & Warren, S. C. Intercalation of Layered Materials from Bulk to 2D. *Advanced Materials* **31**, (2019).

- 9. Zhang, X. *et al.* Van der Waals-Interface-Dominated All-2D Electronics. *Advanced Materials* **35**, (2023).
- Duong, D. L., Yun, S. J. & Lee, Y. H. Van der Waals Layered Materials:
 Opportunities and Challenges. ACS Nano 11, 11803–11830 (2017).
- Cheng, Z. et al. 2D Materials Enabled Next-Generation Integrated
 Optoelectronics: from Fabrication to Applications. Advanced Science 8,
 (2021).
- 12. Tan, T., Jiang, X., Wang, C., Yao, B. & Zhang, H. 2D Material Optoelectronics for Information Functional Device Applications: Status and Challenges. *Advanced Science* **7**, (2020).
- 13. Lv, J., Xie, J., Mohamed, A., ... X. Z.-C. S. & 2022, undefined.
 Photoelectrochemical energy storage materials: design principles and functional devices towards direct solar to electrochemical energy storage.
 pubs.rsc.org.
- 14. Fagiolari, L., Sampò, M., Lamberti, A., ... J. A.-E. S. & 2022, undefined.

 Integrated energy conversion and storage devices: Interfacing solar cells, batteries and supercapacitors. *Elsevier*.
- 15. Zhang, P., Wang, F., Yu, M., Zhuang, X. & Feng, X. Two-dimensional materials for miniaturized energy storage devices: from individual devices to smart integrated systems. *Chem Soc Rev* 47, 7426–7451 (2018).
- 16. Rogdakis, K., Karakostas, N. & Kymakis, E. Up-scalable emerging energy conversion technologies enabled by 2D materials: from miniature power



- harvesters towards grid-connected energy systems. *Energy Environ Sci* **14**, 3352–3392 (2021).
- 17. Alam, S., Asaduzzaman Chowdhury, M., Shahid, A., Alam, R. & Rahim, A.

 Synthesis of emerging two-dimensional (2D) materials Advances, challenges and prospects. *FlatChem* **30**, 100305 (2021).
- Zhang, X., Hou, L., Ciesielski, A. & Samorì, P. 2D Materials Beyond Graphene for High-Performance Energy Storage Applications. *Adv Energy Mater* 6, (2016).
- 19. Zhang, X., Hou, L., Materials, A. C.-... E. & 2016, undefined. 2D materials beyond graphene for high-performance energy storage applications. *Wiley Online Library*.
- 20. Tian, J., Zhao, Z., Kumar, A., Reviews, R. B.-C. S. & 2014, undefined. Recent progress in design, synthesis, and applications of one-dimensional TiO 2 nanostructured surface heterostructures: a review. *pubs.rsc.org*.
- 21. Jr, W. C. & Rethwisch, D. Fundamentals of Materials Science and Engineering:

 An Integrated Approach. (2020).
- 22. Guo, S., Reviews, S. D.-C. S. & 2011, undefined. Graphene nanosheet: synthesis, molecular engineering, thin film, hybrids, and energy and analytical applications. *pubs.rsc.org*.
- 23. Xia, F., Wang, H., Hwang, J., ... A. N.-N. R. & 2019, undefined. Black phosphorus and its isoelectronic materials. *nature.com*.

- 24. Li, L. *et al.* Black phosphorus field-effect transistors. *Nature Nanotechnology* 2014 9:5 **9**, 372–377 (2014).
- 25. Bhimanapati, G. R. *et al.* Recent Advances in Two-Dimensional Materials beyond Graphene. *ACS Nano* **9**, 11509–11539 (2015).
- 26. Zhang, F., Yu, J., Sun, J., Sun, Q. & Wang, Z. L. Bandgap Modulation in BP Field Effect Transistor and Its Applications. *Adv Electron Mater* **7**, (2021).
- Kusmartsev, F. V., Wu, W. M., Pierpoint, M. P. & Yung, K. C. Application of Graphene Within Optoelectronic Devices and Transistors. 191–221 (2015) doi:10.1007/978-981-287-242-5
- 28. Chang, H. & Wu, H. Graphene-based nanomaterials: Synthesis, properties, and optical and optoelectronic applications. *Adv Funct Mater* **23**, 1984–1997 (2013).
- 29. Choi, W. *et al.* Recent development of two-dimensional transition metal dichalcogenides and their applications. *Elsevier*.
- 30. Wang, H. *et al.* Physical and chemical tuning of two-dimensional transition metal dichalcogenides. *pubs.rsc.org*.
- 31. Chaves, A., Azadani, J., Applications, H. A.-... and & 2020, undefined. Bandgap engineering of two-dimensional semiconductor materials. *nature.com*.
- 32. Zheng, W. *et al.* Light emission properties of 2D transition metal dichalcogenides: fundamentals and applications. *Wiley Online Library*.

- 33. Meric, I. *et al.* Current saturation in zero-bandgap, top-gated graphene field-effect transistors. *Nature Nanotechnology 2008 3:11* **3**, 654–659 (2008).
- 34. Ramasubramaniam, A., Naveh, D. & Towe, E. Tunable band gaps in bilayer transition-metal dichalcogenides. *Phys Rev B Condens Matter Mater Phys* **84**, 205325 (2011).
- 35. Susarla, S. *et al.* Quaternary 2D Transition Metal Dichalcogenides (TMDs) with Tunable Bandgap. *Adv Mater* **29**, (2017).
- Qi, L. et al. Mid-Infrared Optoelectronic Waveguide Devices with 2D
 Materials. Wiley Online Library (2024) doi:10.1002/apxr.202400079.
- 37. Chen, C. et al. Widely tunable mid-infrared light emission in thin-film black phosphorus. Sci Adv 6, (2020).
- 38. Du, H., Lin, X., Xu, Z., C, D. C.-J. of M. C. & 2015, undefined. Recent developments in black phosphorus transistors. *pubs.rsc.org*.
- 39. Cui, X. *et al.* Extra-High Mechanical and Phononic Anisotropy in Black Phosphorus Blisters. *Wiley Online Library*.
- 40. Li, L. *et al.* Emerging in-plane anisotropic two-dimensional materials. *Wiley Online Library* **1**, 54–73 (2019).
- 41. Bhimanapati, G. R. *et al.* Recent Advances in Two-Dimensional Materials beyond Graphene. *ACS Nano* **9**, 11509–11539 (2015).

- 42. Geng, D., Yang, H. Y., Yang, H. Y. & Geng, D. C. Recent advances in growth of novel 2D materials: beyond graphene and transition metal dichalcogenides.

 Wiley Online Library 30, (2018).
- 43. Luo, M., Fan, T., Zhou, Y., Zhang, H. & Mei, L. 2D Black Phosphorus—Based Biomedical Applications. *Adv Funct Mater* **29**, (2019).
- 44. Ge, X., Xia, Z. & Guo, S. Recent Advances on Black Phosphorus for Biomedicine and Biosensing. *Adv Funct Mater* **29**, (2019).
- 45. Ren, X. *et al.* Properties, preparation and application of black phosphorus/phosphorene for energy storage: a review. *J Mater Sci* **52**, 10364–10386 (2017).
- 46. Wu, S., Hui, K. S. & Hui, K. N. 2D Black Phosphorus: from Preparation to Applications for Electrochemical Energy Storage. *Advanced Science* **5**, (2018).
- 47. Yi, Y., Sun, Z., Li, J., Chu, P. K. & Yu, X. F. Optical and Optoelectronic Properties of Black Phosphorus and Recent Photonic and Optoelectronic Applications.

 Small Methods 3, (2019).
- 48. Debnath, P. C., Park, K. & Song, Y. W. Recent Advances in Black-Phosphorus-Based Photonics and Optoelectronics Devices. *Small Methods* **2**, (2018).
- 49. Zeng, L. et al. Surface and interface control of black phosphorus. Chem 8,632–662 (2022).

- 50. Wu, Z., Jie, W., Yang, Z. & Hao, J. Hybrid heterostructures and devices based on two-dimensional layers and wide bandgap materials. *Mater Today Nano* **12**, 100092 (2020).
- 51. Yin, T. et al. Advancing Applications of Black Phosphorus and BP-Analog
 Materials in Photo/Electrocatalysis through Structure Engineering and Surface
 Modulation. Advanced Science 7, 2001431 (2020).
- 52. Butusov, M. & Jernelöv, A. *Phosphorus: An Element That Could Have Been Called Lucifer*. (2013).
- 53. Fung, C. M., Er, C. C., Tan, L. L., Mohamed, A. R. & Chai, S. P. Red Phosphorus:

 An Up-and-Coming Photocatalyst on the Horizon for Sustainable Energy

 Development and Environmental Remediation. *Chem Rev* **122**, 3879–3965

 (2022).
- 54. Cossairt, B., Piro, N., reviews, C. C.-C. & 2010, undefined. Early-transition-metal-mediated activation and transformation of white phosphorus. *ACS Publications* **110**, 4164–4177 (2010).
- 55. Xu, Y. *et al.* Recent progress in black phosphorus and black-phosphorusanalogue materials: properties, synthesis and applications. *pubs.rsc.org*.
- 56. Bachhuber, F. et al. The Extended Stability Range of Phosphorus Allotropes.

 Angewandte Chemie International Edition **53**, 11629–11633 (2014).
- 57. Gusmão, R., Sofer, Z. & Pumera, M. Black Phosphorus Rediscovered: From Bulk Material to Monolayers. *Angewandte Chemie International Edition* **56**, 8052–8072 (2017).

- 58. Pauling, L., Physics, M. S.-T. J. of C. & 1952, undefined. Bond orbitals and bond energy in elementary phosphorus. *pubs.aip.org*.
- 59. Greenwood, N. & Earnshaw, A. Chemistry of the Elements. (2012).
- 60. Zhang, G. *et al.* Layer-Dependent Electronic and Optical Properties of 2D Black Phosphorus: Fundamentals and Engineering. *Wiley Online Library*.
- 61. Zhang, G., Huang, S., Wang, F. & Yan, H. Layer-Dependent Electronic and Optical Properties of 2D Black Phosphorus: Fundamentals and Engineering. *Laser Photon Rev* **15**, (2021).
- 62. Xing, C. *et al.* Preparations, properties and applications of low-dimensional black phosphorus. *Elsevier*.
- 63. Zhang, F., Yu, J., Sun, J., Sun, Q. & Wang, Z. L. Bandgap Modulation in BP Field Effect Transistor and Its Applications. *Adv Electron Mater* **7**, (2021).
- 64. Takao, Y., Asahina, H. & Morita, A. Electronic Structure of Black Phosphorus in Tight Binding Approach. *JPSJ* **50**, 3362 (1981).
- 65. Low, T. et al. Tunable optical properties of multilayer black phosphorus thin films. Phys Rev B Condens Matter Mater Phys **90**, 075434 (2014).
- 66. Castellanos-Gomez, A. *et al.* Isolation and characterization of few-layer black phosphorus. *2d Mater* **1**, 25001 (2014).
- 67. Liang, L. *et al.* Electronic bandgap and edge reconstruction in phosphorene materials. *Nano Lett* **14**, 6400–6406 (2014).

- 68. Liu, H. *et al.* Phosphorene: An unexplored 2D semiconductor with a high hole mobility. *ACS Nano* **8**, 4033–4041 (2014).
- 69. Li, Y., Yang, S. & Li, J. Modulation of the electronic properties of ultrathin black phosphorus by strain and electrical field. *Journal of Physical Chemistry C* **118**, 23970–23976 (2014).
- 70. Zhang, M., Biesold, G., reviews, Z. L.-C. society & 2021, undefined. A multifunctional 2D black phosphorene-based platform for improved photovoltaics. *pubs.rsc.org*.
- 71. Liu, S. *et al.* Thickness-dependent Raman spectra, transport properties and infrared photoresponse of few-layer black phosphorus. *J Mater Chem C Mater* 3, 10974–10980 (2015).
- 72. Xia, F., Wang, H. & Jia, Y. Rediscovering black phosphorus as an anisotropic layered material for optoelectronics and electronics. *Nat Commun* **5**, (2014).
- 73. Qiao, J., Kong, X., Hu, Z. X., Yang, F. & Ji, W. High-mobility transport anisotropy and linear dichroism in few-layer black phosphorus. *Nat Commun* **5**, (2014).
- 74. Ge, X., Xia, Z. & Guo, S. Recent Advances on Black Phosphorus for Biomedicine and Biosensing. *Adv Funct Mater* **29**, (2019).
- 75. Koenig, S. P., Doganov, R. A., Schmidt, H., Castro Neto, A. H. & Özyilmaz, B. Electric field effect in ultrathin black phosphorus. *Appl Phys Lett* **104**, (2014).
- 76. Kim, J. *et al.* 2D MATERIALS. Observation of tunable band gap and anisotropic Dirac semimetal state in black phosphorus. *Science* **349**, 723–726 (2015).

- 77. Xia, F., Wang, H. & Jia, Y. Rediscovering black phosphorus as an anisotropic layered material for optoelectronics and electronics. *Nature Communications* 2014 5:1 5, 1–6 (2014).
- 78. Gaddemane, G. *et al.* Theoretical studies of electronic transport in monolayer and bilayer phosphorene: A critical overview. *Phys Rev B* **98**, (2018).
- 79. Kumar, A. & Rai, R. S. Electrical, Mechanical, and Thermal Properties of Two-Dimensional Nanomaterials. *Two-Dimensional Nanomaterials-Based Polymer Nanocomposites: Processing, Properties and Applications* 195–230 (2024) doi:10.1002/9781119905110.CH6.
- 80. Tian, Z., Guo, C., Zhao, M., Li, R. & Xue, J. Two-Dimensional SnS: A

 Phosphorene Analogue with Strong In-Plane Electronic Anisotropy. *ACS Nano*11, 2219–2226 (2017).
- 81. Li, L. *et al.* Emerging in-plane anisotropic two-dimensional materials. *Wiley Online Library* **1**, 54–73 (2019).
- Li, X. et al. Review of Anisotropic 2D Materials: Controlled Growth, Optical Anisotropy Modulation, and Photonic Applications. Laser Photon Rev 15, (2021).
- 83. Wang, J. *et al.* Mid-infrared polarized emission from black phosphorus lightemitting diodes. *Nano Lett* **20**, 3651–3655 (2020).
- 84. Zhu, M. *et al.* Metal-Free Photocatalyst for H2 Evolution in Visible to Near-Infrared Region: Black Phosphorus/Graphitic Carbon Nitride. *J Am Chem Soc* **139**, 13234–13242 (2017).

- 85. Lin, C., Grassi, R., Low, T. & Helmy, A. S. Multilayer Black Phosphorus as a Versatile Mid-Infrared Electro-optic Material. *Nano Lett* **16**, 1683–1689 (2016).
- 86. Bai, L. *et al.* Solution-processed black phosphorus/PCBM hybrid heterojunctions for solar cells. *J Mater Chem A Mater* **5**, 8280–8286 (2017).
- 87. Wu, Z. *et al.* Large-scale growth of few-layer two-dimensional black phosphorus. *Nat Mater* **20**, 1203–1209 (2021).
- 88. Miao, J. *et al.* Air-Stable Humidity Sensor Using Few-Layer Black Phosphorus.

 ACS Appl Mater Interfaces 9, 10019–10026 (2017).
- 89. Guo, Q. *et al.* Black phosphorus mid-infrared photodetectors with high gain.

 Nano Lett **16**, 4648–4655 (2016).
- Ahmed, T. et al. Fully Light-Controlled Memory and Neuromorphic
 Computation in Layered Black Phosphorus. Adv Mater 33, (2021).
- 91. Zhang, M., Biesold, G. M. & Lin, Z. A multifunctional 2D black phosphorene-based platform for improved photovoltaics. *Chem Soc Rev* **50**, 13346–13371 (2021).
- 92. Yasaei, P. et al. High-quality black phosphorus atomic layers by liquid-phase exfoliation. Advanced Materials **27**, 1887–1892 (2015).
- 93. Kang, J. *et al.* Solvent exfoliation of electronic-grade, two-dimensional black phosphorus. *ACS Nano* **9**, 3596–3604 (2015).

- 94. Fan, S. et al. Rapid thermal thinning of black phosphorus. J Mater Chem C

 Mater 5, 10638–10644 (2017).
- 95. Jia, J. et al. Plasma-treated thickness-controlled two-dimensional black phosphorus and its electronic transport properties. ACS Nano 9, 8729–8736 (2015).
- 96. Lee, G., Lee, J.-Y., Lee, G.-H. & Kim, J. Tuning the thickness of black phosphorus via ion bombardment-free plasma etching for device performance improvement. *J Mater Chem C Mater* **4**, 6234–6239 (2016).
- 97. Kim, S., Jung, Y., Lee, J.-Y., Lee, G.-H. & Kim, J. In situ thickness control of black phosphorus field-effect transistors via ozone treatment. *Nano Res* **9**, 3056–3065 (2016).
- 98. Li, X. et al. Synthesis of thin-film black phosphorus on a flexible substrate. 2d Mater 2, 31002 (2015).
- 99. Xu, Y. et al. Epitaxial nucleation and lateral growth of high-crystalline black phosphorus films on silicon. *Nat Commun* **11**, 1–8 (2020).
- Zhou, J. et al. Layered Intercalation Materials. Advanced Materials 33, 2004557 (2021).
- 101. Zhao, Y., Wu, Z., Dang, Z., Reviews, J. H.-A. P. & 2022, undefined. Progress in the synthesis of 2D black phosphorus beyond exfoliation. *pubs.aip.org*.

- 102. Schranghamer, T., Sharma, M., ... R. S.-C. S. & 2021, undefined. Review and comparison of layer transfer methods for two-dimensional materials for emerging applications. *pubs.rsc.org*.
- 103. Fan, S. *et al.* Transfer assembly for two-dimensional van der Waals heterostructures. *iopscience.iop.org*.
- 104. Chen, Y., Gong, X. L. & Gai, J. G. Progress and Challenges in Transfer of Large-Area Graphene Films. *Advanced Science* **3**, (2016).
- 105. A facile and efficient dry transfer technique for two-dimensional Van derWaals heterostructure.
 https://cpb.iphy.ac.cn/article/2017/1899/cpb 26 8 087306.html.
- 106. Kim, C., Yoon, M., Jang, B., Lubricants, J. K.-T. and & 2020, undefined. A review on transfer process of two-dimensional materials. *koreascience.krC Kim, MA Yoon, B Jang, JH Kim, KS KimTribology and Lubricants, 2020 koreascience.kr* **36**, 1−10 (2020).
- 107. Somphonsane, R., ... K. B.-... S. (2076-3417 & 2024, undefined. Advances in 2D Material Transfer Systems for van der Waals Heterostructure Assembly. **search.ebscohost.com.**
- 108. Bi, S., Wang, H., Wang, R., Cheliotis , I. & Zergioti, I. A review on transfer methods of two-dimensional materials. *iopscience.iop.org* **11**, 22004 (2024).
- 109. Nakatani, M. *et al.* Ready-to-transfer two-dimensional materials using tunable adhesive force tapes. *Nature Electronics 2024 7:2* **7**, 119–130 (2024).

- 110. Zhao, Y. et al. Large-area transfer of two-dimensional materials free of cracks, contamination and wrinkles via controllable conformal contact. Nature Communications 2022 13:1 13, 1–10 (2022).
- 111. Onodera, M., Materials, T. M.-S. and & 2023, undefined. Transfer of van der Waals Heterostructures of Two-dimensional Materials onto Microelectromechanical Systems. sensors.myu-group.co.jp 35, 1929–1939 (2023).
- 112. Onodera, M. *et al.* All-dry flip-over stacking of van der Waals junctions of 2D materials using polyvinyl chloride. *Scientific Reports 2022 12:1* **12**, 1–7 (2022).
- 113. Nakatani, M. *et al.* Ready-to-transfer two-dimensional materials using tunable adhesive force tapes. *Nature Electronics 2024 7:2* **7**, 119–130 (2024).
- 114. Watson, A., Lu, W., Guimarães, M., Materials, M. S.-2D & 2021, undefined.
 Transfer of large-scale two-dimensional semiconductors: challenges and developments. *iopscience.iop.org* (2021) doi:10.1088/2053-1583/abf234.
- 115. Liu, Y. *et al.* Recent progress in the fabrication, properties, and devices of heterostructures based on 2D materials. *Springer*.
- Liang, X. et al. Toward clean and crackless transfer of graphene. ACS Nano 5,
 9144–9153 (2011).
- 117. Dong, W., Dai, Z., Liu, L., Materials, Z. Z.-A. & 2024, undefined. Toward clean 2d materials and devices: Recent progress in transfer and cleaning methods.

 Wiley Online Library 36, (2023).

- 118. Gao, Y., Chen, J., Chen, G., Fan, C. & Liu, X. Recent Progress in the Transfer of Graphene Films and Nanostructures. *Small Methods* **5**, (2021).
- Dong, W., Dai, Z., Liu, L., Materials, Z. Z.-A. & 2024, undefined. Toward clean2d materials and devices: Recent progress in transfer and cleaning methods.Wiley Online Library 36, (2023).
- 120. Jia, L. *et al.* Fabrication technologies for the on-chip integration of 2D materials. *Wiley Online Library* **6**, (2022).
- 121. Pham, P. V. et al. Transfer of 2D Films: From Imperfection to Perfection. ACS

 Nano 18, 14841–14876 (2024).
- 122. Schranghamer, T., Sharma, M., ... R. S.-C. S. & 2021, undefined. Review and comparison of layer transfer methods for two-dimensional materials for emerging applications. *pubs.rsc.org*.
- 123. Watson, A., Lu, W., Guimarães, M., Materials, M. S.-2D & 2021, undefined.

 Transfer of large-scale two-dimensional semiconductors: challenges and developments. *iopscience.iop.org* (2021) doi:10.1088/2053-1583/abf234.
- 124. Cai, Z., Liu, L., Materials, P. Z.-I. & F. & 2024, undefined. The development of transfer technologies for advanced 2D circuits integration. *Wiley Online Library* 1, 304–322 (2024).
- 125. Chen, Y., Gong, X. L. & Gai, J. G. Progress and Challenges in Transfer of Large-Area Graphene Films. *Advanced Science* **3**, (2016).



- 126. Zhao, Y. *et al.* Large-area transfer of two-dimensional materials free of cracks, contamination and wrinkles via controllable conformal contact. *Nature Communications 2022 13:1* **13**, 1–10 (2022).
- 127. Fan, S. *et al.* Strategy for transferring van der Waals materials and heterostructures. *iopscience.iop.org*.
- 128. Liu, Y., Zhang, S., He, J., Wang, Z. M. & Liu, Z. Review and comparison of layer transfer methods for two-dimensional materials for emerging applications. *pubs.rsc.org* **11**, 3 (2019).
- 129. Pham, P. V *et al.* Transfer of 2D Films: From Imperfection to Perfection. *ACS Publications* **18**, 14841–14876 (2024).
- 130. Pham, P. V. et al. 2D Heterostructures for Ubiquitous Electronics and Optoelectronics: Principles, Opportunities, and Challenges. Chem Rev 122, 6514–6613 (2022).
- 131. Novoselov, K. S. Nobel Lecture: Graphene: Materials in the Flatland. *Rev Mod Phys* 83, 837–849 (2011).
- 132. Song, C. & Kwon, H. J. Ferroelectrics based on hfo2 film. *Electronics*(Switzerland) **10**, (2021).
- 133. Manjunatha, J. G. & Hussain, C. M. Carbon Nanomaterials-Based Sensors: Emerging Research Trends in Devices and Applications. *Carbon Nanomaterials-Based Sensors: Emerging Research Trends in Devices and Applications* 1–450 (2022) doi:10.1016/C2020-0-04501-9.

- 134. Deng, X. *et al.* Application of atomic force microscopy in cancer research. *J Nanobiotechnology* **16**, V (2018).
- 135. Vision and visual servoing for nanomanipulation and nanocharacterization in scanning electron microscope.
 - https://www.researchgate.net/publication/281534044_Vision_and_visual_se rvoing_for_nanomanipulation_and_nanocharacterization_in_scanning_electr on_microscope.
- 136. Anodised TiO2 Nanotubes: Synthesis, Growth Mechanism and Thermal Stability.
 - https://www.researchgate.net/publication/215769214_Anodised_TiO2_Nano tubes_Synthesis_Growth_Mechanism_and_Thermal_Stability.
- 137. Dash, T. & Maiti, C. K. An overview of nanoscale device fabrication technology—part I. *Nanoelectronics: Physics, Materials and Devices* 193–214 (2023) doi:10.1016/B978-0-323-91832-9.00007-5.
- 138. Dai, Z., Liu, L. & Zhang, Z. Strain Engineering of 2D Materials: Issues and Opportunities at the Interface. *Advanced Materials* **31**, 1805417 (2019).
- 139. Du, J. et al. Strain Engineering in 2D Material-Based Flexible Optoelectronics.

 Small Methods 5, 2000919 (2021).
- 140. An, J. *et al.* Perspectives of 2D Materials for Optoelectronic Integration. *Adv Funct Mater* **32**, 2110119 (2022).
- 141. Yang, S., Chen, Y. & Jiang, C. Strain engineering of two-dimensional materials: Methods, properties, and applications. *InfoMat* **3**, 397–420 (2021).

- 142. Qi, Y. et al. Recent Progress in Strain Engineering on Van der Waals 2D Materials: Tunable Electrical, Electrochemical, Magnetic, and Optical Properties. Advanced Materials 35, 2205714 (2023).
- 143. Peng, Z., Chen, X., Fan, Y., ... D. S.-L. S. & & 2020, undefined. Strain engineering of 2D semiconductors and graphene: from strain fields to band-structure tuning and photonic applications. nature.comZ Peng, X Chen, Y Fan, DJ Srolovitz, D LeiLight: Science & Applications, 2020•nature.com 2047–7538 doi:10.1038/s41377-020-00421-5.
- 144. Peng, Z., Chen, X., Fan, Y., Srolovitz, D. J. & Lei, D. Strain engineering of 2D semiconductors and graphene: from strain fields to band-structure tuning and photonic applications. *Light: Science & Applications 2020 9:1* **9**, 1–25 (2020).
- 145. Duong, D. L., Yun, S. J. & Lee, Y. H. Van der Waals Layered Materials:
 Opportunities and Challenges. ACS Nano 11, 11803–11830 (2017).
- 146. Gao, L. Flexible Device Applications of 2D Semiconductors. *Small* 13, 1603994 (2017).
- 147. Kim, S. J., Choi, K., Lee, B., Kim, Y. & Hong, B. H. Materials for Flexible, Stretchable Electronics: Graphene and 2D Materials. *Annu Rev Mater Res* 45, 63–84 (2015).
- 148. Li, F. *et al.* Recent advances in strain-induced piezoelectric and piezoresistive effect-engineered 2D semiconductors for adaptive electronics and optoelectronics. *Springer* **12**, 3 (2020).

- 149. Blundo, E., Cappelluti, E., Felici, M., Pettinari, G. & Polimeni, A. Strain-tuning of the electronic, optical, and vibrational properties of two-dimensional crystals. *Appl Phys Rev* **8**, (2021).
- 150. Self-powered cardiac pacemaker enabled by flexible single crystalline PMN-PT piezoelectric energy harvester. europepmc.orgGT Hwang, H Park, JH Lee, SK Oh, KI Park, M Byun, G Ahn, CK Jeong, K No, H KwonAdvanced Materials (Deerfield Beach, Fla.), 2014 europepmc.org.
- 151. Effect of grain size on piezoelectric, ferroelectric and dielectric properties of PMN-PT ceramics. ElsevierR Pramanik, MK Sahukar, Y Mohan, B

 Praveenkumar, SR Sangawar, A ArockiarajanCeramics International,

 2019 Elsevier.
- 152. Xu, S. *et al.* Flexible piezoelectric PMN–PT nanowire-based nanocomposite and device. *ACS PublicationsS Xu, Y Yeh, G Poirier, MC McAlpine, RA Register, N YaoNano letters, 2013•ACS Publications* **13**, 2393–2398 (2013).
- 153. Guo, F. *et al.* Piezoelectric biaxial strain effects on the optical and photoluminescence spectra of 2D III–VI compound α -In2Se3 nanosheets. *pubs.aip.org* **116**, 113101 (2020).
- 154. Publications, N. et al. Phosphorene: an unexplored 2D semiconductor with a high hole mobility. ACS PublicationsH Liu, AT Neal, Z Zhu, Z Luo, X Xu, D

 Tománek, PD YeACS nano, 2014•ACS Publications 8, 4033–4041 (2014).
- 155. Ling, X. *et al.* Anisotropic Electron-Photon and Electron-Phonon Interactions in Black Phosphorus. *Nano Lett* **16**, 2260–2267 (2016).

- 156. Wang, X. et al. Highly anisotropic and robust excitons in monolayer black phosphorus. nature.comX Wang, AM Jones, KL Seyler, V Tran, Y Jia, H Zhao, H Wang, L Yang, X Xu, F XiaNature nanotechnology, 2015•nature.com.
- 157. Li, Y. et al. Giant anisotropic Raman response of encapsulated ultrathin black phosphorus by uniaxial strain. Wiley Online LibraryY Li, Z Hu, S Lin, SK Lai, W Ji, SP LauAdvanced Functional Materials, 2017•Wiley Online Library 27, (2017).
- 158. Wang, Y. et al. Strain-induced direct—indirect bandgap transition and phonon modulation in monolayer WS2. SpringerY Wang, C Cong, W Yang, J Shang, N Peimyoo, Y Chen, J Kang, J Wang, W Huang, T YuNano Research, 2015•Springer 8, 2562–2572 (2015).
- 159. Conley, H. J. *et al.* Bandgap engineering of strained monolayer and bilayer MoS2. *Nano Lett* **13**, 3626–3630 (2013).
- 160. Hanfland, M., Beister, H. & Syassen, K. Graphite under pressure: Equation of state and first-order Raman modes. *Phys Rev B* **39**, 12598–12603 (1989).
- 161. Mohiuddin, T. M. G. *et al.* Uniaxial strain in graphene by Raman spectroscopy:

 G peak splitting, Grüneisen parameters, and sample orientation. *Phys Rev B*Condens Matter Mater Phys **79**, (2009).
- 162. Hu, Z. *et al.* Interlayer electronic hybridization leads to exceptional thickness-dependent vibrational properties in few-layer black phosphorus.

 pubs.rsc.orgZX Hu, X Kong, J Qiao, B Normand, W JiNanoscale,

 2016•pubs.rsc.org.

- 163. Kumar, A. *et al.* Memory effect and coexistence of negative and positive photoconductivity in black phosphorus field effect transistor for neuromorphic vision sensors. *pubs.rsc.orgA Kumar, K Intonti, L Viscardi, O Durante, A Pelella, O Kharsah, S Sleziona, F GiubileoMaterials Horizons, 2024•pubs.rsc.org* 11, 2397 (2024).
- 164. Hu, Z. et al. Two-dimensional black phosphorus: its fabrication, functionalization and applications. pubs.rsc.orgZ Hu, T Niu, R Guo, J Zhang, M Lai, J He, L Wang, W ChenNanoscale, 2018 pubs.rsc.org.
- 165. Liu, S. et al. Thickness-dependent Raman spectra, transport properties and infrared photoresponse of few-layer black phosphorus. pubs.rsc.orgS Liu, N Huo, S Gan, Y Li, Z Wei, B Huang, J Liu, J Li, H ChenJournal of Materials Chemistry C, 2015•pubs.rsc.org.
- 166. Deng, B. *et al.* Efficient electrical control of thin-film black phosphorus bandgap. *nature.comB Deng, V Tran, Y Xie, H Jiang, C Li, Q Guo, X Wang, H Tian, SJ Koester, H Wang, JJ ChaNature communications, 2017 nature.com* (2017) doi:10.1038/ncomms14474.
- 167. Liu, X. et al. Resolving the in-plane anisotropic properties of black phosphorus. Wiley Online LibraryX Liu, CR Ryder, SA Wells, MC HersamSmall Methods, 2017•Wiley Online Library 1, (2017).
- 168. Chen, C. et al. Growth of single-crystal black phosphorus and its alloy films through sustained feedstock release. nature.comC Chen, Y Yin, R Zhang, Q



Yuan, Y Xu, Y Zhang, J Chen, Y Zhang, C Li, J Wang, J Li, L FeiNature Materials, 2023•nature.com.

- 169. Gurarslan, A. et al. Surface-Energy-Assisted Perfect Transfer of Centimeter-Scale Monolayer and Few-Layer MoS2 Films onto Arbitrary Substrates. ACS

 Publications A Gurarslan, Y Yu, L Su, Y Yu, F Suarez, S Yao, Y Zhu, M Ozturk, Y

 Zhang, L CaoACS nano, 2014 ACS Publications 8, 11522–11528 (2014).
- 170. Pirkle, A. *et al.* The effect of chemical residues on the physical and electrical properties of chemical vapor deposited graphene transferred to SiO2. *pubs.aip.org* (2011) doi:10.1063/1.3643444.
- 171. Kim, C., Yoon, M.-A., Jang, B., Kim, J.-H. & Kim, K.-S. A review on transfer process of two-dimensional materials. *oak.go.krCR Kim, MAR Yoon, BSR JangTribology and Lubricants, 2020•oak.go.kr* **36**, 1–10 (2020).
- 172. Zhou, Q., Chen, Q., Tong, Y. & Wang, J. Light-Induced Ambient Degradation of Few-Layer Black Phosphorus: Mechanism and Protection. *Angewandte*Chemie International Edition 55, 11437–11441 (2016).
- 173. Li, Q. et al. Recent advances in oxidation and degradation mechanisms of ultrathin 2D materials under ambient conditions and their passivation strategies. pubs.rsc.orgQ Li, Q Zhou, L Shi, Q Chen, J WangJournal of Materials Chemistry A, 2019•pubs.rsc.org.
- 174. Ren, X., Yang, X., Xie, G. & Luo, J. Black Phosphorus Quantum Dots in Aqueous Ethylene Glycol for Macroscale Superlubricity. *ACS Appl Nano Mater* **3**, 4799–4809 (2020).

- 175. Li, H., Li, C., Zhao, H., Tao, B. & Wang, G. Two-Dimensional Black Phosphorus:

 Preparation, Passivation and Lithium-Ion Battery Applications. *Molecules*2022, Vol. 27, Page 5845 27, 5845 (2022).
- 176. Gao, X. et al. Integrated wafer-scale ultra-flat graphene by gradient surface energy modulation. nature.comX Gao, L Zheng, F Luo, J Qian, J Wang, M Yan, W Wang, Q Wu, J Tang, Y Cao, C TanNature Communications, 2022•nature.com doi:10.1038/s41467-022-33135-w.
- 177. Patil, C. *et al.* Highly accurate, reliable, and non-contaminating two-dimensional material transfer system. *Appl Phys Rev* **9**, 11419 (2022).
- 178. Suo, J. *et al.* Interfacial engineering from material to solvent: a mechanistic understanding on stabilizing α-formamidinium lead triiodide perovskite photovoltaics. *ElsevierJ Suo, B Yang, J Jeong, T Zhang, S Olthof, F Gao, M Grätzel, G Boschloo, A HagfeldtNano Energy, 2022 Elsevier.*
- 179. Zhang, J. *et al.* Ethylene glycol nanofluids dispersed with monolayer graphene oxide nanosheet for high-performance subzero cold thermal energy storage.

 **RSC Adv 11*, 30495–30502 (2021).
- 180. Li, X. et al. Large-area synthesis of high-quality and uniform graphene films on copper foils. science.orgX Li, W Cai, J An, S Kim, J Nah, D Yang, R Piner, A Velamakanni, I Jung, E Tutucscience, 2009•science.org 324, 1312–1314 (2009).
- 181. Lee, C. H. *et al.* Transferred large area single crystal MoS2 field effect transistors. *Appl Phys Lett* **107**, 193503 (2015).

- 182. Yu, Y., Fong, P. W. K., Wang, S. & Surya, C. Fabrication of WS2/GaN p-n

 Junction by Wafer-Scale WS2 Thin Film Transfer. *Sci Rep* **6**, 1–11 (2016).
- 183. Lemme, M., Echtermeyer, T., ... M. B.-S.-S. & 2008, undefined. Mobility in graphene double gate field effect transistors. *Elsevier*.
- 184. Ohata, A. *et al.* Impact of back-gate biasing on effective field and mobility in ultrathin silicon-on-insulator metal-oxide-semiconductor field-effect-transistors. *J Appl Phys* **113**, (2013).
- 185. Zhao, Y. *et al.* A clean transfer approach to prepare centimetre-scale black phosphorus crystalline multilayers on silicon substrates for field-effect transistors. *Nature Communications 2024 15:1* **15**, 1–8 (2024).
- 186. Na, J. *et al.* Few-layer black phosphorus field-effect transistors with reduced current fluctuation. *ACS Nano* **8**, 11753–11762 (2014).
- 187. Shen, Y. *et al.* Rational design on wrinkle-less transfer of transition metal dichalcogenide monolayer by adjustable wettability-assisted transfer method. *Adv Funct Mater* **31**, 2104978 (2021).
- 188. Mondal, A. et al. Low Ohmic contact resistance and high on/off ratio in transition metal dichalcogenides field-effect transistors via residue-free transfer. Nat Nanotechnol 1–10 (2023).
- 189. Lee, C. H. *et al.* Transferred large area single crystal MoS2 field effect transistors. *Appl Phys Lett* **107**, (2015).